Table of Contents

Tabla de Contenido

Copper Recovery Through Smelter Slag Flotation in Atacama, Chile: An Industrial Case Study

Recuperación de cobre mediante flotación de escorias de fundición en Atacama, Chile: un estudio de caso industrial

Osvaldo Pavez [1], Pablo Herrera [2], Miguel González [3], and Oscar Rivera [4]

ABSTRACT

Copper slag flotation was studied on an industrial scale at a concentrator plant in the region of Atacama, Chile. This study consisted of the physical, chemical, and mineralogical characterization of the copper slag, along with preliminary flotation tests. This article focuses on industrial flotation, which consisted of two one-year campaigns (2016 and 2017). The first campaign was carried out using an existing copper slag flotation circuit in the plant. During the second campaign (2017), a circuit for sulfide ore flotation with an additional columnar flotation cleaning stage was evaluated. Results showed an improvement in metallurgical parameters on the second campaign (including improvements in processing capacity, concentrate copper grade, and metallurgical recovery). From the industrial copper slag flotation campaigns, it was concluded that it is possible to obtain a commercial-quality copper concentrate, suitable for further processing in a copper smelter. This mitigates certain environmental impacts of copper processing.

Keywords: copper slag, flotation, concentrate smelting

RESUMEN

Se estudió la flotación de escoria de cobre en una planta concentradora de la Región de Atacama, Chile. El estudio consistió en la caracterización física, química y mineralógica de la escoria de cobre, además de las pruebas preliminares de flotación. Este artículo se enfoca en la flotación industrial, la cual consistió en dos campañas de un año cada una (2016 y 2017). En la primera campaña se utilizó un circuito de flotación de escorias existente en la planta. Para la segunda campaña (2017), se utilizó un circuito de flotación de sulfuros, más una etapa adicional de limpieza mediante flotación columnar. Los resultados mostraron mejora en los parámetros metalúrgicos de la segunda campaña (incluyendo mejoras en capacidad de procesamiento, ley de concentrado de cobre y recuperación metalúrgica). De las campañas de flotación de escoria de cobre, se concluyó que es posible obtener un concentrado de cobre de calidad comercial, apto para su posterior procesamiento en una fundición. Esto mitiga ciertos impactos ambientales del procesamiento de cobre.

Palabras clave: escoria de cobre, flotación, fusión de concentrado

Introduction

ENAMI (Empresa Nacional de Minería – National Mining Company) is a state-owned company from Chile, which promotes the development and growth of small and medium national mining through its metallurgical, economic, and exploration operations. The operational structure of ENAMI is directly related to the production of saleable products such as copper concentrates and copper cathodes, as well as through the purchase of minerals, concentrates, precipitates and different mining estates, including the five beneficiation plants along the country. The copper concentrates and precipitates produced and bought by ENAMI are smelted at the Hernán Videla Lira Smelter (HVL) (Herrera, 2018).

HVL smelter operations started in 1952, and, as of today, it has become a strategic pillar of ENAMI. The capacity of this smelter is 300 kt/y, it and entails concentrate smelting in one Teniente Converter (TC) of 4 x 15 m, the converting of copper matte in two Peirce-Smith converters (PSC), and the recovery of some valuable metals from slag in one electric

slag cleaning furnace (SCF) Devia, Parra, Queirolo, Sánchez, and Wilkomirsky, 2019). The flowsheet of the HVL smelter is presented in Figure 1.

[1] Metallurgical engineer, Universidad de Concepción, Chile. Ph.D. in Metallurgical Engineering, Universidade Federal de Minas Gerais, Brasil. Affiliation: Departamento de Ingeniería en Metalurgia and Centro Regional de Investigación y Desarrollo Sustentable de Atacama (CRIDESAT), Universidad de Atacama. E-mail: osvaldo.pavez@uda.cl

[2] Metallurgical engineer, Universidad de Atacama, Chile. Affiliation: Planta Manuel Antonio Matta, Empresa Nacional de Minería (ENAMI). E-mail: paherrera@enami.cl

[3] Metallurgical engineer, Universidad de Atacama, Chile. Affiliation: Planta Manuel Antonio Matta, Empresa Nacional de Minería (ENAMI). E-mail: magonzalez@enami.cl

[4] Metallurgical engineer, Universidad de Atacama, Chile. Affiliation: Centre for Pyrometallurgy, Department of Materials Science and Metallurgical Engineering, University of Pretoria, South Africa. E-mail: oscar.rivera.likao@gmail.com
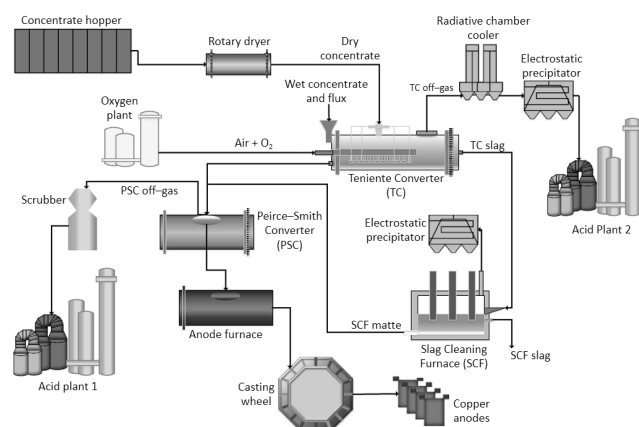
Figure 1. Flow diagram of HVL smelter (redrawn by authors).
Source: Couble (2016).

The main concentrate supplier from ENAMI for the HVL smelter is the Manuel Antonio Matta concentrator plant (MAM). MAM is the ENAMI main beneficiation plant. It is located 1 km away from the HVL smelter. The operation of MAM started in 1965 with a nominal capacity of 6 500 tons per month, which has increased to 110 000 tons in 2020 (Herrera, 2018).

The decrease in copper prices between 2015 and 2017 generated a decrease in the material fed to the smelter, especially in the product supplied by the MAM plant. In 2015, 100 000 tons of concentrate were produced by MAM, whereas, in 2017, it decreased to 40 000 tons. This shortage increased production costs and decreased the copper concentrate output (Tuck, 2019). The strategy adopted by ENAMI to increase the copper concentrate inventory was reflected on the evaluation and implementation of a new copper source: the flotation of copper slag (CS) from the HVL smelter by using the existing CS flotation circuit in the plant.

Background for the present study

In general, slags from the copper industry are rich in iron oxide, silica, calcium oxide, and alumina, and they are commonly deposited and stocked in landfills as their final destination. The worldwide production of slag in the copper industry is approximately 24,6 Mton, out of which 3,0 Mton is attributable to Chilean producers (Gorai, Jana, and Premchand, 2003; Valenzuela, 2016). Besides the undesirable gangue components such as oxides, silicates and amorphous glass, CS can exhibit valuable metal contents as high as 4-8 mass% Cu in converter slags, while smelter slags usually contain 1-2 mass% Cu. Copper can occur in slags as (a) dissolved copper, present mostly as Cu^+ ions, and (b) mechanically entrained droplets of matte (Schlesinger, King, Sole, and Davenport, 2011).

The substantial amount of copper and the massive amount of discarded slags has motivated the reprocessing of this metallurgical waste, which nowadays represents a promising secondary source of valuable products. Additionally, a global concern about the environment and new regulations have brought a reengineering of the mining industry, aimed to integrate the concept of sustainable metallurgy throughout the production process (Sibanda, Sipunga, Danha, and Mamvura, 2020). Extensive research has been carried out in order to maximize the recovery of valuable metals from CS. In general, the methods for copper recovery from slags can be classified into three categories, namely physical separation (flotation, magnetic separation); pyrometallurgy (roasting); and hydrometallurgy (leaching) (Guo, Zhu, Pan, Wu, and Zhang, 2016; Wang and Erdenebold, 2020).

Several studies on CS flotation have been reported in the literature. Sibanda et al. (2020) indicated that copper recovery from CS can be enhanced through a thorough understanding of the mineralogy and liberation profile of the slag, together with an optimization on the flotation reagents. Fan, Li, Wei, Li, and Sun (2017) concluded that three factors affect CS flotation: particle fineness, collector type, and pH. They achieved a concentrate with a copper grade of 14,47% and copper recovery of 79,66%, by milling 80% under 74 μm, by using 50 g/t of butyl xanthate as a collector and adjusting to a pH of 10 with Na_2CO_3.

Shamsi, Noaparast, Shafaie, and Gharabaghi, (2015) studied the effect of collector synergism on flotation recovery of copper from copper smelting slags. To increase copper recovery, a mixture of 6 g/t Z6, 4 g/t Z11, 30 g/t AERO 3477, and 20 g/t AERO 208 was used to determine the synergistic effect of collectors on copper recovery. The flotation tests at optimal conditions (mixture of collectors) resulted in an increase from 62,23 to 80,27%.

Guo et al. (2016) developed a new technology to improve the beneficiation of copper and iron components from copper slag, by modifying the molten slag to promote the mineralization and grain growth of the valuable compounds. Results showed that, under the proper conditions, the copper grade of the rougher stage increased from 6,43% to 11,04%; the iron recovery of magnetic separation significantly increased from 32,40% to 63,26%; and other evaluation indexes slightly changed in comparison with unmodified copper slags.

Tong, Han, Ren, and Yang (2014) studied the effect of grinding fineness, pH, and collector type and dosing on copper slag flotation. The results showed that, after a grinding degree of 90% under 74 μm, pH 6,0, 80 g/t of XT–53 as collector, and 30 g/t of 2# oil as collector, a concentrate with copper grade of 23,55% and copper recovery of 85,61% was obtained.

Xue, Li, and Qin (2016) studied the flotation of slowly cooled CS from the Ausmelt furnace. These researchers reported that, by using butyl xanthate as collector, a concentrate with copper grade of 16,11% and copper recovery of 69,90% was achieved. The copper grade on tailings was only 0,2%.

Another aspect that can affect both the milling and flotation of CS is the cooling behavior of the slag. Several researchers have reported that slow cooling of the slag can lead to an improvement in copper recovery because of the segregation of some valuable elements such as copper, silver, and

molybdenum during the solidification and further cooling (Mihajlović, Kamberović, Korać, Gavrilovski, and Jovanović, 2015; Voisin, Pizarro, and Ossandon, 2017).

Therefore, this paper describes the evaluation of two industrial circuits for CS flotation in two campaigns: 2016 and 2017. The existing CS flotation circuit in the plant was used in 2016. In 2017, a concentrate flotation circuit with a column flotation cleaning stage was evaluated. The aim was to obtain a copper concentrate with copper contents of 25% or above.

Materials and methods

Characterization of copper slag from HVL smelter

The CS used in the laboratory tests and industrial campaigns was collected from the HVL smelter main slag landfill. Samples were characterized by particle size distribution (PSD), specific weight, Bond Index (Wi), chemical analysis, mineralogical analysis, and flotation tests.

PSD was determined in a Ro-Tap unit with sieves from 6# to 200# ASTM. Specific weight was obtained through the Le Chatelier method. The Bond Index was determined in a milling-classification closed circuit, in a 12" x 12" mill at 70 RPM. The load consisted of 285 balls with diameters from $1^1/_2$" to $3/_4$" and a ball mass of 20,125 kg. An ASTM 140# (106 μm) mesh was used for this test.

Chemical composition was determined through an atomic absorption mass spectrometry. The mineralogical analysis consisted of optical microscopy and X-ray diffraction analysis (XRD) with a Shimadzu XRD-6100 (Cu Kα) diffractometer. The quantification of crystalline phases was obtained from Rietveld refinements of the XRD patterns.

The flotation stage was performed in a Denver D-12 cell. It was carried out under the following conditions: PSD from 60% to 80% under 200# (ASTM); pH = 8,0; 40 g/t of F-503 (collector) and 30 g/t of H-70 (froather). These operational conditions were suggested by the Process Engineering and Chemical Laboratory staff from the plant.

Industrial flotation circuits

Figure 2 shows the circuit used during the 2016 campaign. It consists of three ball mills operated in a closed circuit. Hydrocyclone underflow is recycled for regrinding, while the overflow is sent to a conditioning stage before the rougher-scavenger stage. This stage consists of twelve Dorr Oliver cells of 300 ft^3, distributed in four cells for each flotation stage (rougher, cleaner and scavenger).The recovery of sulfides takes place in the the rougher and scavenger stages, then the product is sent to the cleaner stage to improve the copper grade of the concentrate. The concentrate is then transported to a thickener and filtered in a ceramic filter.

In 2017, a second alternative was evaluated: an existing flotation circuit for sulfide ores (Circuit Nr. 2) with a columnar cell as a cleaner stage. Figure 3 shows the flowsheet of this circuit. It consists of a set of five ball mills operating simultaneously, which increase the CS flotation capacity up
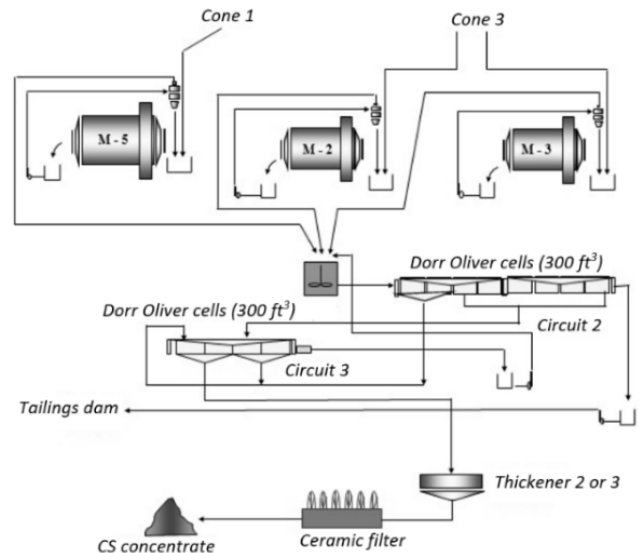
Figure 2. Circuit Nr. 1 (2016).
Source: Couble (2016)

to 100 t/h. The rougher stage consists of seven Outokumpu cells (565 ft^3), the cleaner stage of a columnar cell, whilst a scavenger stage processes the tailings from the cleaner stage. The scavenger stage consists of eight Outokumpu cells divided into four cells of 8 m^3 cells and six cells of 3,0 m^3. The circuit also has Outokumpu mechanical cells (20 m^3 and 40 m^3) and a regrinding stage for the rougher concentrate.
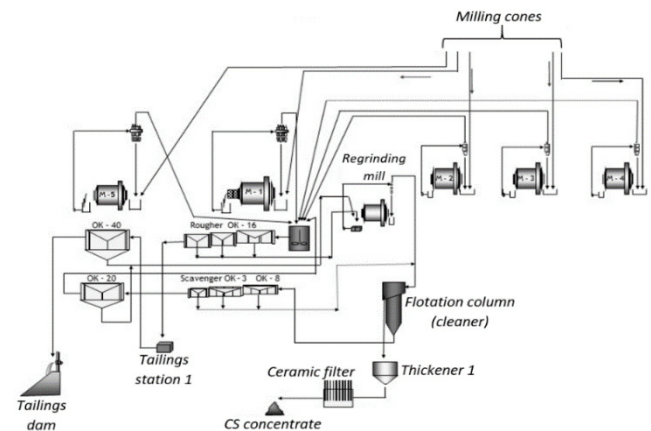
Figure 3. Circuit Nr. 2 (2017).
Source: Couble (2016)

Results

Characterization of copper slag

Table 1 shows the results of the physical characterization of CS: F$_{80}$, density, and Bond Index.

The CS samples showed a density of 3,30 g/cm^3, similar to what was reported by Valderrama, Gonzalez, Santander and Zazzali, (2018) for reverberatory furnace slag from the same smelter (HVL). Nazer, Pavez, Rojas, and Aguilar (2010) reported a density of 3,817 g/cm^3 for samples obtained from

the same deposit as the present study. Velásquez (2018) reported a density of 3,92 for slags from Potrerillos smelter (Atacama, Chile), while Cendoya (2009) reported a density of 4,0 g/cm^3 for another Chilean copper smelter slag. The Bond index was 22,6 kWh/t. This value is higher than normal copper ores, which normally present a Bond Index between 13,0 and 20,0 kWh/t (Nazer *et al.*, 2010; Cendoya, 2009; Valderrama *et al.*, 2018).

Table 1. Physical characterization of the copper slag

F_{80} (µm)	Density (g cm^{-3})	Bond Index (kWh ton^{-1})
2 360	3,30	22,6 ± 1.1

Source: Authors

In mineral comminution, material abrasiveness, pulp environment and particle size, are the most important factors influencing the wear of the linings and grinding media in ball milling. For the HVL smelter slag, Valderrama *et al.* (2018) reported a high abrasion index (0,912 g/h), which would imply a high consumption of steel (linings and grinding media).

Table 2 presents the chemical analysis results of the CS sample. The slag presented 0,53% Cu and high amounts of iron and silicon. Valderrama *et al.* (2018) reported a similar chemical composition, with a different copper percentage in CS.

Table 2. Chemical composition of the CS (normalized)

Component	Fe_T	SiO_2	CaO	Al_2O_3	Na_2O	K_2O	MgO	Cu	S
wt %	36,32	41,11	8,36	8,10	2,22	1,23	1,53	0,58	0,55

Source: Authors

Chemical and mineralogical analyses indicated 0,58% copper and 0,55% sulfur; high amounts of iron (33,3%) and silica (17,7%); substantial amounts of calcium oxide (5,50%) and alumina (3,95%); and minor amounts of sodium, potassium, and magnesium oxides. These values are consistent with the chemical composition of ancient and recent CS from Atacama (Cardona, Coursol, Vargas, and Parra, 2011; Nazer *et al.*, 2010; Pavez, Nazer, Rivera, Salinas, and Araya, 2019). On the other hand, although copper can be as dissolved oxide, it is commonly found as entrained grains of bornite and chalcopyrite. Nazer *et al.* (2010) reported a 0,75% copper grade, with iron and silicon as the most important constituents in CS from the same smelter.

Table 2 shows the quantification of crystalline phases of the laboratory flotation tests. The CS (feed) is constitued by fayalite (Fe_2SiO_4) and magnetite (Fe_3O_4). No sulfides or copper oxides were detected, probably because their concentrations were below the XRD detection limits. The concentrate contained not only bornite ($Cu_{1,375}Fe_{0,275}S$) and chalcopyrite ($CuFeS_2$), but also a considerable amount of fayalite and magnetite. The tailings did not show other compounds but fayalite and magnetite (80,4% and 19,6%, respectively).

Table 3. Quantitative XRD analyses of the feed, concentrate and tailings from the laboratory tests

Stream	Mineralogical composition (wt%)
Feed	Fayalite (76,7%); magnetite (23,3%)
Concentrate	Bornite (37,6%); fayalite (30.4%); magnetite (18,5%); chalcopyrite (13,6%)
Tailings	Fayalite (80,4%); magnetite (19,6%)

Source: Authors

Nazer *et al.*, (2010) reported fayalite (50%), magnetite (39%) and magnesium fayalite (10%) as main constituents of the CS from HVL smelter. Cardona *et al.*, (2011) studied the solidification of SCF slag from the HVL smelter under fast and moderate cooling rates. They found that, under fast cooling rates the presence of fayalite, magnetite and glassy phases predominate, whilst the main phases to crystallise under moderate cooling rates are magnetite and fayalite (Nazer *et al.*, 2010; Cardona *et al.*, 2011).

The high amounts of fayalite and magnetite in the CS concentrate are due to high the degree of association between sulfides and slag, as shown in Figure 4. However, CS milling must be carried out in a very controlled way, as the excess of fine particles can lead to clogging of the piping and pumping systems. Some sulfides (bright grey) are closely associated and enclosed within larger slag particles (dark grey), which results in the unavoidable transport of slag to the concentrate.
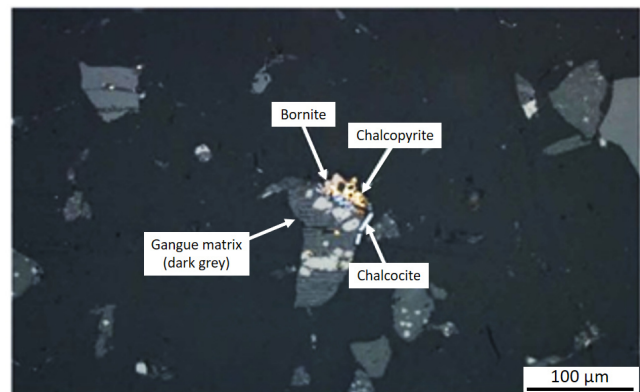
Figure 4. Micrograph (optical microscopy) showing sulfides attachment to slag.
Source: Authors

Laboratory flotation tests

Figure 5 shows the flotation test results, with copper recoveries from 59,0% to 62,0% for the total copper, and 62,0% to 64,9% for insoluble copper. There were no considerable differences in recoveries of both total and insoluble copper from 60% to 80% under 200# ASTM (74 µm).

According to the industrial observations of the MAM plant, a coarse PSD (60% to 65% under 200# ASTM) can lead to clogging in the mill discharge pipes, as well as hydrocyclone overflow due to the fact that the pulp settles inside the hoses

and pipes. On the other hand, a fine PSD (70% to 80% under 200# ASTM) results from overgrinding, thus increasing the energy cost of the comminution process.
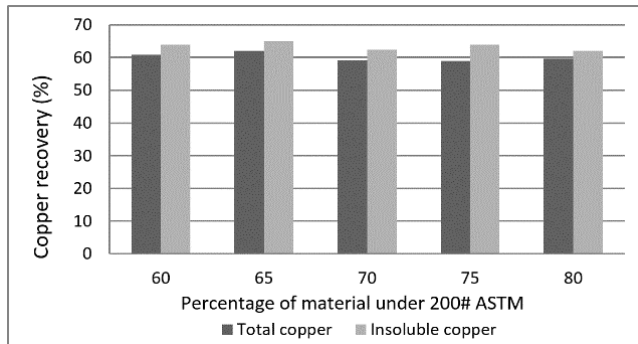
Figure 5. Metallurgical recovery of total and insoluble copper as function of PSD.
Source: Authors

Industrial campaign (2016) – Circuit Nr. 1

Figures 6 and 7 show the copper grades and recoveries achieved by Circuit Nr. 1 in July (17 days) and August (25 days) of 2016. The copper grade in July was lower than in August, but the recovery in July was higher. During that month, 10 587 tons of CS were processed, and the copper concentration in the concentrate oscillated between 14,69% and 19,97% (16,92% on average). The average copper recovery was 73,93%. In August, the processing of 15 614 tons of CS yielded copper grades in the concentrate from 13,55% to 23,30% (18,22% on average), while the average copper recovery was 71,99%.
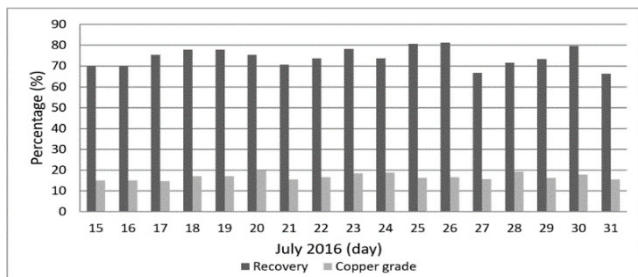
Figure 6. Circuit Nr. 1 (campaign of 2016).
Source: Authors
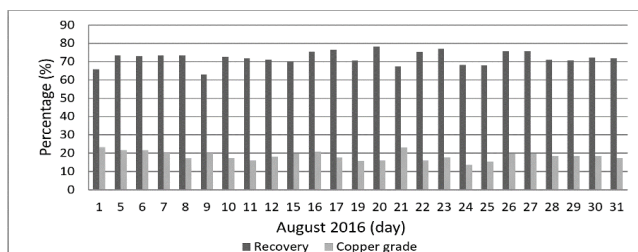
Figure 7. Circuit Nr. 1 (campaign of 2016).
Source: Authors

The results showed that the copper grade in the final concentrate was not commercially satisfactory. The main

limitation of the circuit was the lack of a cleaner stage to increase the copper grade in the final concentrate.

Industrial campaign (2017) – Circuit Nr. 2

Figures. 8 and 9 present the copper grades and recoveries achieved by Circuit Nr. 2 in June (14 days) and August (22 days). In August, the copper grade in the concentrate and recovery were higher than in June. During the latter, the processing of 29 480 tons of CS led to copper grades in concentrate from 12,01% to 27,41% (21,27% on average), while the average copper recovery was 71,93%. In August, the plant beneficiated 34 045 tons of CS resulting in copper grades in concentrate from 7,5% (which is highly unusual) to 32,81% (25,42% on average), with an average recovery of 75,80%.
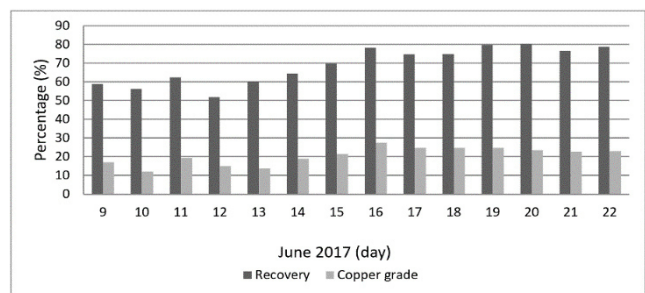
Figure 8. Metallurgical recovery and copper grade (Circuit Nr. 2 – June, 2017).
Source: Authors
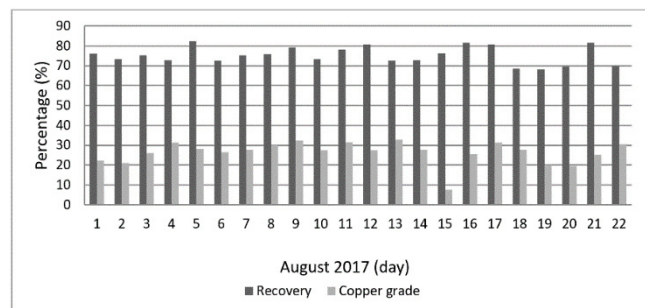
Figure 9. Metallurgical recovery and copper grade (Circuit Nr. 2 – August, 2017).
Source: Authors

From Figures 8 and 9, it is clear that Circuit Nr. 2 showed a higher performance than Circuit Nr. 1 in processing capacity, copper grade of concentrate, and copper recovery. There is also a potential further improvement in copper recovery by adding a scavenger stage for rougher tailings. The scavenger stage was not in the circuit design due to the high copper recovery in the rougher stage (~95%) of the sulfide ores processed in the plant.

The summary of the main parameters of the studied circuits is presented in Table 4. From the presented data, it is clear that only in the industrial campaign in 2017 (Circuit Nr. 2) was the obtained concentrate comercially acceptable (copper grade above 25 mass%). The capacity of the second Circuit was substantially higher (about three times) than

Circuit Nr. 1, even though the variabilty of Circuit Nr. 2 was considerably higher than the first. Finally, both circuits exhibited a similar copper recovery.

The higher performance of Circuit Nr. 2 in terms of copper grade is due to the columnar cleaner stage and the presence of five ball mills. Sipunga (2015) reported improvements in copper recovery through the addition of a regrinding stage to the flotation circuit. This researcher reported a recovery of 75,8% in the first flotation stage and an increase of up to 92,2% by adding a regrinding stage for rougher tailings.

Table 4. Summary of average copper grades (main streams), capacities and copper recoveries for circuits 1 and 2

Circuit	Copper grade (mass %Cu)			Capacity (ton per day)	Recovery (%)
	F	C	T		
1 (2016)	0,68 ± 0,05	17,36 ± 5,94	0,19 ± 0,03	623,9 ± 198,5	72,93 ± 4,18
2 (2017)	0,93 ± 0,16	24,67 ± 5,29	0,25 ± 0,03	1 764,6 ± 655,7	72,90 ± 7,54

Note: F: feed; C: concentrate; T: tailings
Source: Authors

General economic considerations

It has been shown the successful implementation of the CS processing is promoted by two main economic factors: the shortage in copper ore supply and a decrease in the price of copper between 2015 and 2017. However, it is necessary to highlight the increased costs associated to slag processing when compared to conventional copper ore processing.

The main parameters affected by CS flotation were the grinding costs and grinding media consumption. The grinding costs reached 9,41 USD/t, made up of a fixed cost of 3,05 USD/t and a variable cost of 6,36 USD/t.

It is worth noting the increase on the consumption of grinding media (1200 g/t) for the processed CS, when compared to the normal copper ore (670-890 g/t). According to Chilean Copper Comission (COCHILCO), the average grinding media consumption for the Chilean copper producers is about 700 g/t (COCHILCO, 2018). Therefore, the processing of CS represents an increase of 56% in grinding media, which notoriously affects the grinding costs.

The steep increase on the steel consumption from the grinding media, is due to the difference in the Bond Index (Wi) of the CS and copper ores. The literature reports values of 15,9-16,7 kWh/t for copper ores (Camus & Tobar, 2017; Delgado, 2013) and about 27,8 kWh/t for CS (Guarda, 2015).

Another important aspect is the reagent consuption of CS processing. Table 5 shows both the type and dosage of the reagents (collector and froather) used in the MAM plant for CS and copper ore processing. According to the literature, the consumption of reagents in CS processing substantially exceeds those ones from the copper ores, doubling the amount of collector and increasing froather consumption by about 50%.

Table 5. Types and dosages of reagents (collector and froather) used in MAM concentrator plant, for CS and copper ores processing

Raw material	Collector (g/t)	Froather (g/t)	
	Aero 3894 Promoter	Aerofroth 70	Dowfroth D–1012
Copper slag	40	15	15
Copper ore	20	20 (maximum)	

Source: Authors

Conclusions

In the 2016 campaign (Circuit Nr. 1) the plant processed 10 587 tons of CS in July. The copper grade of the concentrate ranged from 14,69% to 19,15% (16,92% on average) with a copper recovery of 73,93%. In August, 15 614 tons of CS were processed and the copper grade of the concentrate varied from 13,55% to 23,30% (18,22% on average), and the average copper recovery was 71,99%. The low copper grade in the concentrate is probably due to the lack of a cleaner stage, thus decreasing the copper grade of the final product.

In the second campaign (2017, Circuit Nr. 2), the plant benefited 29 480 tons of CS in June, with copper grades in concentrate from 12,01% to 27,41% (21,27% on average) and an average copper recovery of 71,93%. In August, by processing 34 045 tons of CS, copper grades varied from 7,5% (atypical) to 32,81% (25,42% on average). The average copper recovery was 75,80%.

Circuit Nr. 2 showed a higher performance than Circuit Nr. 1 in terms of mass flow capacity, copper grade in concentrate, and copper recovery. We suggest the addition of a scavenger stage in this circuit to process the rougher tailings. This modification could improve copper recovery in the overall process.

Because of the mineralogical composition of CS (mostly constitued fayalite and magnetite), the Bond Index value of 22,6 kWh/t is higher than the normal copper ores, which normally report a Bond Index between 13,0 to 20,0 kWh/t. This higher abrasiveness of CS when compared to an average copper ore is evidenced in a higher consumption of grinding media of about 60%. Additionally, reagent consumption is also substantially higher, doubling the collector dosage and increasing by about 50% the froather dosage. It is crucial to consider these two key economic parameters in order to have a more thorough description and understanding of the overall process.

Acknowledgements

References

Camus, F. and Tobar, M. (2017). *Determinación del índice de trabajo a menas con contenido de valor comercial de diversos sectores de la IV Región*. Chile: Universidad de La Serena. 10.13140/RG.2.2.19978.82886

Cardona, N., Coursol, P., Vargas, J., and Parra, R. (2011). The physical chemistry of copper smelting slags and copper losses at the Paipote smelter part 2 - Characterisation of industrial slags. *Canadian Metallurgical Quarterly, 50*(4), 330-340. 10.1179/000844311X13112418194806

Cendoya, P. (2009). Efecto en la Resistencia de las Escorias de Fundición de Cobre como Agregado Fino en el Comportamiento Resistente del Hormigón. *Ingeniare. Revista Chilena de Ingeniería, 17*(1), 85–94. 10.4067/S0718-33052009000100009

COCHILCO. (2018). *Análisis del mercado de insumos críticos en la minería del cobre* (Issue 2018). Chile: Gobierno de Chile. https://www.cochilco.cl/MercadodeMetales/Anali sisMercadodelosInsumosCríticos2017(empresas).pdf

Couble, C. (2016). *Revisión y actualización del método de reconciliación del Convertidor Teniente en Fundición Hernán Videla Lira ENAMI* (Master's thesis in Chemical Engineering, Universidad Técnica Federico Santa María, Spain). http://hdl.handle.net/11673/23169

Delgado, C. (2013). *Evaluación de un cambio tecnológico para el procesamiento de minerales de alta dureza*. Chile: Universidad de Chile. http://repositorio.uchile.cl/ha ndle/2250/114434

Devia, M., Parra, R., Queirolo, C., Sánchez, M., and Wilkomirsky, I. (2019). Copper smelting and converting: past and present Chilean developments. *Mineral Processing and Extractive Metallurgy: Transactions of the Institute of Mining and Metallurgy, 128*(1-2), 108-116. 10.1080/25726641.2018.1542050

Fan, J., Li, H., Wei, L., Li, C., and Sun, C. (2017). The Recovery of Copper from Smelting by Flotation Process. In T. P. (eds) Wang S., Free M., Alam S., Zhang M. (Ed.), *Applications of Process Engineering Principles in Materials Processing, Energy and Environmental Technologies*. An EPD Symposium in Honor of Professor Ramana G. Reddy. Springer International Publishing AG. 10.1007/978-3-319-51091-0_21

Gorai, B., Jana, R. K., and Premchand. (2003). Characteristics and utilisation of copper slag - A review. *Resources, Conservation and Recycling, 39*(4), 299-313. 10.1016/S0921-3449(2)00171-4

Guarda, N. (2015). *Efecto del enfriamiento controlado en el consumo de energía y la recuperación de valiosos en el procesamiento de escorias de fusión de cobre*. Chile: Universidad de Chile. http://repositorio.uchile.cl/handle /2250/137113

Guo, Z., Zhu, D., Pan, J., Wu, T., and Zhang, F. (2016). Improving Beneficiation of Copper and Iron from Copper Slag by Modifying the Molten Copper Slag. *Metals, 6*(4), 86. 10.3390/met6040086

Herrera, P. (2018). *Evaluación de circuitos de flotación de escoria en Planta Manuel Antonio Matta* (Metallurgical Engineering Thesis, Universidad de Atacama, Atacama Chile).

Mihajlović, A., Kamberović, Ž., Korać, M., Gavrilovski, M., and Jovanović, N. (2015). The effect of primary copper slag cooling rate on the copper valorization in the flotation process. *Metallurgical and Materials Engineering, 21*(2), 127-141. 10.30544/102

Nazer, A., Pavez, O., Rojas, F., and Aguilar, C. (2010). Una Revisión de los usos de las escorias de cobre. X CONAMET/SAM, 1, 5. http://iberomet2010.260mb.com /pdfcongreso/t5/T5-36_nazer_n1_FINAL.pdf

Pavez, O., Nazer, A., Rivera, O., Salinas, M., and Araya, B. (2019). Copper slag from different dumps in the Atacama Region used in mortars as partial replacement of cement. *Revista Materia, 24*(2). 10.1590/s1517-707620190002.0664

Schlesinger, M., King, M., Sole, K., and Davenport, W. (2011). *Extractive Metallurgy of Copper* (Fifth edition). Amsterdam, Netherlands: Elsevier.

Shamsi, M., Noaparast, M., Shafaie, S. Z., and Gharabaghi, M. (2015). Synergism effect of collectors on copper recovery in flotation of copper smelting slags. *Geosystem Engineering, 19*(2), 57-68. 0.1080/12269328.2015.1087349

Sibanda, V., Sipunga, E., Danha, G., and Mamvura, T. A. (2020). Enhancing the flotation recovery of copper minerals in smelter slags from Namibia prior to disposal. *Heliyon, 6*(1) E03135. 10.1016/j.heliyon.2019.e03135

Sipunga, E. (2015). *Optimization of the flotation of copper smelter slags from Namibia Custom Smelters 'Slag Mill Plant* (Master's Thesis University of the Witwatersrand, Johannesburg, South Africa). http://wiredspace.wits.ac.z a/handle/10539/20110

Tong, X., Han, B., Ren, S. P., and Yang, B. (2014). Recovery of copper from copper smelter slag by flotation. *Applied Mechanics and Materials*, 496-500, 406-409. 10.4028/www.scientific.net/AMM.496-500.406

Tuck, C. A. (2019). Iron Ore. In U.S. Geological Survey (Eds.) *Mineral Commodity Summaries 2019*. Reston, VA: U.S. Geological Survey. 10.3133/70202434

Valderrama, L., Gonzalez, M., Santander, M., and Zazzali, B. (2018). Recuperación de cobre contenido en escoria de cobre mediante flotación. *Holos, 5*, 40-50. 10.15628/holos.2018.7118

Valenzuela, A. (2016). Mining Waste Management in Chile: Experience, Challenges and Opportunities. Paper presented at *XIV Congreso Internacional Expomin 2016*: Workshop on best practices on mining policies and technologies. Thematic session 2 - Mining waste management and mine rehabilitation. Santiago, Chile.

Velásquez, V. (2018). *Optimización de la recuperación de cobre en el circuito de flotación de Codelco-El Salvador en base a la evaluación de nuevas formulaciones de reactivos de flotación* (Metallurgical Engineering Thesis, Universidad de Concepción, Concepción, Chile). http://repositorio.ud

ec.cl/jspui/bitstream/11594/3058/4/Tesis_Optimizacio
n_de_la_recuperacion_de_cobre.Image.Marked.pdf

Voisin, L., Pizarro, C., and Ossandon, J. (2017). *Determination of the behaviour of valuable metals during the controlled cooling of copper smelting slags to clarify their recovery by grinding and flotation*. Paper presented at the 5th International Slag Valorisation Symposium. https://cutt.ly/BzBJ7TM

Wang, J.-P. and Erdenebold, U. (2020). A study on reduction of copper smelting slag by carbon for recycling into metal values and cement raw material. *Sustainability, 12*(1421). 10.3390/su12041421

Xue, P., Li, G., and Qin, Q. (2016). Recovery of copper from slow cooled ausmelt furnace slag by floatation. *Characterization of Minerals, Metals, and Materials 2015*, 621-628. 10.1007/978-3-319-48191-3_78

Fuzzy Logic Control for a Soft Exoskeleton Glove Using a Motor-Tendon Actuator

Control de lógica difusa para un guante de exoesqueleto suave que utiliza un actuador motor-tendón

Joga Dharma Setiawan[1], Mochammad Ariyanto[2], Sri Nugroho[3], Rifky Ismail[4], Tedi Purbayanto[5], and Haeryip Sihombing[6]

ABSTRACT

A hand is one of the essential limbs on the human body that is used for daily activities. The aim of this research is to develop a soft exoskeleton hand to assist people with hand deterioration. The developed exo-glove is made of low-cost RTV (room-temperature vulcanizing) silicone rubber with a motor-tendon actuation system that produces the flexion and extension motion. Here, the actuator converts rotation motion into linear motion from DC motor, while a potentiometer sensor is utilized to measure the rotation angle on the actuator system, in which fuzzy logic control (FLC) is employed for controlling the motion of the proposed motor-tendon actuator. To validate the function and mechanism of the developed soft exoskeleton glove, testing was conducted towards the FLC performance on the healthy human hand for various object grasping tests. Based on the test results, this study shows that the soft glove can be implemented on the human hand as an assistive device.

Keywords: fuzzy logic control, soft exoskeleton glove, assistive device, motor-tendon actuator

RESUMEN

La mano es una de las extremidades más importantes del cuerpo humano que se utiliza para actividades de la vida diaria. El objetivo de esta investigación es desarrollar una mano exoesqueleto suave para ayudar a las personas con la mano deteriorada. El exo-guante desarrollado está hecho de caucho de silicona RTV (vulcanización a temperatura ambiente) de bajo costo con un sistema de accionamiento motor-tendón que produce el movimiento de flexión y extensión. Aquí, el actuador convierte el movimiento de rotación en movimiento lineal del motor de DC, mientras que se utiliza un sensor de potenciómetro para medir el ángulo de rotación en el sistema del actuador, en el que se utiliza el control lógico difuso (FLC) para controlar el movimiento del actuador motor-tendón propuesto. Para validar la función y el mecanismo del exo-guante blando desarrollado se realizaron pruebas para lograr el rendimiento de FLC en la mano humana sana en varias pruebas de agarre de objetos. Según los resultados de la prueba, este estudio muestra que el guante blando se puede implementar en la mano humana como un dispositivo de asistencia.

Palabras clave: control de lógica difusa, exoesqueleto blando, dispositivo de asistencia, actuador motor-tendón

[1]Mechanical Engineer, Diponegoro University, Indonesia, Ph.D. in Mechanical Engineering, Michigan State University, USA. Affiliation: Diponegoro University, Indonesia. E-mail: joga.setiawan@ft.undip.ac.id
[2]Mechanical Engineer, Diponegoro University, Indonesia, M.Sc. in Mechanical Engineering, Diponegoro University. Affiliation: Diponegoro University, Indonesia. E-mail: mochammad_ariyanto@ft.undip.ac.id
[3]Mechanical Engineer, Diponegoro University, Indonesia, Ph.D. in Mechanical Engineering, Tohoku University, Japan. Affiliation: Diponegoro University, Indonesia. E-mail: srinugroho2004@yahoo.com
[4]Mechanical Engineer, Diponegoro University, Indonesia, Ph.D. in Mechanical Engineering, Twente University, The Netherlands. Affiliation: Center for Biomechanics, Biomaterial, Biomechatronics, and Biosignal processing (CBIOM3S), Diponegoro University, Indonesia. E-mail: rifky_ismail@ft.undip.ac.id
[5]Mechanical Engineer, Diponegoro University, Indonesia, B.Sc. in Mechanical Engineering, Diponegoro University. Affiliation: Diponegoro University, Indonesia. E-mail: tedipurbayanto@gmail.com
[6]Mechanical Engineer, University Teknikal Malaysia Melaka, M.Sc. in Mechanical Engineering, Universitas Pelita Harapan, Indonesia. Affiliation: University Teknikal Malaysia Melaka, Malaysia. E-mail: iphery@utem.edu.my

Introduction

The hand is one part of the human body that has a significant role in carrying out daily activities. People with hand disabilities require a wearable robot that can help them perform as they did before. Two types of wearable robots are widely used for people with hand disabilities: prostheses and exoskeletons. Prosthetic hands, especially myoelectric hands, are an option for people who have lost a hand. There are many commercially available devices of this kind in the market today, but their price is not low enough (Ku, Lee, Park, Lee, and Jeong, 2019). Marks and Michael (2001) even stated that the cost have quadrupled as microprocessor control has steadily increased. Birnbaum (2016) stated in his report that these devices are a luxury rather than a necessity. The World Health Organization (Hill and Krug, 2017) underlined that, without access to prostheses or orthoses, people who need them are often excluded, isolated and condemned to poverty. Based on this, many researchers have been

developing 3D-printed myoelectric hands intended as low-end products (Sreenivasan *et al.*, 2018; Yoshikawa, Sato, Higashihara, Ogasawara, and Kawashima, 2015; Slade, Akhtar, Nguyen, and Bretl, 2015; Kamikawa and Maeno, 2008). A myoelectric hand can be operated by the wearer through an electromyography sensor that is placed on the remainder of the human limb. This sensor can read EMG signals from residual nerves through muscle contractions, but there are still many flaws (Balciunas, Murphy, and Zdonbinski, 2019; Geethanjali, 2016). Most devices still use hard robot technology and are limited to EMG signal acquisition (Ribeiro *et al.*, 2019).

Researchers from around the world have developed exoskeleton hands by using hard materials or hard robot technology. People with impaired hands such as stroke hand issues or brachial plexus injuries need an exoskeleton hand to assist their motion. The exoskeleton is aimed to assist and provide mechanical support for the human joints in the hands, fingers, elbows, etc. A hard exoskeleton hand is rigid and easier to control than its soft variant. However, it is limited in the sense that it is hard to align with a human hand, not comfortable, and still heavy (Ho *et al.*, 2011; Pu, Chang, Pei, Kuo, and Wang, 2016; Gearhart, Varone, Stella, and BuSha, 2016; Ismail, Ariyanto, Pambudi, Syafei, and Ananto, 2017).

Recently, many researchers have developed soft exoskeleton hands to overcome these limitations, even though they are more difficult to control. Three types of commonly used actuation systems in soft exoskeleton are pneumatic network (Polygerinos *et al.*, 2013; Yun, Kang, and Cho, 2017; Yap *et al.*, 2015, 2016), shape memory alloy (SMA) (Villoslada, Flores, Copaci, Blanco, and Moreno, 2015; Hadi, Alipour, Kazeminasab, and Elahinia, 2018), and motor-tendon actuation (Randazzo, Iturrate, Perdikis, and Millán, 2018; Kim, In, Lee, and Cho, 2017; In, Kang, Sin, and Cho, 2015). The control design and actuation system for these hands have become one of the most challenging issues in developing soft exoskeleton robots. Soft exoskeleton hands have are now a potential wearable robot and an assistive device for people with impaired hands. They also can be used for hand rehabilitation purposes.

According to the above, this study develops a wearable soft exoskeleton glove that will be used as an assistive device for people with impaired hands. A soft glove is generated by using RTV (room-temperature vulcanizing) silicone rubber material, while the actuator system is a motor-tendon actuator incorporating fuzzy logic control. Two Bowden cables are used as power transmitters from the motor-tendon actuator to the soft glove to perform flexion and extension movements as mechanical support. After the soft exoskeleton glove prototype is developed, a test on a healthy human hand is conducted to determine the performance of the robot. Aditionally, the grasping test is performed using various objects with different shapes, sizes, and masses.

Methodology

A soft exoskeleton glove

This study begins to model the soft exoskeleton glove by determining the average dimensions of the fingers and hands for brachialis plexus injury patients, in order to get the best glove size configuration. Modeling is carried out by developing a 3D design using CAD software (SolidWork®). The 3D soft glove design is shown in Figure 1, and the next step is to design a mold design based on it.

Synthetic rubber is used as a soft glove material. According to its manufacturing temperatures, there are two types: those that require heating and those that do not, which are called RTV (room-temperature vulcanization) silicone. RTV silicone has many types based on the type of mixture, stiffness, and heat resistance. In this study, RTV silicone rubber was chosen as the material for the soft glove because it makes the manufacturing process easier. This process does not require heating, and this study worked at low temperatures. Several types of materials such as RTV 48, RTV 52, and RTV Platinum were used, out of which the latter was chosen since it has the highest stiffness. During the casting process, RTV Platinum can enter and fill the narrow gaps in the soft glove mold to yield better results. Soft exoskeleton glove manufacturing results are shown in Figure 1.

(a) (b)
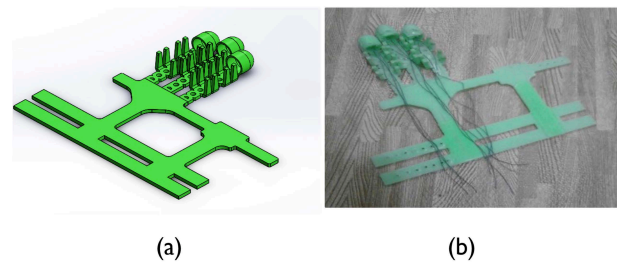
Figure 1. Soft exoskeleton glove: (a) 3D design, (b) manufacturing results.
Source: Authors

Motor-tendon actuator

This section discusses the kinematic modeling of the motor-tendon actuator based on the rotation pattern of the servo motor, which is used as the main driver to pull the sheath tendon. The modeling discusses the kinematic model of x displacement for the motor-tendon actuator to model linear displacement into potentiometer sensor rotation (position control).

Figure 2 shows the design configuration of the motor-tendon actuator. It is worth noting that the purpose of kinematic modeling is to provide feedback control to the used actuator - in this case, a DC motor. Feedback is a signal from the potentiometer sensor in the actuator system. The potentiometer used in this study has a range of motion of $270°$, while the DC motor rotation pulls the tendon-sheath from the normal position to the full grip position that requires more than one rotation. Therefore, a rotary reduction between the potentiometer and the DC motor is needed, so that the

actuator rotation does not exceed the range of motion of the potentiometer. Figure 3 shows a reduction system using four pulleys.

(a)

(b)
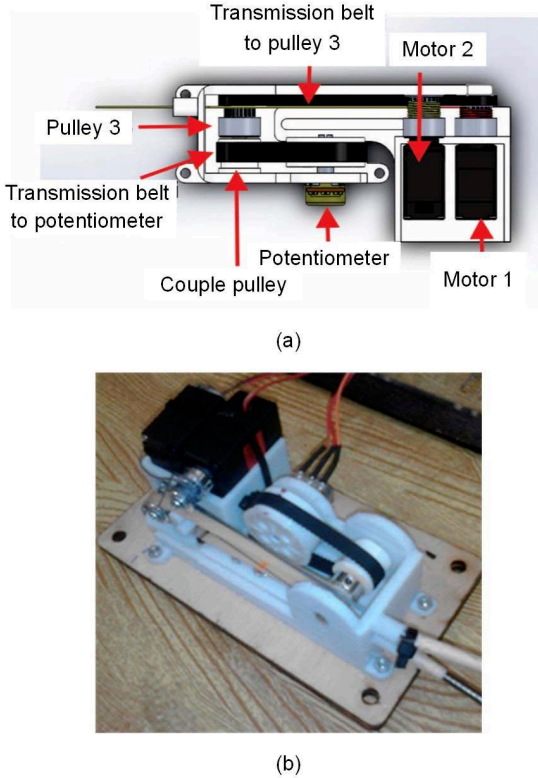
Figure 2. Motor-tendon actuator design; (a) top view, (b) prototype.
Source: Authors
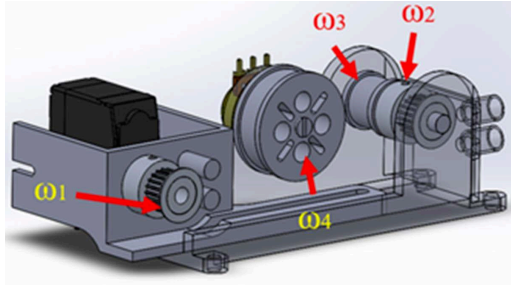
Figure 3. Gear reduction system on the motor-tendon actuator.
Source: Authors

The DC motor pulley is represented by ω_1 as the initial reference point of the round, which acts as an actuator, while the pulley on the coupled shaft is represented by ω_2 and ω_3. The potentiometer pulley is represented by ω_4. The calculation of the reduction system has the purpose of determining how much reduction occurs in the motor-tendon actuator. This reduction pulley calculation starts from the pulley of a DC motor. Pulleys 1 and 2 are connected to the belt so that their linear velocity is the same. Thus, the equation can be written as follows:

$$\omega_1 r_1 = \omega_2 r_2 \tag{1}$$

where $r_1 = r_2$, then $\omega_1 = \omega_2$.

Pulleys 2 and 3 are coupled using a shaft so that there is a relation between them. Pulleys 3 and 4 are connected by a belt so that the linear speed between the two pulleys is the same, and the equation can be written as follows:

$$\omega_3 r_3 = \omega_4 r_4 \tag{2}$$

Based on calculations in Equations (1), (2), and (3), a range of motion can be found from the sheath tendon. The diameter of a DC motor pulley is 10 mm, the maximum analog to digital converter (ADC) value from the potentiometer in the motor-tendon actuator is 746, and the minimum ADC value is 97. The calculation of the range of motion from sheath tendon is stated in Equation (3), (4), and (5).

$$\theta_4 = \frac{(ADC_{\max} - ADC_{\min})}{1023} \times 360° = 242,46° \tag{3}$$

$$\frac{\theta_1}{\theta_4} = \frac{\omega_1}{\omega_4} = 727,39° \tag{4}$$

$$x = \pi d_1 \frac{\theta_1}{360°} = 36,4 \, \text{mm} \tag{5}$$

From the results of these Equations, the obtained length of the tendon pull is 36,4 mm.

The development of the exoskeleton glove was conducted in our previous study (Setiawan, *et al.*, 2020). Some of the soft exoskeleton glove and motor-tendon actuator manufacturing processes have been described in the research. After the manufacturing processes, the assembly process of all components, including the soft glove, the motor-tendon actuator, the motor-tendon actuator case, two Bowden cables, and electrical components were carried out. The wearable robot soft exoskeleton glove that has been completed through the assembly process is shown in Figure 4. The motor-tendon actuator can be worn on the waist of the user/wearer.

Figure 4. Overall final prototype of soft exoskeleton glove.
Source: Authors

Control Mechanism

The selected method for controlling the employed DC motor is fuzzy logic control (FLC), whose implementation stages will be presented in this section. There are three main components in a FLC design: input, rule, and output. The output value used in the FLC is the pulse width modulation (PWM) value. The PWM value adjusts the movement of the motor clockwise or counterclockwise and increases or decreases the speed of the DC motor. The rule component is a fuzzy logic that is used for the produced output in accordance with the input. The three main components produce logic, which is then used for motor movement control in the actuator. The input used in fuzzy logic is an error value. Therefore, before designing the input part of the Fuzzy Logic Designer, it was necessary to determine the boundary of the error value that is used as the so-called the input membership function in this study. It is identified and summarized in Table 1.

Table 1. Membership function input command identification

Error	Error Identification	Symbol
6 cm – 4 cm	Positive Large	PL
4 cm – 2 cm	Positive Normal	PN
2 cm – 0 cm	Positive Small	PS
0	Zero	Zero
0 cm – (-2 cm)	Negative Small	NS
(-2 cm) – (-4 cm)	Negative Normal	NN
(-4 cm) – (-6 cm)	Negative Large	NL

Source: Authors

The rotational speed of the DC motor is controlled using PWM. When the value of PWM is positive, the motor pulls the tendon to move in flexion. However, while the value is negative, the motor stretches the tendon, or the soft glove position returns to its normal position. The output membership function response is identified in Table 2. After the membership functions of the input and the output are determined, the next step is to design a rule or logic. The employed logic is "if" and "then", which means that if the input X has been determined, then the output Y will be produced. The rule used in motor control in this study can be seen in Table 3. The embedded control block of the wearable soft robotic glove with FLC is shown in Figure 5. The FCL is developed with a Simulink block diagram, as shown in Figure 6. The reading of a potentiometer or electromyography (EMG) sensor is applied using analog input block with a sampling frequency of 50 Hz.
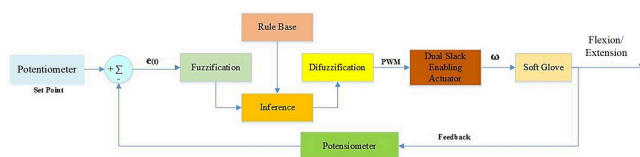
Figure 5. Fuzzy Logic control employed in the soft exoskeleton glove.
Source: Authors
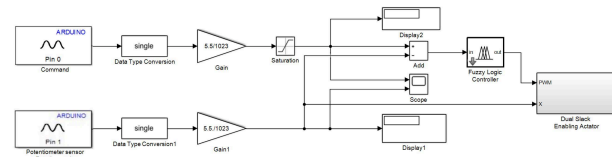
Figure 6. Block diagram of embedded Fuzzy Logic control in MATLAB/Simulink.
Source: Authors

Table 2. Membership function output response identification

PWM	PWM Identification	Symbol
0 – 6 cm	Positive PWM	P_PWM
0 cm	Zero	Zero_PWM
(-6 cm) – 0 cm	Negative PWM	N_PWM

Source: Authors

Table 3. Fuzzy logic rule

Logic	Error	Logic	PWM
	PL		P_PWM
	PN		P_PWM
	PS		P_PWM
If	Zero	Then	Zero_PWM
	NS		N_PWM
	NN		N_PWM
	NL		N_PWM

Source: Authors

Results and Discussion

In this section, the results of testing the soft exoskeleton glove control performance will be implemented on healthy human hands. Performance control testing is performed by comparing the results of the test, given the command and the resulting response. The control performance test is conducted by comparing the results between with and without load. The 'without load' category implies that the soft exoskeleton glove is not worn by a user, while a 'with load test' means that the soft exoskeleton glove is worn on a healthy human hand.

Fuzzy Inference System (FIS) is one of the algorithms used for decision making. In fuzzy logic designs, there are three main parts, namely input commands, rules, and commands or fuzzy logic, which are designed based on the input, and consequently respond as the produced output. The FIS for this study is shown in Figure 7.

Before the fuzzy logic performance test is carried out, it is necessary to fine-tune the membership input and output functions in the fuzzy logic designer to get a control response that matches the objectives. In this study, the tuning was performed six times to identify the best response from several conducted experiments. Table 4 shows the PWM value entered in the membership function.
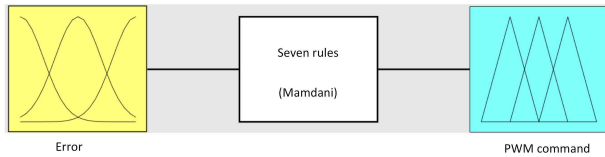
Figure 7. Fuzzy Inference System diagram.
Source: Authors

Table 4. Value of membership function for PWM command

No	Trial	Parameters		
		Negative PWM	Zero	Positive PWM
1	Tuning 1	[-150 -60]	[-80 0 80]	[60 150]
2	Tuning 2	[-130 -20]	[-70 0 70]	[20 130]
3	**Tuning 3**	**[-180 -20]**	**[-90 0 90]**	**[20 180]**
4	Tuning 4	[-220 -20]	[-120 0 120]	[20 220]
5	Tuning 5	[-200 20]	[-110 0 110]	[20 200]
6	Tuning 6	[-150 -20]	[-100 0 100]	[20 150]

Source: Authors

From several experiments in tuning that input into the membership function plot, the best response was obtained in the third trial. The best plot obtained from the input membership function is shown in Figure 8.
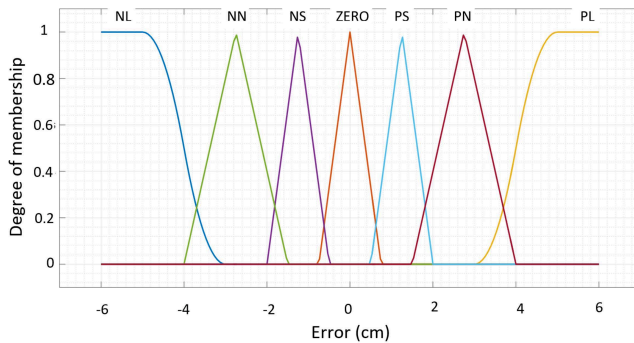
Figure 8. Input membership function.
Source: Authors

Membership Function Output is the PWM limit value entered in the output dialog box. The values entered are for a negative PWM from -180 to -20, as well as a positive PWM from 20 to 180. For typical values, as well as those in the plot, which are depicted with zero-lines, the entered value is -90 to 90. The best plot obtained by the membership function output as a response representing the value of the PWM output is shown in Figure 9.

The output membership function that occurs in accordance with the PWM value is shown in Figure 9. If the PWM value is positive, the motor pulls the tendon, which is represented by the orange line (positive PWM). When the PWM motor is negative (negative PWM), the motor stretches the tendon, or the soft glove position returns to normal, which is represented by the blue line.
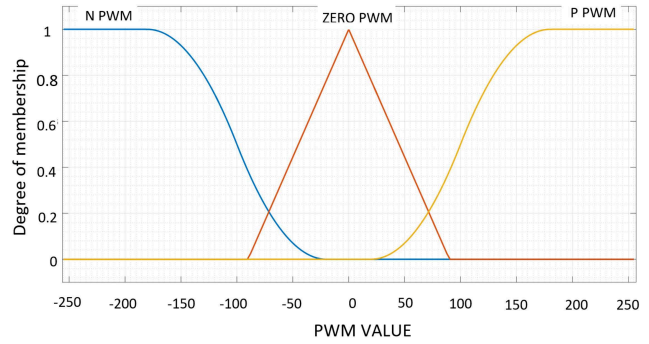
Figure 9. Output membership function.
Source: Authors

The Simulink block diagram is built and then embedded in the Arduino Mega 2560 microcontroller for data retrieval. The data is taken in the form of steps and a trajectory following input and output in terms of time. Tests are carried out with and without load so that the data is obtained, which is then carried out data plots. Figure 10 shows the step signal input and output plots with respect to time.
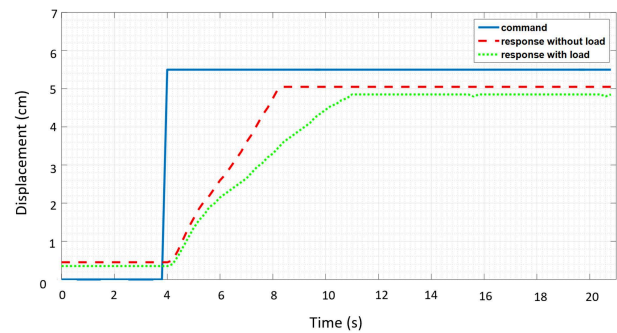
Figure 10. Fuzzy logic control response with the input step command.
Source: Authors

Figure 10 reveals the command signal represented by a blue line. The red-dashed lines represent the without-load response signal, while the green dot line represents the response signal with a load. The performance of the transient response system based on the test is shown in Table 5. "Without-load" means that the soft exoskeleton glove was unattached on the human hand, whereas "with a load" means that the soft glove was attached to the human hand.

Table 5. System transient response performance

No	Performance	Symbol	Value		Unit
			Without load	With load	
1	Time constant	τ	1,9	2,8	s
2	Rise time	Tr	0,3	0,2	s
3	Settling time	Ts	1,1	1,6	s
4	Delay time	Td	0,2	0,3	s
5	Steady-state error	SSE	8,2	11,8	%

Source: Authors

The trajectory following command is used for the input and output signals to determine the suitability of the response to the given command. The results of the trajectory graph of the given signal command and the response ares shown in Figure 11. Based on these results, there is a delay of about 1 second.
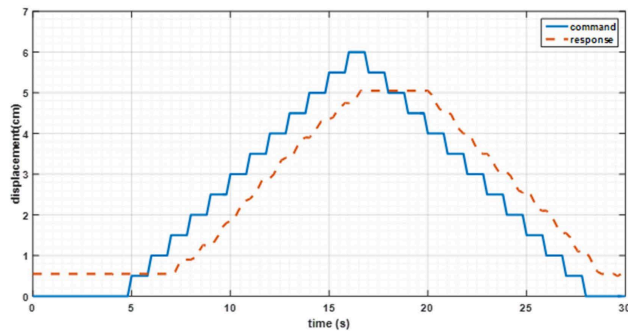
Figure 11. Trajectory following command and response signals.
Source: Authors

Object Grasping Test

In this section, the results of the test with and without load will be discussed. The no-load test was carried out by pulling the sheath tendon every 1 cm to observe the curvature that was formed in the soft exoskeleton glove. Figure 12 shows the test results of the movement by pulling the sheath tendon. Based on the test results, there is a change in the angle of 67° on the first segment of the finger by pulling the sheath tendon from 0 to 5 cm.
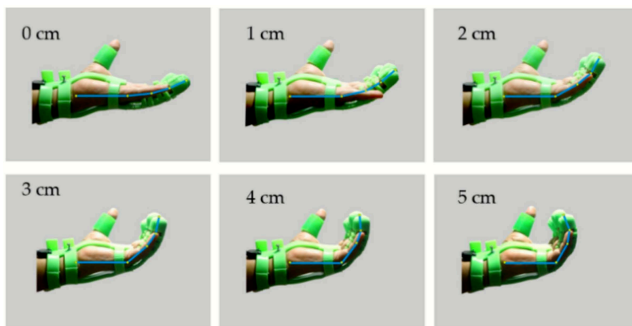
Figure 12. The trajectory of the finger when the soft exoskeleton glove is worn by the user.
Source: Authors

In the next test, the soft exoskeleton glove is used to assist and provide mechanical support to the user's hand. In this test, the glove is attached to healthy human hands. The test results are shown in Figure 13. Based on these results, the soft exoskeleton glove can assist and provide mechanical support in grasping six various objects of different sizes, shapes, and masses.

Based on the previous study using PI compensator for controlling the exoskeleton glove (Setiawan, *et al.*, 2020), FLC
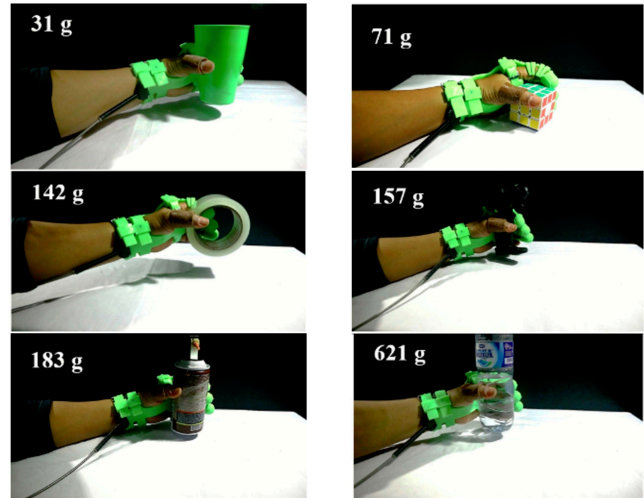
Figure 13. Grasping test with various objects.
Source: Authors

has a better performance and faster response compared to PI compensators. The video performance of the developed soft exoskeleton glove for providing mechanical assistances worn by a user can be seen online at https://www.youtube.com/watch?-v=497cCqo5V5M&t=13s

Conclusions

In this study, a soft exoskeleton glove prototype with the motor-tendon actuator was successfully developed. It consists of three main components in the working system: soft glove, tendon sheath, and motor-tendon actuator. The fuzzy logic control design for controlling the motion of the soft exoskeleton glove has been successfully developed and implemented. The best-obtained values for negative PWM are from -180 to -20, and the positive PWM values range between 20 and 180. The soft exoskeleton glove was able to pull the first segment of fingers of the user up to 67° which produced the curvature that was necessary for grasping. The soft exoskeleton glove can assist the user in grasping various types of objects with variations in shape, size, and mass.

Acknowledgments

References

Balciunas, A., Murphy, P., and Zdonbinski, Z. (2019). Viability and function of myoelectric prosthetics as compared to passive, body-powered, and electrically powered prosthetics. First-Year Conference Paper, University of Pittsburgh, Swanson School of Engineering, 3 August 2019.

Birnbaumm, I. (2016). *The 'Maserati of Microprocessor Prosthetics' Costs $120,000.* https://www.vice.com/en_us/article/jpgagx/luxury-prosthetics

Geethanjali, P. (2016). Myoelectric control of prosthetic hands: state-of-the-art review. *Medical Device (Auckland)*, 9, 247-255. 10.2147/MDER.S91102

Gearhart, C. J., Varone, B., Stella, M. H., and BuSha, B. F. (2016). An effective 3-fingered augmenting exoskeleton for the human hand. In IEEE (Eds.) *38th Annual International Conference of the IEEE Engineering in Medicine and Biology Society (EMBC)* (pp. 590-593). New York, NY: IEEE. 10.1109/EMBC.2016.7590771

Hadi, A., Alipour, K., Kazeminasab, S., and Elahinia, M. (2018). ASR glove: A wearable glove for hand assistance and rehabilitation using shape memory alloys. *Journal of Intelligent Material Systems and Structures*, 29(8),1575-1585. 10.1177/1045389X17742729

Hill., S., and Krug, E. (2017). *Standards for Prosthetics and Orthotics. World Health Organization.* https://apps.who.int/iris/-bitstream/handle/10665/259209/97892415124 80-part1-eng.pdf

Ho, N. S., Ton, K. Y., Hu, X. L., Fung, K/L., Wei, X. J., Rong, W., and Susanto, E. A. (2011). An EMG-driven exoskeleton hand robotic training device on chronic stroke subjects: Task training system for stroke rehabilitation. In IEEE (Eds.) *IEEE International Conference on Rehabilitation Robotics* (pp. 1-5). New York, NY: IEEE. 10.1109/ICORR.2011.5975340

In, H., Kang, B. B., Sin, M. K., and Cho, K. J. (2015). Exo-Glove: A wearable robot for the hand with a soft tendon routing system. *IEEE Robotics & Automation Magazine*, 22(1), 97-105. 10.1109/MRA.2014.2362863

Ismail, R., Ariyanto, M., Pambudi, K. A., Syafei, J. W., and Ananto, G. P. (2017). Extra robotic thumb and exoskeleton robotic fingers for patient with hand function disability. In IEEE (Eds.) *4th International Conference in Electrical Engineering, Computer Science and Informatics (EECSI)* (pp. 1-6). New York, NY: IEEE. 10.1109/EECSI.2017.8239166

Kamikawa Y., and Maeno T. (2008). Underactuated five-finger prosthetic hand inspired by grasping force distribution of humans. In IEEE (Eds.) *IEEE/RSJ International Conference on Intelligent Robots and Systems* (pp. 22-26). New York, NY: IEEE. 10.1109/IROS.2008.4650628

Kim, B., In, H., Lee, D. Y., and Cho, K. J. (2017). Development and assessment of a hand assist device: GRIPIT. *Journal of Neuro Engineering and Rehabilitation*, 14(1), 15. 10.1186/s12984-017-0223-4

Ku, I., Lee, G. K., Park, C. H., Lee, J., and Jeong, E. (2019). Clinical outcomes of a low-cost single-channel myoelectric-interface three-dimensional hand prosthesis. *Archieves of Plastic Surgery*, 46(4), 303-310. 10.5999/aps.2018.01375

Marks, L. J., and Michael, J. W., (2001). Clinical Review. *BMJ*, 232(September), 732-735. 10.1136/bmj.323.7315.732

Polygerinos, P., Lyne, S., Wang, Z., Fernando, L., Mosadegh, B., Whitesides, G. M., and Walsh, C. J. (2013). *Towards a soft pneumatic glove for hand rehabilitation.* Paper presented at the 26th IEEE/RSJ International Conference on Intelligent Robots and Systems: New Horizon, IROS 2013- Tokyo, Japan. 10.1109/IROS.2013.6696549

Pu, S. W., Chang, J. Y., Pei, Y. C., Kuo, C. C., and Wang, M. J., (2016). Anthropometry-based structural design of a hand exoskeleton for rehabilitation. In IEEE (Eds.) *23rd International Conference on Mechatronics and Machine Vision in Practice (M2VIP)* (pp. 1-6). New York, NY: IEEE. 10.1109/M2VIP.2016.7827282

Randazzo, L., Iturrate, I., Perdikis, S., and Millán, J. d.R (2018). Mano: A wearable hand exoskeleton for activities of daily living and neurorehabilitation. *IEEE Robotics and Automation Letters*, 3(1), 500-507. 10.1109/LRA.2017.2771329

Ribeiro, J., Mota, F., Cavalcante, T., Nogueira, I., Gondim, V., Albuquerque, V., and Alexandria, A. (2019). Analysis of man-machine interfaces in upper-limb prosthesis: A review. *Robotics, 8*, 16, 1-17. 10.3390/robotics8010016

Setiawan, J. D., Ariyanto, M., Nugroho Sri., Munadi M., and Ismail R. (2020). A soft exoskeleton glove incorporating motor-tendon actuator for hand movements assistance. *International Review of Automatic Control*, 13(1), 1-11. 10.15866/ireaco.v13i1.18274

Slade, P., Akhtar, A., Nguyen, M., and Bretl, T. (2015). Tact: Design and performance of an open-source, affordable, myoelectric prosthetic hand. In IEEE (Eds.) *IEEE International Conference on Robotics and Automation (ICRA)* (pp. 6451-6456). New York, NY: IEEE. 10.1109/ICRA.2015.7140105

Sreenivasan, N., Gutiérrez, D. F. U., Bifulco, P., Cesarelli, M., Gunawardana, U., and Gargiulo, G. D. (2018). Towards ultra low-cost myoactivated prostheses. *BioMed Research International*, 2018, 9634184. 10.1155/2018/9634184

Villoslada, A., Flores, A., Copaci, D., Blanco, D., and Moreno, L., (2015). High-displacement flexible shape memory alloy actuator for soft wearable robots. *Robotics and Autonomous Systems*, 73, 91-101. 10.1016/j.robot.2014.09.026

Wang, B., McDaid, A., Aw, K. C., and Biglari-Abhari, M. (2017). Design and development of a skinny bidirectional soft glove for post-stroke hand rehabilitation. Paper presented at the *Intelligent Systems Conference (IntelliSys)*. 10.1109/IntelliSys.2017.8324248

Yap, H. K., Goh, J. C. H., and Yeow, R. C. H. (2015). Design and characterization of soft actuator for hand rehabilitation application. In Lacković, I., and Vasic, D., (Eds.) *6th European Conference of the International Federation for Medical and Biological Engineering* (vol. 45, pp. 367-370). Cham: Springer International Publishing. 10.1007/978-3-319-11128-5_92

Yap, H. K., Ang, B. W. K., Lim, J. H., Goh, J. C. H., and Yeow, C. H. (2016). A fabric-regulated soft robotic glove with user intent detection using EMG and RFID for hand assistive application. In IEEE (Eds.) *IEEE International Conference on Robotic and Automation (ICRA)* (pp. 3537-3542). New York, NY: IEEE. 10.1109/ICRA.2016.7487535

Yoshikawa, M., Sato, R., Higashihara, T., Ogasawara, T., and Kawashima, N. (2015). Rehand: Realistic electric prosthetic hand created with a 3D printer. In IEEE (Eds.) *37th Annual International Conference of the IEEE Engineering in Medicine and Biology Society* (*EMBC*) (pp. 2470-2473). New York, NY: IEEE. 10.1109/EMBC.2015.7318894

Yun, S. S., Kang, B. B., and Cho, K. J. (2017). Exo-Glove PM: An easily customizable modularized pneumatic assistive glove. *IEEE Robotics and Automation Letters*, *2*(3), 1725-1732. 10.1109/LRA.2017.2678545

Tensile Properties of 3D printed polymeric pieces: comparison of several testing setups

Propiedades de tracción de piezas poliméricas hechas en impresión 3D: comparación de diversas configuraciones de prueba

Andrés Romero[1], Marcelo Piovan[2], Carlos Mainetti[3], Dario Stechina[4], Sandra Mendoza[5], Hector Martín[6], and Claudio Maggi[7]

ABSTRACT

This work aims to evaluate and compare variations of a methodology for performing tensile tests on thermoplastic specimens constructed by additive manufacturing technologies (AMT) with filament deposition modeling (FDM). The testing procedures of pieces made in FDM machines do not yet have any conclusive standards because 3D printing, as a disruptive and exponentially growing technology, has not allowed enough time to reach a definitive scientific consensus. Nowadays, testing standards for injected thermoplastic parts or laminated composites are employed as substitutes with careful implementation. A comparative study was carried out on the elasticity modulus, determined within the framework of the same standard but with different measuring devices and testing machines. These machines cover a broad range from professional automated high precision machines to lab and specialized machines. Sets of 3D-printed specimens with identical manufacturing parameters were constructed in a commercial 3D printer. An analysis of variance was performed in order to evaluate the consistency and significance of experimental data for the same polymer, considering the machine type and its corresponding setup. From the experimental data, it is concluded that, with the due care, all evaluated testing setups can reach comparable results, especially in the absence of sophisticated and expensive measuring systems.

Keywords: 3D printing, elastic properties, tensile tests, testing sensitivity

RESUMEN

El objetivo de este trabajo es evaluar y comparar variantes en una metodología para realizar ensayos de tracción en probetas termoplásticas hechas con tecnologías de construcción aditiva (AMT) con modelado por deposición de filamento (FDM). Los procedimientos de ensayo para piezas hechas en máquinas FDM aún no tienen estándares conclusivos, pues la impresión 3D, al ser una tecnología disruptiva que crece exponencialmente, no ha dado tiempo suficiente para establecer un consenso científico definitivo. Actualmente, los estándares de prueba para partes con inyección termoplástica se emplean como sustitutos con una implementación cuidadosa. Se efectuó un estudio comparativo del módulo de elasticidad, determinado en el marco del mismo estándar pero con dispositivos de medición y máquinas de prueba diferentes. Estas máquinas cubren un rango que va desde máquinas de ensayo profesionales de alta precisión hasta máquinas de laboratorio construidas *ad-hoc*. Se construyeron conjuntos de probetas bajo los mismos parámetros de manufactura en una impresora 3D comercial. Se hizo un análisis de varianza con el fin de evaluar la consistencia y significancia de los datos experimentales para el mismo polímero, teniendo en cuenta el tipo de máquina y su correspondiente configuración. A partir de los datos experimentales, se concluye que, con el debido cuidado, todas las configuraciones de ensayo analizadas pueden alcanzar resultados comparables, especialmente en ausencia de sistemas de medición sofisticados y costosos.

Palabras clave: impresión 3D, propiedades elásticas, ensayos de tracción, sensibilidad de ensayos

[1] Electr. Engineer, Universidad Tecnológica Nacional, FR Bahía Blanca (UTN-FRBB), Argentina. Affiliation: Assistant Professor, Centro de Investigaciones en Mecánica Teórica y Aplicada (CIMTA-UTN-FRBB), Argentina.
E-mail: andresrom147@hotmail.com
[2] Ph.D., Universidad Nacional del Sur (UNS), Argentina. Affiliation: Full Professor, CIMTA-UTN-FRBB. E-mail: mpiovan@frbb.utn.edu.ar
[3] Electr. Engineer, UTN-FRBB. Affiliation: Associate Professor, Dept. Electr. Eng. UTN-FRBB, Argentina. E-mail: mainetti@frbb.utn.edu.ar
[4] Mech. Engineer, Universidad Tecnológica Nacional, FR Reconquista (UTN-FRRQ), Argentina. Affiliation: Research student, UTN FRRQ Grupo de Diseño Industrial (GRUDIN). E-mail: dario.stechina@gmail.com
[5] Ph.D., Utrecht University, Netherlands. Affiliation: Associate Professor, UTN-FRRQ. E-mail: smendoza@frrq.utn.edu.ar
[6] Ph.D., UNS, Argentina. Affiliation: Associate Professor, GRUDIN UTN-FRRQ, Argentina. E-mail: hectordmartin@gmail.com
[7] Mech. Engineer, UTN-FRRQ. Affiliation: Assistant Professor, GRUDIN UTN-FRRQ, Argentina. E-mail: ncmaggi@arnet.com.ar

Introduction

Additive manufacturing technologies (AMT) or 3D printing are not particularly new, since the basic prototypes emerged in academic laboratories during the 1970's. Embryonic ideas have rapidly evolved, leading to the construction of professional machines during the 1980s (Canesa, Fonda, Zennaro, 2013; Dizon, Espera, Chen, and Advincula, 2018).

However, such machines were limited, and their product was expensive and only useful as a visualization tool without a productive purpose.

The evolution of AMT led to a broad variety of procedures, where inks, resins, plastic polymers, and powdered ceramics/metals have been employed as construction materials. In the beginning, the polymeric Filament Deposition Modeling (FDM) was the leading procedure in AMT. Nowadays, among all the existing procedures on the market, FDM is yet the most employed procedure, covering more than 51% of the additive manufacturing applications worldwide (Dizon *et al.*, 2018). This is due to the following reasons: the fall of international patents of several technologies, procedures and machines, and the emergence of the REPRAP project in Bath University, as well as very friendly and economical micro-controllers (*e.g.* Arduino, Sanguino, etc.). All these factors, among others, led to an unsuspected revolution in the construction of 3D printers all around the world, which is today in full expansion and without a prognosis for roof limits, at least for the next 10 years (Wohlers, 2017). Until the appearance of the REPRAP printers, there was scarce interest in determining elastic properties, as well as mechanical and constitutive models, for pieces constructed with AMT. This is due to the fact that products constructed with such machines served as prototype models for preliminary evaluation, as a previous step for constructing the final product through conventional machining procedures. Consequently, knowledge about strength and durability was not taken in to account. However, considering the improvement of production processes, the quality of the materials and the need to replace real parts or to build functional parts for service in real operating conditions, the determination of mechanical properties of parts constructed with AMT under prescribed resistance or strength has become a commandment (Tymrak, Kreiger, and Pearce, 2014). In this context, since the settlement and immediate evolution of the REPRAP project, numerous articles have appeared, covering a wide range of studies on mechanical properties of printed parts. In a basic survey of scientific/technical papers which experimentally analyze or model the material properties of printed specimens, it is possible to find no less than 500 articles in indexed journals (SCOPUS, SCIMAGO, etc.), nearly 80% of them belonging to the last five years (Chacon, Caminero, Garcia-Plaza, and Núñez, 2018; Torrado and Roberson, 2016; Caminero, Chacón, García-Moreno, and Rodríguez, 2018; Balderrama *et al.*, 2018; Valerga, Batista, Salguero, and Girot, 2018). In all the aforementioned studies, the main purpose was to evaluate the influence of diverse constructive and operative parameters (such as temperatures, infill, stain, layer thickness, etc.) in the mechanical response of a given polymer employed for 3D printing. However, a lot of dispersion in the adopted criteria was observed, due to the absence of specific standards for testing printed pieces (Foster, 2015) and the difficulty to reach a consensus regarding the behavior of micro/macro mechanics of 3D printed pieces. Apart from the constructive parameters of AMT, there is a topic that is not commonly taken into account, which plays an important role. This is the case of the criteria and machines employed within the testing procedures according to the equipment available in the institutions that perform the studies. Some authors employed professional automatic testing equipment, including extensometers (Tymrak *et al.*, 2014; Caminero *et al.*, 2018; Chacon *et al.*, 2017), but others used professional machines without them (Lanzotti, Grasso, Staiano, and Martorelli, 2015). Some authors employed academic machines with manual handling without an indication of uniformity in the strain rate (Ahmed, Islam, Vanhoose, and Rahman, 2017), while others developed their own testing criteria or machines, and so on (check Dizon *et al.*, 2018 for a long set of references). A comparison of the material properties obtained in the papers above for the same type of materials reveals an important dispersion. This leads to the uncomfortable idea of doubting which data to use for prescribing the properties and subsequent response of a printed part.

This article is aimed to complement the previous studies. It presents a compatibility analysis, connected with positioning/locking and testing/measuring singularities of the specimen in given machines, considering accepted variations of applicability of the testing setup (*e.g.* use of extensometer or not, among others). The elasticity moduli are calculated with data extracted from three testing machines with different features, namely a fully automated professional machine, an academic laboratory test machine (with hand operation) and an *ad hoc* testing machine built by the first three authors (with automated operation). Tensile tests were circumscribed within the framework of a given standard for injected plastics (ISO 527/1, 1996; ISO 527/2, 1996), which has been used by many other authors (Lechter, and Waytaschek, 2014; Torrado and Roberson, 2016) as the operative and conceptual framework for their studies.

The present work is structured as follows: first, the methodology of the test, materials and probes are described, as well as the main features, differences and similarities of the employed machines. Then, some results are presented and a comparison through the analysis of variance of the processed results is carried out. Finally, conclusions, limitations and future research are outlined.

Methodology and materials

Figure 1 shows three types of machines employed for the comparative tests. Figure 1(a) shows the high precision professional machine; Figure 1(b), the academic homologated machine (employed by many authors worldwide (Ahmed, Islam, Vanhosse and Rahman, 2017); and Figure 1(c), the *ad-hoc* machine built in the laboratories of the Center for Research in Theoretical and Applied Mechanics of UTN FRBB. For these machines, the procedure described in the ISO 527/2 Standards was proposed (1996). Figure 2 shows the dimensions and characteristic lengths of the ISO 527/2-5A specimen: L_G is the gauge-length (where the strain is measured and extensometer placed, if employed) and L_{gh} is the initial length between grip-heads. The testing machines have differences and similarities between them. Table 1 shows the main features of each one. As it can be seen, INSTROM 33961 has a better quality in comparison to the other two machines.

(a)

(b)

(c)

Figure 1. Machines employed: (a) INSTRON 33691, (b) PASCO ME-8230, (c) CIMTA-MEP02.
Source: Authors

Table 1. Details of the testing machines

Machine	INSTROM33961	PASCO ME8230	CIMTA-MEP02
Laboratory	PLAPIQUI	UTN-FRRQ	UTN-FRBB
Load control	Automatic	Manual crank	Automatic
Software control	Instrom®	Capstone®	Matlab® based
Strain recording	Difference between grips		
Displ. precision	0,0001 mm	0,001 mm	0,005 mm
Load precision	0,0001 N	0,001 N	0,001 N
Grips fixing and locking	Pneumatic Toothed clamp	Geometric Clamp	Mechanical Toothed clamp

Source: Authors

Figure 3 shows sketches of the specimen mounted on the grip-heads. The INSTROM 33961 and CIMTA-MEP02 machines have the same mounting scheme. On the other hand, PASCO ME8230 has grips to hold the bone-shaped end of the specimen. This choice was not awkward, taking into account that the measurement of displacements and strains in all of

these machines is based on the difference of distance between grips, an aspect accepted in absence of extensometers, and employed in much of the aforementioned research. Thus, the specimen mounted on the PASCO machine has $L_G \approx L_{gh}$.
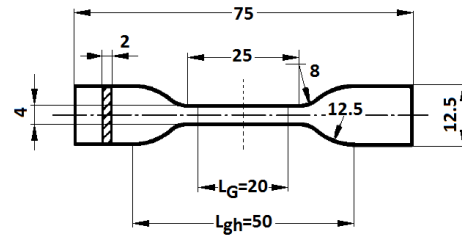
Figure 2. Dimensions (mm) of the ISO 527/2-5A specimen.
Source: Authors

(a)

(b)
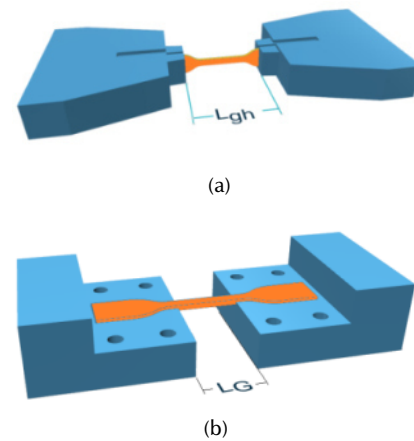
Figure 3. Sketches of locking devices: (a) INSTRON 33691and CIMTA-MEP02, (b) PASCO ME8230.
Source: Authors

In order to help the understanding of this topic, a 3D finite element analysis, performed in FlexPDE® (Backstrom, 2006), is shown in Figure 4, where, it is possible to see the variation of the longitudinal displacement in the axis line of an ISO 527/2-5A specimen under a given extensional tension, according to the typical mounting (in absence of an extensometer) of INSTROM 33691 and CIMTA-MEP02 machines.

As expected, a linear displacement pattern (*i.e.* constant strain) along the gauge length L_G (path B) is observed. However, in order to avoid mistakes in the calculation of elastic properties, the non-linear displacement (paths A and C) must be considered to correlate the effective strain and displacement of the specimen versus the final distance measured between grips or grip-heads as well. This correction is automatically performed by the control software of the INSTROM 33691 machine, by setting up the type of specimen and gauge-length (this procedure si carried out in absence of an extensometer), whatever the distance between head-jaws. On the other hand, in the CIMTA-MEP-02 machine, the correction factor must be calculated (for definite L_{gh}) in Matlab routines employing the raw experimental data. This conception implies that parts (A), (B) and (C) must be printed with the same features.
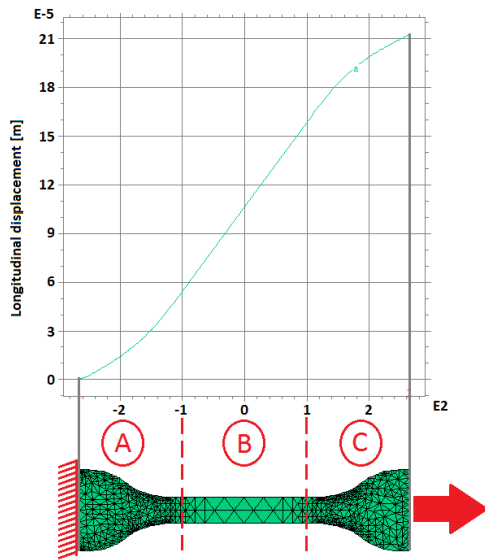
Figure 4. Simulation of the displacement in ISO 527/2-5A specimens.
Source: Authors

In accordance with ISO 527-2 (1996) regarding the determination of the modulus of elasticity and extensional stress, the following expressions are used:

$$E_m = \frac{\sigma_1 - \sigma_2}{\epsilon_1 - \epsilon_2}, \qquad (1)$$

$$\sigma = \frac{F}{A} \qquad (2)$$

where σ is tensile stress; F and A are the measured tensile force and the initial cross-sectional area of the specimen, respectively E_m is the elasticity modulus; and σ_i and ϵ_i ($i = 1, 2,$) are tensile tension and strain at the i-th point of the proportionality line of the test. Particularly, σ_i ($i = 1, 2$) should be the stress values associated to strains $\epsilon_2 = 0,0050$ and $\epsilon_1 = 0,0025$, respectively.

Such strains correspond to values homogenized from the raw experimental data to a common origin within the whole set of specimens (a procedure requested in the standards). This is done to avoid eventual spurious effects at the beginning of the test, such as slippage or other irregularities when the grip may be not firm enough.

Four types of polymers used in 3D printing (other than the commonly tested ABS and PLA) are evaluated: high-impact poly-styrene (HIPS), recycled polyethylene terephthalate (PET), poly-lactic acid with carbon conductive powder (CPLA), and poly-lactic acid with thermo-chromatic additives (TPLA). A standard operating speed of 5 mm/min (Tymrak et al., 2014; Torrado and Roberson, 2016) has been set for all machines. In the case of the academic PASCO machine, some preliminary tests have necessarily been carried out in order to fix the proper rotation speed of the crank, although it has a variability which is intended to be evaluated against the uniform processes.

The printing parameters of each set of specimens are shown in Table 2. They correspond to the optimal configurations given or suggested by printer and filament manufacturers, given that they correspond to a machine of Argentinian origin: Far-TecnoART®, which has a nozzle diameter of 0,35 mm and uses 1,75 mm filaments. All of the latter were acquired from the same manufacturer. The whole set of 16 specimens for each material was constructed simultaneously in a multiple part printing process (Figure 5). The CURA V15.04 software was used for slicing and creating the gcode.

Table 2. Printing parameters

Material	HIPS	PET	CPLA	TPLA
Print speed [mm/s]	25	25	30	30
Nozzle temperature [°C]	240	245	225	215
Bed temperature [°C]	80	35	60	60
Thickness of layers [mm]	0,2	0,2	0,2	0,2
Infill [%]	100	100	100	100
Raster angle [°] respect L_G	0	0	0	0
Number of outer loops	2	2	2	2
Printed number of specimens	16	16	16	16

Source: Authors
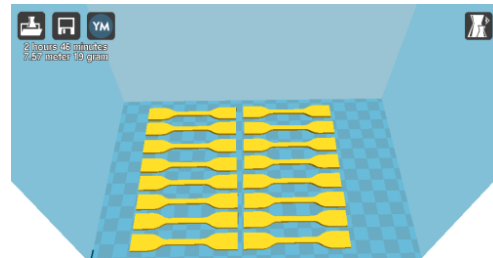
Figure 5. Distribution of the samples in the printer platform.
Source: Authors

Sets of four specimens of each material were selected for testing on each machine. A few of them were spared in case of unexpected failure or inconsistent results. All sets were randomly chosen from the printing platform.

Results and analysis

Figure 6 shows the displacement of the machine-head with respect to the time of a typical test performed in the three employed systems.

As it is possible to see, the paths of INSTROM 33691 and CIMTA-MEP02 are lines (i.e. motion of uniform speed set in 5 mm/min = 0,0833 mm/s), whereas a variable behavior is observed in the case of PASCO ME8230, which oscillates along the aforementioned linear path. This behavior is consistent with the manual handling of the machine, and special attention was given to the rotation pace of the crank in order to maintain the speed of the machine head as close as 5 mm/min (this was controlled by means of the Capstone software that interfaces the PC and test machine).
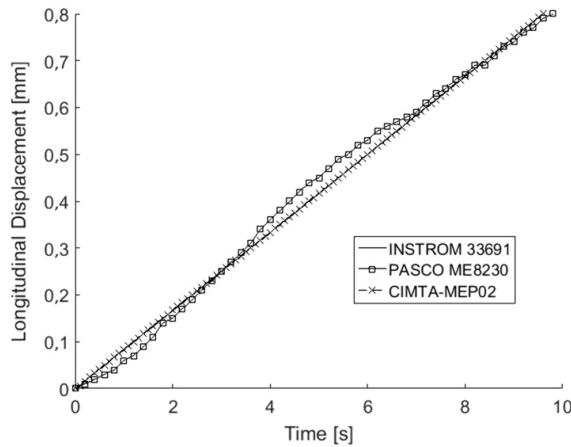
Figure 6. Example of machine-head motion.
Source: Authors

Figure 7 shows the maximum and minimum stress-strain experimental envelope curves of the CPLA tested with the three machines. The present results are compared with the experimental data gathered from the research by Jain and Tadesse (2019), who evaluated the response of their version of carbon conductive PLA (or CPLA) with respect to the percentage of conductive carbon incorporated to plain PLA. As mentioned before, the CPLA employed in the present research is generic (and not completely detailed by its manufacturer). It is possible to see that the present results are contained between the limit cases of the experimental data offered by Jain and Tadesse (2019).
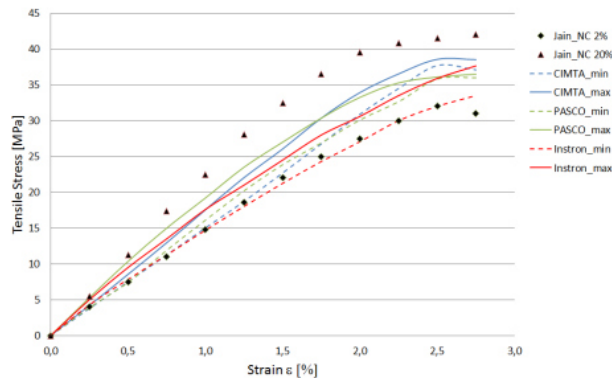
Figure 7. Stress-strain curves of tests in CPLA compared with data of the literatures (Jain and Tadesse 2019).
Source: Authors

In Tables 3 to 6, it is possible to see the elasticity modulus resulting from the tests for HIPS, PET, CPLA and TPLA, respectively. In these Tables, only the mean and coefficient of variation (CoV) of each set of samples are presented. The CoV is defined as the ratio of the standard deviation with respect to the mean. A simple survey of these results reveals that the INSTROM 33961 had the lower dispersion (or lower CoV) in the set of samples of every material. This was suspected *a priori*, considering that the machine INSTROM 33961 has

better quality and superior technology. Nevertheless, the dispersion observed in the samples of the other two machines had a CoV of comparable values in comparison with the ones observed in the INSTROM 33961. The CoV was generally lower than of 5% (an acceptable value for testing materials), except in the case of PET, which, by the way, as a recycled material, can suffer from moderate variability. Moreover, a quick overview of the experimental means of every material reveals an apparently low discrepancy among all machines and their corresponding testing criteria, except in the cases of PET and TPLA, where there was a difference of nearly 5% between two particular testing schemes. However, in order to compare the results of the three machines and their corresponding assemblies, an analysis of variance (ANOVA) had to be performed.

Table 3. Elasticity moduli (MPa) for HIPS specimens

Machines	CIMTA-MUEP-02	INSTROM33961	PASCO ME8230
Specimen 1	944,87	915,70	920,30
Specimen 2	972,36	964,42	982,39
Specimen 3	887,13	948,45	898,49
Specimen 4	902,80	895,02	929,03
Mean	926,79	930,90	932,55
CoV	0,042	0,034	0,038

Source: Authors

Table 4. Moduli of Elasticity (MPa) for PET specimens

Machines	CIMTA-MUEP-02	INSTROM33961	PASCO ME8230
Specimen 1	934,75	1 090,77	993,18
Specimen 2	1 061,39	989,46	953,87
Specimen 3	1 181,18	1 075,86	1 132,19
Specimen 4	1 107,53	998,71	1 010,53
Mean	1 071,21	1 038,70	1 022,44
CoV	0,097	0,050	0,075

Source: Authors

Table 5. Elasticity moduli (MPa) for CPLA specimens

Machines	CIMTA-MUEP-02	INSTROM33961	PASCO ME8230
Specimen 1	1 533,70	1 508,93	1 502,07
Specimen 2	1 581,67	1 593,19	1 530,23
Specimen 3	1 621,12	1 489,49	1 580,46
Specimen 4	1 495,56	1 566,12	1 612,32
Mean	1 558,02	1 539,43	1 556,27
CoV	0,035	0,031	0,032

Source: Authors

The ANOVA is a tool for statistical analysis, useful for comparing experimental results, taking into account the influence or significance of several factors or parameters that are imposed to given sets of specimens (for this article, the strain measuring criteria, clamping and motion control).

Table 6. Elasticity moduli (MPa) for TPLA specimens

Machines	CIMTA-MUEP-02	INSTROM33961	PASCO ME8230
Specimen 1	1 572,36	1 442,31	1 488,35
Specimen 2	1 480,13	1 495,87	1 431,74
Specimen 3	1 457,38	1 449,61	1 517,78
Specimen 4	1 500,13	1 467,28	1 468,12
Mean	1 502,50	1 463,77	1 476,50
CoV	0,033	0,016	0,024

Source: Authors

It is useful for identifying whether two or more sets of experimental data can be accepted to give the same results, provided the factors imposed to the set of specimens. In this study, the one-way ANOVA may be applied to the three sets of data. Then, the ANOVA, by employing the Fisher-Snedecor distribution (or F-distribution), checks the 'null-hypothesis' in which specimens of all groups are taken from populations with the same expected values. For a detailed use and understanding of the ANOVA, the reader is encouraged to consult the book by Cox and Reid (2000). The one-way ANOVA can be performed easily within the data-analysis of Excel®, Matlab®, or Mathematica® spreadsheets.

The null-hypothesis of this ANOVA test implies that, for every material and every subset (one for each machine), the subset behaves in the same manner, independent from the imposed factor. In other words, this implies that the mean values of the elasticity modulus for each independent factor (*i.e.* machines, clamping arrangement, etc.) are statistically the same, regardless of the presence of small differences between the samples.

Table 7. ANOVA statistics with a 0,05 level of significance

Material	f_{test}	$f_{critical}$	Probability: P_n
PET	0,383	4,256	0,6925
HIPS	0,028	4,256	0,9724
CPLA	0,162	4,256	0,8529
TPLA	1,057	4,256	0,3812

Source: Authors

Due to space limitations, the results of the ANOVA are condensed in Table 7, where it is observed that, in all cases, $F_{critical} = 4,256$ because each subset has 4 specimens, and the level of significance was set in 5% (which is typical for this type of analysis). Moreover $F_{critical} > F_{test}$, and $P_n > 5\%$ for all cases. This implies that there is no strong evidence to reject the null-hypothesis, that is, the expected values of the E-modulus, calculated with data of the machines, do not differ between them. All values of the parameter P_n are quite high, except for TPLA, which is borderline acceptable. However, there is no significant evidence that the results are due to random factors, thus satisfying the null-hypothesis.

Conclusions

This article has addressed a comparison of tensile material properties, specifically E-modulus, of typical polymers employed in 3D printing. This task has been carried out with three testing machines with different features, quality, and assembly, in accordance with standard ISO 527/2 (1996). From these tests, the following can be outlined:

a) Testing methodologies without the use of extensometers can be used to successfully determine the elasticity modulus of printed parts.

b) The differences between machine setups are not a strong factor to influence the sensibility in the calculation of the elasticity modulus in 3D printed specimens.

c) A slight variation in the deformation rate during individual tests (PASCO ME8230) has shown no significant influence in the determination of the E-modulus. However, the variation should be maintained as close as the value prescribed in the standard.

Since this article has shown the compatibility of results in employing different experimental layouts to determine the E-modulus of 3D printed specimens, there is still a wide variability and uncertainty in the behavior of printed pieces due to other sources, such as material quality and definiteness, material ageing, etc. The study of these topics is the matter of future research.

Acknowledgements

References

Álvarez, C. K., Lagos, C. R., and Aizpun, M. (2016). Investigating the influence of infill percentage on the mechanical properties of fused deposition modelled ABS parts. *Ingeniería e Investigación, 36*(3), 110-116. 10.15446/ing.investig.v36n3.56610

Ahmed, M., Islam, M., Vanhoose, J., and Rahman, M. (2017). Comparisons of Elasticity Moduli of Different Specimens Made Through Three Dimensional Printing. *3D Printing and Additive Manufacturing, 4*(2), 105-109. 10.1089/3dp.2016.0057

Backstrom, G. (2006). *Simple deformation and vibration by finite element analysis*. Malmö, Sweden: G&B Publishing.

Balderrama-Armendariz, C. O., MacDonald, E., Espalin, D., Cortes-Saenz, D., Wicker, R., and Maldonado-Macias, A. (2018). Torsion analysis of the anisotropic behavior of

FDM technology. *The International Journal of Advanced Manufacturing Technology 96,* 307-317.

Caminero, M. A., Chacón, J. M., García-Moreno, I., and Rodríguez, G. P. (2018). Impact damage resistance of 3D printed continuous fibre reinforced thermoplastic composites using fused deposition modelling. *Composites Part B: Engineering, 148,* 93-103. 10.1016/j.compositesb.2018.04.054

Chacon, J. M., Caminero, M. A., Garcia-Plaza, E., and Núñez, P. J. (2017). Additive manufacturing of PLA structures using fused depositing modelling: effect of process parameters on mechanical properties and their optimal selection. *Materials and Design, 124*(15), 143-157. 10.1016/j.matdes.2017.03.065

Canesa, E., Fonda, C., and Zennaro, M. (2013). *Low cost 3D-printing for Science, Education and Sustainable Development* (1st Ed). Trieste, Italy: The Adbus Salam International Center of Theoretical Physics.

Cox, D. R., and Reid, N. M. (2000). *The theory of design of experiments*. Boca Raton, FL: Chapman & Hall/CRC.

Dizon, J. R., Espera, A. H., Chen, Q., and Advíncula, R. C. (2018). Mechanical characterization of 3D-printed polymers. *Additive Manufacturing, 20,* 44-67. 10.1016/j.addma.2017.12.002

Far TecnoART (2018). *Far Innovation, Impresoras 3D.* https://www.far-arg.com/

Foster, A. M. (2015). *Materials Testing Standards for Additive Manufacturing of Polymer Materials: State of the Art and Standards Applicability* (*NISTIR 8059*). Washington DC: NIST, US Dept. of Commerce. 10.6028/NIST.IR.8059

Galantucci, L. M., Lavecchia, F., and Percoco, G. (2010). Quantitative analysis of a chemical treatment to reduce roughness of parts fabricated using fused deposition modeling. *CIRP Annals, 59*(1), 247-250. 10.1016/j.cirp.2010.03.074

ISO 527/1 (1996). Determination of tensile properties of plastics. Part 1: General principles. International Standards Organization.

ISO 527/2 (1996). Determination of tensile properties of plastics. Part 2: Test conditions for molding and extrusion plastics. International Standards Organization.

Jain, S. K. and Tadesse, Y. (2019). Fabrication of Polylactide/Carbon Nanopowder Filament using Melt Extrusion and Filament Characterization for 3D Printing. *International Journal of Nanoscience, 18*(5), 1850026. 10.1142/S0219581X18500266

Lanzotti, A., Grasso, M., Staiano, G., and Martorelli, M. (2015). The impact of process parameters on mechanical properties of parts fabricated in PLA with an open-source 3D printer. *Rapid Prototyping Journal, 21*(5), 604-617. 10.1108/RPJ-09-2014-0135

Lechter, T. and Waytaschek, M. (2014). Material property testing of 3D-pirnted specimen in PLA on an entry-level 3D printer. Proceedings of the ASME 2014 International Mechanical Engineering Congress and Exposition IMECE Nov 14-20, Montreal, Canada. IMECE2014-39379.

Torrado, A. R. and Roberson, D. A. (2016) Failure Analysis and Anisotropy Evaluation of 3D-Printed Tensile Test specimens of different Geometries and Print Raster Patterns. *Journal of Failure Analysis and Prevention, 16,* 154-164. 10.1007/s11668-016-0067-4

Tymrak, B. M., Kreiger M., and Pearce J. M. (2014). Mechanical properties of components fabricated with open-source 3-D printer s under realistic environmental conditions. *Materials and Design, 58,* 242-246. 10.1016/j.matdes.2014.02.038

Valerga, A. P., Batista, M., Salguero, J., and Girot, F. (2018). Influence of PLA filament conditions on characteristics of FDM parts. *Materials, 11*(8), 1322. 10.3390/ma11081322

Accelerated Adaptive Backstepping Control of the Chaotic MEMS Gyroscope by Using the Type-2 Sequential FNN

Control acelerado del backstepping adaptativo del giroscopio caótico MEMS por medio de la FNN secuencial de tipo 2

Le Zhao[1], Shaohua Luo[2], Guanci Yang[3], and Junyang Li[4]

ABSTRACT

In this paper, we propose an accelerated adaptive backstepping control algorithm based on the type-2 sequential fuzzy neural network (T2SFNN) for the micro-electromechanical system (MEMS) gyroscope with dead-zone and constraints. Firstly, the mathematical model of the MEMS gyroscope is established to perform dynamical analyses and controller design. Then, the phase diagrams and Lyapunov exponents are presented to reveal its chaotic oscillation, which is harmful to system stability. In order to suppress oscillations derived from chaos and dead-zone, an accelerated adaptive backstepping controller is proposed wherein an adaptive auxiliary is established to compensate the influence of nonsymmetric dead-zone on stability performance, along with the T2SFNN designed to approximate unknown functions of dynamic systems. Furthermore, the speed function is introduced to accelerate convergence speed of the control system, and the problem of complex term explosion in traditional backstepping is successfully solved by a second-order tracking differentiator. Finally, simulation results show that the proposed control scheme can guarantee asymptotic convergence of all signals in the closed-loop system, as well as satisfying states constraints and fulfilling the purposes of chaos suppression and accelerated convergence.

Keywords: MEMS gyroscope, type-2 sequential fuzzy neural network, accelerated backstepping control, chaotic oscillation, speed function

RESUMEN

En este artículo se propone un algoritmo de control acelerado y autoadaptado de backstepping basado en la red neural analgésica de tipo 2 (T2SFNN) para giroscopios del sistema microeléctrico (MEMS) con zona muerta y limitaciones. En primer lugar, se establece el modelo matemático del giroscopio MEMS para realizar análisis dinámicos y diseño de controladores. Luego, se presentan los diagramas de fase y los exponentes de Lyapunov para revelar su oscilación caótica, que es perjudicial para la estabilidad del sistema. Con el fin de suprimir las oscilaciones derivadas del caos y la zona muerta, se propone un controlador de backstepping adaptativo acelerado en el que se establece un auxiliar adaptativo para compensar la influencia de la zona muerta no simétrica en el rendimiento de estabilidad, junto con el T2SFNN diseñado para aproximar funciones desconocidas de sistema dinámico. Además, se introduce la función de velocidad para acelerar la velocidad de convergencia del sistema de control, y el problema de la explosión de términos complejos en el backstepping tradicional es resuelto exitosamente por un diferenciador de seguimiento de segundo orden. Finalmente, los resultados de la simulación muestran que el esquema de control propuesto puede garantizar la convergencia asintótica de todas las señales en el sistema de circuito cerrado, además de satisfacer las restricciones de los estados y lograr los propósitos de supresión del caos y convergencia acelerada.

Palabras clave: giroscopio MEMS, red neuronal difusa secuencial de tipo 2, control acelerado de backstepping, oscilación caótica, función de velocidad

Introduction

In view of the advantages of measuring the angular velocity of objects, low energy consumption, high integration, and simple structure, the MEMS gyroscope is widely used in vehicle navigation and positioning system, control, aerospace, the social robot, and other fields (Lin, Li, and Yang, 2020; Chong *et al.*, 2016; Fang, Fei, and Yang, 2018; Rahmani, 2018; Rahmani and Rahman, 2018; Su, Li, and Yang, 2020). Unfortunately, due to the influence of manufacturing errors and working environment changes, the measuring accuracy of the MEMS gyroscope will be greatly reduced. On top of that, the inherent characteristics of MEMS gyroscopes,

[1] School of Mechanical Engineering, Guizhou University, China. Affiliation: Student. Email: lezhao0813@126.com
[2] School of Mechanical Engineering, Key Laboratory of Advanced Manufacturing Technology, Guizhou University, China. Ph.D. Affiliation: Full professor. Email: shluo@gzu.edu.cn
[3] Key Laboratory of Advanced Manufacturing Technology, Guizhou University, China. Ph.D. Affiliation: Full professor. Email: gcyang@gzu.edu.cn
[4] State Key Laboratory of Mechanical Transmission, Chongqing University, China. Ph.D. Affiliation: Full professor. Email: junyangli@cqu.edu.cn

such as dead-zone hysteresis and chaotic oscillations, will reduce its operational performance, and even cause serious safety accidents. Therefore, it is of profound and lasting significance to design an effective controller to improve the robust performance of the MEMS gyroscope and suppress the chaotic oscillations within it.

With continuous in-depth research, many practical and effective strategies have been proposed, such as adaptive control, backstepping control, sliding mode control, and fuzzy control (Fei and Zhou, 2012; Luo and Song, 2016; Ouakad, Nayfeh, Choura, and Najar, 2015; Xu, Zhang, Li, He, and Shi, 2019). Aiming at a new 3-D chaotic system with an axe-shaped curve of equilibrium points, Vaidyanathan, Sambas, and Mamat (2018)constructed the analog circuits to reveal the dynamic characteristics of this system, and then designed an adaptive synchronization controller to carry out the stable control of this system. For a new five-dimensional four-wing hyperchatic system, they built the analog circuits to reveal motion behavior, and then implemented the synchronisation function via integral sliding mode control (Sambas, Chang, Dolvis, Jacques, and Vaidyanathan, 2019). The integral sliding mode control was designed to synchronize a new 2-scrill chaotic system with four quadratic nonlinear terms, and an analog circuit of the new 2-scroll chaotic system was constructed to check the feasibility of the model (Sambas, Vaidyanathan, Mamat, and Mohamed, 2020). For a three-axis MEMS gyroscope, Fei and Zhou (2012) discussed a robust adaptive control strategy through the coupling of fuzzy and sliding mode controls. In order to address the control problem of the MEMS resonator, Luo and Song (2016) proposed an adaptive backstepping control method based on RBF neural networks with output constraints and uncertain time delays. For the MEMS gyroscope, Xu *et al.* (2019) proposed a non-singular terminal sliding mode control method based on compound neural learning. Ouakad *et al.* (2015) designed a feedback controller to suppress the nonlinear motion of the microbeam resonator, and then used electronic circuits to build the controller to illustrate the feasibility of the design scheme. The control methods mentioned above have some disadvantages, such as slow response speeds, poor robustness and poor anti-interference ability.

The way to improve the robustness and enhance the anti-jamming capability of the MEMS gyroscope is an open issue. Sliding mode control is widely used in nonlinear systems because it shows strong robustness to parameter changes. The fractional sliding mode control method is an effective control method that can effectively suppress external disturbance and improve robustness of the controlled system (Rahmani and Rahman, 2019). For the MEMS gyroscope system, Fei and Chu (2016) proposed a dynamic global proportional integral derivative (PID) sliding mode control method and introduced a dynamic PID sliding surface to reduce chattering. For the robot flexible connecting rod system, Delavari *et al.* designed a fractional sliding mode control method and introduced a particle swarm optimization algorithm to adjust the controller parameters to obtain better control performance (Delavari, Lanusse, and

Sabatier, 2013). By comparing with the traditional non-singular sliding mode control, the fractional sliding mode control has better convergence precision. Sun and Ma (2017) presented a tracking fractional sliding mode terminal control method for linear motors. For the grid-connected doubly-fed induction generator system, Xiong, Wang, Mi, and Khan proposed a fractional-order sliding mode control method (2017). The simulation results show that the method can not only guarantee the asymptotical stability of all signals of the closed-loop system, but also has strong anti-interference abilities . The main shortcoming of the proposed fractional order sliding mode control is that the control target crosses the approach equilibrium point back and forth on both sides of sliding mode surface, which leads to chattering, thus affecting the control accuracy and even causing the controller performance to collapse.

In recent years, backstepping control has attracted wide attention due to its recursive and systematic control process (Li and Kang, 2010; T. Sun and Pan, 2019; Tong and Li, 2011). Unfortunately, there is an obvious flaw in traditional backstepping technology; virtual control signal causes "complex item explosions" due to repeated differentiation (Gao *et al.*, 2016; S. Gao, Dong, Ning, Tang, and Li, 2018). In order to address this defect, Pan, Wang, Li, and Yu investigated adaptive command-filtered backstepping control method wherein a command filter is used to eliminate these explosions (2017). Although the command filter can solve this issue, it brings about the issue of controller accuracy degradation. In view of this, a second-order tracking differentiator (Tian, Shen, and Dai, 2014) is introduced into the recursive process of traditional backstepping to solve the problem of "complex term explosions" and ensure the accuracy of the controller.

Motivated by the afore-mentioned research works, we developed an accelerated adaptive backstepping controller for the MEMS gyroscope. The main contributions of the accelerated adaptive backstepping control algorithm are emphasized as follows:

1) In the process of the accelerated adaptive backstepping controller design, the control input can reduce the adverse dead-zone effect in practical engineering applications, and a tracking differentiator is proposed to prevent the complex explosion associated with backstepping.

2) In order to accelerate the convergence speed and ensure that the system reaches a steady state faster, the speed function is integrated in the whole control policy. And the T2SFNN is designed to eliminate the effects of unknown functions and enhance the robustness of the controlled system.

3) Our algorithm not only reduces the chattering of the control input, but also improves the robustness of the system against parameter uncertainty and external interference.

Modeling of the MEMS gyroscope

A conventional MEMS gyroscope is mainly composed of a mass, a cantilever beam, a driving electrode, an induction device, and a base, where the driving electrode applies a driving force to the mass block to cause it to vibrate in the direction of the drive shaft. The displacement and velocity of the mass block in the direction of the detection axis can be measured with the induction device. The schematic diagram of the MEMS gyroscope is depicted in Figure 1.
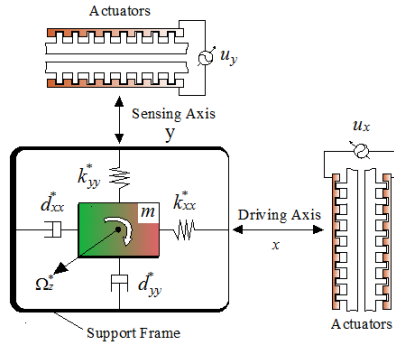
Figure 1. Schematic diagram of the MEMS gyroscope.
Source: Authors

Based on Newtonian mechanics and Kirchhoff's law, the dynamical Equation of the MEMS gyroscope can be expressed as follows (Fang, Yuan, and Fei, 2015; Yan, Hou, Fang, and Fei, 2016):

$$\left. \begin{array}{l} m\ddot{x} + d_{xx}^{*}\dot{x} + d_{xy}^{*}\dot{y} + k_{xx}^{*}x + k_{xy}^{*}y = u_{x}^{*} + d_{x} + 2m\Omega_{z}^{*}\dot{y} \\ m\ddot{y} + d_{xy}^{*}\dot{x} + d_{yy}^{*}\dot{y} + k_{xy}^{*}x + k_{yy}^{*}y = u_{y}^{*} + d_{y} - 2m\Omega_{z}^{*}\dot{x} \end{array} \right\} \quad (1)$$

where m represents the mass; k_{xy}^{*}, d_{xy}^{*} are damping and coupling coefficients; Ω_{z}^{*} is the angular velocity along the z-axes; d_{xx}^{*} and d_{yy}^{*} are the damping coefficients in the x-y axis direction; k_{xx}^{*} and k_{yy}^{*} represent the spring constant in the x-y axis direction; u_{x}^{*} and u_{y}^{*} are control inputs in x-y axis direction; and d_{x} and d_{y} indicate unknown disturbance in x-y axis direction, respectively.

Let $x_1 = x$, $x_2 = \dot{x}$, $x_3 = y$ and $x_4 = \dot{y}$, the dimensionless Equation governing the MEMS gyroscope is rewritten as follows:

$$\begin{aligned} \dot{x}_1 &= x_2 \\ \dot{x}_2 &= -d_{xx}x_2 - d_{xy}x_4 - \omega_x^2 x_1 - \omega_{xy}x_3 + 2\Omega_z x_4 \\ &\quad + d_x + D(u_x) \\ \dot{x}_3 &= x_4 \\ \dot{x}_4 &= -d_{xy}x_2 - d_{yy}x_4 - \omega_{xy}x_1 - \omega_y^2 x_3 - 2\Omega_z x_2 \\ &\quad + d_y + D(u_y) \end{aligned} \quad (2)$$

In Equation (2), a set of new parameters are introduced, such as:

$$\left. \begin{array}{l} d_{xx} = \dfrac{d_{xx}^{*}}{m\omega_0}, d_{xy} = \dfrac{d_{xy}^{*}}{m\omega_0} \\ d_{yy} = \dfrac{d_{yy}^{*}}{m\omega_0}, \Omega_z = \dfrac{\Omega_z^{*}}{m\omega_0}, \omega_x^2 = \dfrac{k_{xx}}{m\omega_0^2} \\ \omega_{xy} = \dfrac{k_{xy}}{m\omega_0^2}, \omega_y^2 = \dfrac{k_{yy}}{m\omega_0^2}, u_x = \dfrac{u_x^{*}}{m\omega_0^2 q_0}, u_y = \dfrac{u_y^{*}}{m\omega_0^2 q_0} \end{array} \right\} \quad (3)$$

where m, q_0 and ω_0^2 represent the quality of the mass, the reference length, and the square of the x-axes and y-axes resonance frequencies, respectively.

In practical engineering applications, friction and clearance of the internal components of the MEMS gyroscope cause asymmetrical dead-zone characteristics, which reduce control accuracy and system performance (Juan and Fei, 2013; Liu, Gao, Tong, and Li, 2015; Na, 2013).Therefore, it is necessary to establish an adaptive auxiliary signal to compensate the influence derived from the dead-zone input. The asymmetrical dead-zone inputs of the x-axes and y-axes can be defined as

$$\left. \begin{array}{l} h_{ri}(u_i - m_{ri}), \ u_i \geq m_{ri} \\ 0, -m_{li} < u_i < m_{ri}, \ i = x, y, \\ h_{li}(u_i + m_{li}), \ u_i \leq m_{li} \end{array} \right\} = D(u_i) \quad (4)$$

where h_{rx} and h_{lx} are the right and left slopes of the x-axes; h_{ry} and h_{ly} are the right and left slopes of the y-axes; m_{rx} and m_{lx} represent the breakpoints of the x-axes; m_{ry} and m_{ly} represent the breakpoints of the y-axes; and h_{ri}, h_{li}, m_{ri} and $m_{li}, i = x, y$ are positive constants. The dead-zone inputs can be rewritten as

$$D(u_i) = h_i u_i + m_i, \quad i = x, y, \quad (5)$$

where

$$\left. \begin{array}{l} h_{rx}, \ u_x \geq m_{rx} \\ 0, \ -m_{lx} < u_x < m_{rx} \\ h_{lx}, \ u_x \leq m_{lx} \end{array} \right\} = h_x$$

and

$$\left. \begin{array}{l} -h_{rx}m_{rx}, \ u_x \geq m_{rx} \\ 0, \ -m_{lx} < u_x < m_{rx} \\ h_{lx}m_{lx}, \ u_x \leq m_{lx} \end{array} \right\} = m_x$$

are constants of the x-axes dead-zone input.

$$\left. \begin{array}{l} h_{ry}, \ u_y \geq m_{ry} \\ 0, \ -m_{ly} < u_y < m_{ry} \\ h_{lx}, \ u_y \leq m_{ly} \end{array} \right\} = h_y$$

and

$$\left. \begin{array}{l} -h_{ry}m_{ry}, \ u_y \geq m_{ry} \\ 0, \ -m_{ly} < u_y < m_{ry} \\ h_{ly}m_{ly}, \ u_y \leq m_{ly} \end{array} \right\} = m_y$$

are constants of the y-axes dead-zone input.

There is $\underline{h}_i = \min(h_{ri}, h_{li}) \leq |h_i| \leq \overline{h}_i = \max(h_{ri}, h_{li})$, $|m_i| \leq \overline{m}_i = \max(h_{ri}m_{ri}, h_{li}m_{li}), i = x, y$.

Remark 1: Zhang, Zhang, Liu, and Kim *et al.* proposed an adaptive control method based on neural networks for the asymmetric dead-zone input in nonlinear system (2009). However, it can only be applied to specific conditions without universality, such as

$$\begin{cases} x_i(k+1) = x_{i+1}(k), \quad i = 1, \ldots, n-1 \\ x_n(k+1) = f(x(k)) + \Gamma(u(k)) + d_1(k), \end{cases}$$

and it has poor accuracy and robustness performance. The proposed scheme not only greatly reduces the chatter phenomenon, but also improves system performance and enhances its robustness to parameter uncertainty and external interference.

Dynamical analysis

In order to reveal the nonlinear characteristics of the MEMS gyroscope and explain the necessity of controller design, the dynamic analysis of the MEMS gyroscope is carried out when the dimensionless parameters of system are set as $\omega_x^2 = 355,3$, $\omega_y^2 = 532,9$, $\omega_{xy} = 70,99$, $d_{xx} = 0,01$, $d_{yy} = 0,01$, $\Omega_z = 0,1$ and $d_{xy} = 0,002$ (Rahmani and Rahman, 2019), and the initial values of the system states are set as $x_1(0) = 0,4$, $x_2(0) = 0$, $x_3(0) = 0,6$ and $x_4(0) = 0$. The sums of Lyapunov exponents x_1, x_2, x_3, and x_4 are $2,8884$, $-1,6952$, $1,1066$, and $-3,501$, respectively. The Kaplan-Yorke dimension of the MEMS gyroscope is calculated as $3,6569$ (Sambas, Mamat, Arafa, Mahmoud, and Sanjaya, 2019; Silva-Juarez, Rodriguez-Gomez, de la Fraga, Guillen-Fernandez, and Tlelo-Cuautle, 2019).

The phase diagrams and corresponding time histories are shown in Figure 2. The Lyapunov exponent diagram is shown in Figure 3. They reveal the dynamic characteristics of the MEMS gyroscope. It is easy to tell that the MEMS gyroscope exhibits chaotic motion. It is well known that this reduces accuracy and affects the running stability of the MEMS gyroscope. Meanwhile, this also fully illustrates thr fact that it is necessary to design a suitable control scheme to suppress the chaotic motion of the MEMS gyroscope and ensure the global asymptotic stability of the closed-loop system.
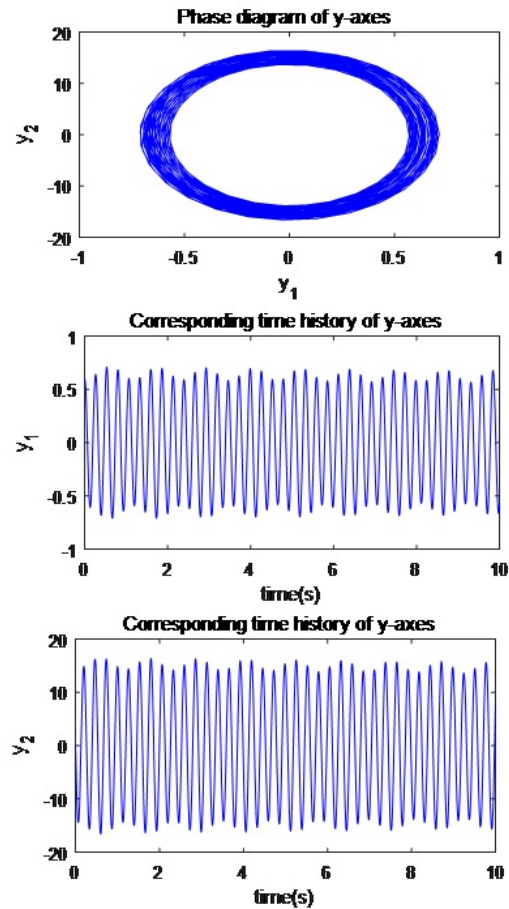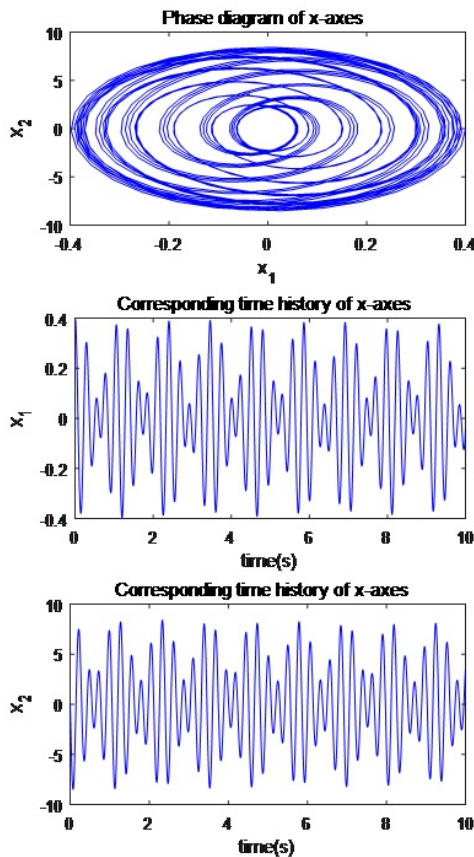
Figure 2. Phase diagrams and corresponding time histories.
Source: Authors
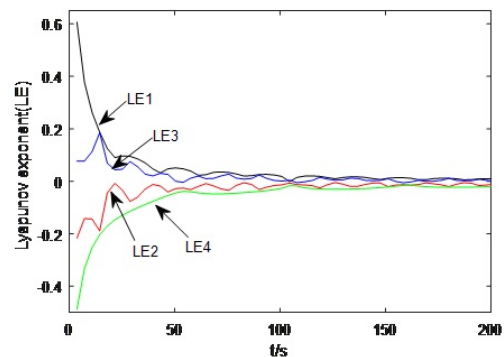
Figure 3. Lyapunov exponent diagram.
Source: Authors

Type-2 sequential fuzzy neural network

The T2SFNN is composed of fuzzy logic systems and neural networks. It avoids shortcomings such as slow speed, low precision, and high sample requirement of the fuzzy logic language and neural network reasoning (Mohammadzadeh and Ghaemi, 2018). The schematic diagram of the T2SFNN, consisting of the input layer, the fuzzification layer, the membership layer, the rule layer and the output layer, is

shown in Figure 4. The operating mechanism of the T2SFNN can be summarized as the following steps:

1) Based on the fuzzy theory, the upper input $\bar{I}_j^i$ and the lower input $\underline{I}_j^i$ on the membership layer can be written as

$$\left.\begin{array}{l} \bar{I}_j^i = \dfrac{\sigma_{\bar{A}_j}^2 c_{B_j^i} + \sigma_{\bar{B}_j^i}^2 I_j}{\sigma_{\bar{A}_j}^2 + \sigma_{\bar{B}_j^i}^2} \\[4mm] \underline{I}_j^i = \dfrac{\sigma_{\underline{A}_j}^2 c_{B_j^i} + \sigma_{\underline{B}_j^i}^2 I_j}{\sigma_{\underline{A}_j}^2 + \sigma_{\underline{B}_j^i}^2}, \; j = 1,2,\ldots,n, \; i = 1,2,\ldots,l \end{array}\right\} \quad (6)$$

where $\sigma_{\bar{A}_j}^2$ and $\sigma_{\bar{B}_j^i}^2$ are the upper widths of the membership functions; $\sigma_{\underline{A}_j}^2$ and $\sigma_{\underline{B}_j^i}^2$ denote the lower widths of the membership functions; and $c_{B_j^i}$ and I_j represent the center and input of the membership function, respectively.

For Equation (6), the upper membership function and the lower membership function can be calculated as:

$$\bar{B}_j^i = \exp\left[\frac{-\left\|\bar{I}_j^i - c_{B_j^i}\right\|^2}{\sigma_{\bar{B}_j^i}^2}\right] \underline{B}_j^i = \exp\left[\frac{-\left\|\underline{I}_j^i - c_{B_j^i}\right\|^2}{\sigma_{\underline{B}_j^i}^2}\right] \quad (7)$$

2) A series of fuzzy IF-THEN rules set of the fuzzy neural network can be expressed in the following form:

IF I_1 is $B_1^i \cdots$ and I_j is B_j^i and $\cdots I_n$ is B_n^i, $j = 1,2,\ldots,n$, $i = 1,\ldots,l$, then

$$O \in \left[\bar{\theta}_i, \underline{\theta}_i\right], \quad (8)$$

where B_j^i is the ith membership function for the jth input.

The upper and lower firing rules of the fuzzy neural network can be expressed in the following forms:

$$\left.\begin{array}{l} \bar{\xi}_i(t) = r\bar{\xi}_i(t-1) + \bar{B}_j^i \\[2mm] \underline{\xi}_i(t) = r\underline{\xi}_i(t-1) + \underline{B}_j^i, \quad i = 1,2,\ldots,l \end{array}\right\} \quad (9)$$

where $\bar{\xi}_i(t)$ and $\underline{\xi}_i(t)$ are the upper and lower of the fuzzy neural network ith rule at previous sample time, respectively; $\bar{\xi}_i(t-1)$ and $\underline{\xi}_i(t-1)$ indicate the upper and lower mapping degrees of the ith rule at the last sample time; r is the design parameter; $\bar{B}_j^i$ and $\underline{B}_j^i$ are the upper/lower membership functions.

3) The output of the T2SFNN can be written as:

$$O(t) = \frac{\sum_{i=1}^{l} \bar{\theta}_i(t)\bar{\xi}_i(t) + \sum_{i=1}^{l} \underline{\theta}_i(t)\underline{\xi}_i(t)}{2} \quad (10)$$

where $\bar{\theta}_i$ and $\underline{\theta}_i$ are considered to be the upper and lower of inputs, and they can be designed in the following forms:

$$\left.\begin{array}{l} \bar{\theta}_i = \bar{\alpha}_i^0(t) + \bar{\alpha}_i^1(t)I_1(t) + \cdots + \bar{\alpha}_i^n(t)I_n(t) \\[2mm] \underline{\theta}_i = \underline{\alpha}_i^0(t) + \underline{\alpha}_i^1(t)I_1(t) + \cdots + \underline{\alpha}_i^n(t)I_n(t), \; i = 1,2,\ldots,l \end{array}\right\} \quad (11)$$
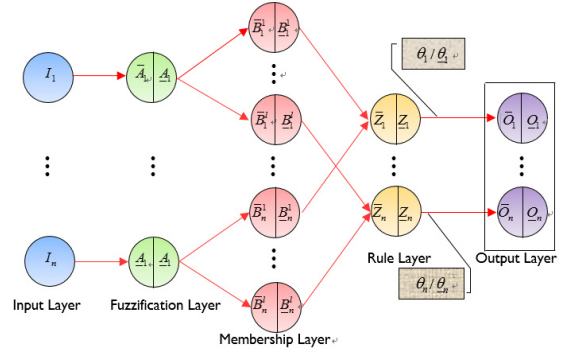
Figure 4. Schematic diagram of the T2SFNN.
Source: Authors

where $\bar{\alpha}_i^j(t), \underline{\alpha}_i^j(t)$, $i = 1,\ldots,l$, $j = 1,\ldots,n$ are the positive constant.

Equation (9) can be re-expressed as follows:

$$O(t) = \theta^T(t)\xi(t) \quad (12)$$

where

$$\theta(t) \equiv \left[\begin{array}{l} \bar{\alpha}_1^0,\ldots,\bar{\alpha}_1^n,\ldots,\bar{\alpha}_l^0,\ldots,\bar{\alpha}_l^n \\[2mm] \underline{\alpha}_1^0,\ldots,\underline{\alpha}_1^n,\ldots,\underline{\alpha}_l^0,\ldots,\underline{\alpha}_l^n \end{array}\right]$$

is the weight vector,

$$\xi(t) = \left[\begin{array}{l} \bar{\xi}_1(t),\ldots,\bar{\xi}_1(t)I_n(t),\ldots,\bar{\xi}_l(t),\ldots,\bar{\xi}_l(t)I_n(t), \\[2mm] \underline{\xi}_1(t),\ldots,\underline{\xi}_1(t)I_n(t),\ldots,\underline{\xi}_l(t),\ldots,\underline{\xi}_l(t)I_n(t) \end{array}\right]^T$$

is the input of the neural network.

Remark 2: With the increase of the membership layers, the approximation accuracy of the T2SFNN improves. However, calculation complexity increases significantly, which consumes too much computation time. Therefore, we adopt the golden section method to select the appropriate number of fuzzy layers. Then, the output accuracy meets the design requirements, and the computational complexity is acceptable.

Lemma 1 (Gao *et al.*, 2016): For any continuous function $f(x)$, there is a T2SFNN that satisfies

$$\sup_{x\in\Omega}\left|f(x) - \hat{f}(x,\theta)\right| \leq \varepsilon(x), \quad (13)$$

where $\hat{f}$ is the estimation of f and $\varepsilon(x)$ is the approximate error of the T2SFNN.

We defined an optimal parameter θ^* being equal to $\arg\min_{\theta\in\Omega_\theta}\left[\sup_{x\in\Omega}\left|f(x) - \hat{f}(x,\theta)\right|\right]$, where Ω_θ is a compact set of x and Ω_θ is a compact set of θ. Let $\tilde{\theta} = \theta^* - \hat{\theta}$ with θ^* being a virtual item. For any constant $\bar{\varepsilon} > 0$, there is $|\varepsilon(x)| \leq \bar{\varepsilon}$.

Controller design

The rate function to accelerate convergence is introduced as (Luo, Li, Li, and Hu, 2020):

$$
\left.\begin{array}{ll}
\dfrac{T^4 \kappa(t)}{(1-b_\varphi)(T-t)^4 + b_\varphi T^4 \kappa(t)}, & 0 \le t \le T \\[2mm]
1/b_\varphi, & t \ge T
\end{array}\right\} = \varphi(t) \qquad (14)
$$

where $0 < T < \infty$ is the specified time, $\kappa(t)$ represents any monotone non-decreasing time smoothing function satisfying $\kappa(0) = 1$ and $\dot{\kappa}(t) \ge 0$. b_φ is a design parameter which satisfies $0 < b_\varphi \ll 1$. Let $\beta_\varphi = \dot{\varphi}(t)/\varphi(t)$, where $\dot{\varphi}(t)$ is a continuous differentiable and bounded function. Additionally, $\varphi(t)$ is a positive and strictly monotone increasing function, and it has an initial value of $\varphi(0) = 1$.

In order to avoid the explosion of differential complex terms associated with traditional backstepping, a second-order tracking differentiator is introduced (Tian et al., 2014):

$$
\left.\begin{array}{l}
\dot{\vartheta}_1 = -r_1 |\vartheta_1 - \alpha_r|^{1/2} sign(\vartheta_1 - \alpha_r) + \vartheta_2 \\[2mm]
\dot{\vartheta}_2 = -r_2 sign(\vartheta_2 - \dot{\vartheta}_1)
\end{array}\right\} \qquad (15)
$$

where r_1, r_2 are positive numbers; α_r is the virtual control law; and ϑ_1 and ϑ_2 stand for the tracking differentiator states.

Lemma 2: If the initial condition $|\vartheta_1(t_0) - \alpha_r(t_0)| \le \wp$ with $\wp > 0$, then, for any small positive numbers l_{ϑ_1} and l_{ϑ_2}, the following inequality holds:

$$
|\vartheta_1 - \alpha_r| \le l_{\vartheta_1}, |\vartheta_2 - \dot{\alpha}_r| \le l_{\vartheta_2}. \qquad (16)
$$

Assumption 1: The desired tracking trajectories x_{id} and their derivatives are continuous and available, and they satisfy the constraints, so that $-t_i \le x_{id} \le t_i$, $i = 1, 3$.

Tracking errors are defined as

$$
\left.\begin{array}{ll}
e_i = x_i - x_{id}, & i = 1, 3 \\[1mm]
e_i = x_i - \alpha_i, & i = 2, 4
\end{array}\right\} \qquad (17)
$$

where x_i, $i = 1, \ldots, 4$ are control inputs; α_i, $i = 2, 4$ stand for virtual control laws; and e_i, $i = 1, \ldots, 4$ indicate tracking errors.

At this time, the accelerated tracking compensation errors of the controller can be designed as follows:

$$
S_i = \varphi e_i, \quad i = 1, \ldots, 4, \qquad (18)
$$

where S_i, $i = 1, \ldots, 4$ represent accelerated errors.

According to the idea of backstepping, the acceleration adaptive backstepping controller design includes four steps:

Step 1: The derivation of S_1 can be deduced:

$$
\dot{S}_1 = \varphi(\beta_\varphi e_1 + e_2 + \alpha_2 - \dot{x}_{1d}). \qquad (19)
$$

Then the virtual control α_2 is designed as

$$
\alpha_2 = -\dfrac{k_1 e_1}{M_1 \cos(\pi S_1/2B_1)} - \beta_\varphi e_1 + \dot{x}_{1d}, \qquad (20)
$$

where $M_1 = \dfrac{2 + \pi S_1 \tan(\pi S_1/2B_1)/2B_1}{\cos(\pi S_1/2B_1)}$; k_1 is a positive constant; and the parameter $B_1 > 0$ satisfies the constraint of the accelerated error as $|S_1| < B_1$.

The first Lyapunov candidate function can be designed

$$
V_1 = \dfrac{S_1^2}{\cos(\pi S_1/2B_1)}. \qquad (21)
$$

Substituting Equation (20) into (19), the derivation of V_1 can be deduced as

$$
\dot{V}_1 = -\dfrac{k_1 S_1^2}{\cos(\pi S_1/2B_1)} + M_1 S_1 S_2. \qquad (22)
$$

Step 2: The derivation of S_2 can be calculated as follows:

$$
\dot{S}_2 = \varphi(\beta_\varphi e_2 + f_2(\cdot) + d_x + u_x - \dot{\alpha}_2), \qquad (23)
$$

where $f_2(\cdot) = -d_{xx}x_2 - d_{xy}x_4 - \omega_x^2 x_1 - \omega_{xy}x_3 + 2\Omega_z x_4$ stands for an unknown nonlinear term, since system parameters such as $d_{xx}, d_{xy}, \omega_x^2, \omega_{xy}, \Omega_z$ are uncertain. The T2SFNN has strong nonlinear mapping abilities and can approximate any unknown nonlinear term with high precision. Consequently, one has

$$
f_2(\cdot) = \theta_2^T \xi_2 + \varepsilon_2. \qquad (24)
$$

The second Lyapunov candidate function is designed as

$$
V_2 = V_1 + \dfrac{S_2^2}{\cos(\pi S_2/2B_2)}. \qquad (25)
$$

From Equation (25), the derivation of V_2 can be deduced as

$$
\dot{V}_2 = \dot{V}_1 + S_2 \dot{S}_2 M_2. \qquad (26)
$$

where $M_2 = \dfrac{2 + \pi S_2/2B_2 \tan(\pi S_2/2B_2)}{\cos(\pi S_2/2B_2)}$.

According to Lemma 2, the derivative of α_2 can be obtained through a second-order tracking differential:

$$
\left.\begin{array}{l}
\dot{\vartheta}_3 = -r_3 |\vartheta_3 - \alpha_2|^{1/2} sign(\vartheta_3 - \alpha_2) + \vartheta_4 \\[2mm]
\dot{\vartheta}_4 = -r_4 sign(\vartheta_4 - \dot{\vartheta}_3)
\end{array}\right\} \qquad (27)
$$

where the bound filtering error satisfies $|\vartheta_4 - \dot{\alpha}_2| \le l_{\vartheta_4}$.

The control input with the corresponding adaptive law can be designed as

$$
u_x = -\hat{\theta}_2^T \xi_2 - \beta_\varphi e_2 + \vartheta_4 \qquad (28)
$$

$$
\dot{\hat{\theta}}_2 = \gamma_2 S_2 M_2 \xi_2 - 2\lambda_2 \hat{\theta}_2, \qquad (29)
$$

where the design parameter k_2, γ_2 and λ_2 are positive constants, and the parameter $B_2 > 0$ satisfies the constraint of the accelerated error as $|S_2| < B_2$.

Substituting Equations (22), (23) and (28) into (26) yields

$$
\begin{aligned}
\dot{V}_2 \le & -\sum_{i=1}^{2} \dfrac{k_i S_i^2}{\cos(\pi S_2/2B_2)} + \dfrac{M_2^2 d_x^2}{2} \\
& - \varphi^2 S_2^2 + \varphi S_2 M_2(f_2(\cdot) - \hat{\theta}_2^T \xi_2) + S_2 M_2 \varphi l_{\vartheta_4}.
\end{aligned} \qquad (30)
$$

Step 3: The derivative of S_3 to time t can be calculated as

$$\dot{S}_3 = \varphi\left(\beta_\varphi e_3 + e_4 + \alpha_4 - \dot{x}_{3d}\right). \tag{31}$$

And the chosen virtual control input α_4 as

$$\alpha_4 = -\frac{k_3 \bar{e}_3}{M_3 \cos\left(\pi S_3/2B_3\right)} - \beta_\varphi e_3 + \dot{x}_{3d}, \tag{32}$$

where $M_3 = \frac{2 + \frac{\pi}{2B_3} S_3 \tan(\pi S_3/2B_3)}{\cos(\pi S_3/2B_3)}$, the design parameter k_3 is a positive constant, and the parameter $B_3 > 0$ satisfies the constraints of the accelerated error as $|S_3| < B_3$.

The third Lyapunov candidate function can be designed as follows:

$$V_3 = V_2 + \frac{S_3^2}{\cos\left(\pi S_3/2B_3\right)}. \tag{33}$$

The derivation of V_3 can be deduced as

$$\dot{V}_3 = \dot{V}_2 + S_3 \dot{S}_3 M_3. \tag{34}$$

Substituting α_4, $\dot{S}_3$ and $\dot{V}_2$ into $\dot{V}_3$ yields

$$
\begin{aligned}
\dot{V}_3 \leq &-\sum_{i=1}^{3} \frac{k_i S_i^2}{\cos\left(\pi S_i/2B_i\right)} - \frac{\varphi^2 S_2^2}{2} + \frac{M_2^2 d_x^2}{2} \\
&+ M_3 S_3 S_4 + \varphi S_2 M_2 \left(f_2\left(\cdot\right) - \hat{\theta}_2^T \xi_2\right) \\
&+ S_2 M_2 \varphi l_{\vartheta_4}.
\end{aligned} \tag{35}
$$

Step 4: The last Lyapunov candidate function can be designed as

$$V_4 = V_3 + \frac{S_4^2}{\cos\left(\pi S_4/2B_4\right)}. \tag{36}$$

where the parameter $B_4 > 0$ satisfies the constraints of the accelerated error as $|S_4| < B_4$.

Calculating the derivative of S_4 with respect to time t results in

$$\dot{S}_4 = \varphi\left(\beta_\varphi e_4 + f_4\left(\cdot\right) + d_y + u_y - \dot{\alpha}_4\right), \tag{37}$$

where $f_4\left(\cdot\right) = -d_{xy}x_2 - d_{yy}x_4 - \omega_{xy}x_1 - \omega_y^2 x_3 - 2\Omega_2 x_2$ stands for an unknown continuous function. We can employ the T2SFNN to approximate it again as

$$f_4\left(\cdot\right) = \theta_4^T \xi_4 + \varepsilon_4. \tag{38}$$

As in step 2, the derivative of α_4 can be obtained through a second-order tracking differential:

$$\left.\begin{aligned}
\dot{\vartheta}_5 &= -r_5 \left|\vartheta_5 - \alpha_4\right|^{1/2} sign\left(\vartheta_5 - \alpha_4\right) + \vartheta_6 \\
\dot{\vartheta}_6 &= -r_6 sign\left(\vartheta_6 - \dot{\vartheta}_5\right)
\end{aligned}\right\} \tag{39}$$

where the bound filtering error satisfies $\left|\vartheta_6 - \dot{\alpha}_4\right| \leq l_{\vartheta_6}$.

The control input with the corresponding adaptive law can be designed as

$$u_y = -\hat{\theta}_4^T \xi_4 - \beta_\varphi e_4 + \vartheta_6 \tag{40}$$

$$\dot{\hat{\theta}}_4 = \gamma_4 S_4 M_4 \xi_4 - 2\lambda_4 \hat{\theta}_4, \tag{41}$$

where the design parameters k_4, γ_4 and λ_4 are positive.

The derivative of V_4 can be computed as follows:

$$\dot{V}_4 = \dot{V}_3 + S_4 \dot{S}_4 M_4 \tag{42}$$

where $M_4 = \frac{2 + \frac{\pi}{2B_4} S_4 \tan(\pi S_4/2B_4)}{\cos(\pi S_4/2B_4)}$.

Substituting u_y, $\dot{S}_4$ and $\dot{V}_3$ into $\dot{V}_4$ yields

$$
\begin{aligned}
\dot{V}_4 \leq &-\sum_{i=1}^{4} \frac{k_i S_i^2}{\cos\left(\pi S_i/2B_i\right)} \\
&+ \sum_{j=2,4,k=x,y} \frac{M_j^2 d_k^2}{2} - \sum_{j=2,4} \varphi^2 S_j^2 \Big/ 2
\end{aligned} \tag{43}
$$

Stability analysis

Lemma 3: Consider the control equation of the MEMS gyroscope described by Equation (2). The accelerated adaptive backstepping control inputs are designed as (20), (28), (32) and (40) with adaptive laws (29), (41). If Assumption 1 holds, and the initial conditions of the MEMS gyroscope with dead-zone inputs satisfy $x_1(0) \in (-B_1 + x_{1d}(0), B_1 + x_{1d}(0))$ and $x_3(0) \in (-B_3 + x_{3d}(0), B_3 + x_{3d}(0))$, then the following conclusions can be drawn:

1) All signals in the closed system are ultimately bounded in a uniform way, and the output constraint is never violated.

2) The issues with chaos oscillation and asymmetric dead-zone in the MEMS gyroscope system are solved, and the transient response speed of the system is improved by employing an acceleration function.

Proof: The whole Lyapunov function candidate is chosen as

$$V = \sum_{i=1}^{4} \frac{S_i^2}{\cos\left(\pi S_i/2B_i\right)} + \sum_{i=2,4} \frac{1}{2\gamma_i} \tilde{\theta}_i^T \tilde{\theta}_i. \tag{44}$$

The derivation of V regard to the time is

$$\dot{V} \leq \sum_{j=2,4} \left(\tilde{\theta}_j^T \left(S_j M_j \xi_j - \frac{1}{\gamma_j} \dot{\hat{\theta}}_j\right) + \frac{M_j^2 \varepsilon_j^2}{2}\right) \tag{45}$$

Substituting Equations (29) and (41) into (45) yields

$$\dot{V} \leq \sum_{j=2,4} \left(\frac{\lambda_j}{\gamma_j} \left(2\theta_j^{*T} \hat{\theta}_j - 2\theta_j^T \hat{\theta}_j\right) + \frac{M_j^2 \varepsilon_j^2}{2}\right) \tag{46}$$

From the Young's inequality, the following can be obtained:

$$\left.\begin{aligned}
\theta^{*T} \theta^* + \hat{\theta}^T \hat{\theta} &\geq 2\theta^{*T} \hat{\theta} \\
\theta^{*T} \hat{\theta} - \hat{\theta}^T \hat{\theta} &\leq \tfrac{1}{2}\theta^{*T}\theta^* - \tfrac{1}{2}\hat{\theta}^T\hat{\theta}
\end{aligned}\right\} \tag{47}$$

Substituting (47) into (46) yields

$$
\begin{aligned}
\dot{V} \leq &-\sum_{i=1}^{4} \frac{k_i S_i^2}{\cos\left(\pi S_i/2B_i\right)} + \sum_{j=2,4} \frac{M_j^2 l_{\vartheta_{j+2}}^2}{2} + \sum_{j=2,4,k=x,y} \frac{M_j^2 d_k^2}{2} \\
&+ \sum_{i=2,4} \left(\frac{\lambda_j}{\gamma_j}\left(-\theta_j^{*T}\theta_j^* - \hat{\theta}_j^T\hat{\theta}_j\right) + \frac{2\lambda_j}{\gamma_j}\theta_j^{*T}\theta_j^{*T} + \frac{M_j^2 \varepsilon_j^2}{2}\right).
\end{aligned} \tag{48}
$$

From $\tilde{\theta} = \theta^* - \hat{\theta}$, it has

$$\tilde{\theta}^T \tilde{\theta} = \theta^{*T}\theta^* - 2\theta^{*T}\hat{\theta} + \hat{\theta}^T\hat{\theta} \leq 2\theta^{*T}\theta^* + 2\hat{\theta}^T\hat{\theta}. \qquad (49)$$

From (48), Equation (47) can be rewritten as

$$\dot{V} \leq -\sum_{i=1}^{4} \frac{k_i S_i^2}{\cos(\pi S_i/2B_i)} + \sum_{j=,4,k=x,y} \frac{M_j^2 d_k^2}{2}$$
$$+ \sum_{j=2,4} \left(\frac{2\lambda_j}{\gamma_j}\theta_j^{*T}\theta_j^* + \frac{M_j^2 \varepsilon_j^2}{2} - \frac{\lambda_j}{2\gamma_j}\tilde{\theta}_j^T\tilde{\theta}_j \right) \qquad (50)$$
$$+ \sum_{j=2,4} \frac{M_j^2 l_{\vartheta_{j+2}}^2}{2} = -a_0 V + b_0 + c_0.$$

where $a_0 = \min\{k_1, k_2, k_3, k_4, \lambda_2, \lambda_4\}$, $b_0 = \sum_{j=2,4} \frac{M_j^2 \varepsilon_j^2}{2} + \sum_{j=2,4} \frac{2\lambda_j}{\gamma_2}\theta_j^{*T}\theta_j^*$ and $c_0 = \sum_{j=2,4} \frac{M_j^2 l_{\vartheta_{j+2}}^2}{2} + \sum_{j=2,4,k=x,y} \frac{M_j^2 d_k^2}{2}$.

According to the general solution of the first-order linear differential equation, the solution of (50) can be expressed as

$$\dot{V}(t) \leq \frac{b_0 + c_0}{a_0} + \left(V(t_0) - \frac{b_0 + c_0}{a_0} \right) e^{-a_0(t-t_0)} \qquad (51)$$

thus defining a compact set as follows:

$$\Omega \equiv \{t \,|\, V(t) \leq C_0\} \in R. \qquad (52)$$

where $C_0 = V(0) + \frac{b_0 + c_0}{a_0}$.

From $\dot{V} \leq -a_0 V + b_0 + c_0 < 0$, it can be obtained that all signals of the closed-loop system are ultimately bounded in a uniform way. There is

$$\left(S_1, S_2, S_3, S_4, \tilde{\theta}_2, \tilde{\theta}_4 \right)^T \in R^{6 \times 1}. \qquad (53)$$

By integrating Equation (50) into interval $[0, T]$, one has

$$\int_0^T \dot{V} dt \leq -\int_0^T a_0 \sum_{i=1}^{4} \frac{k_i S_i^2}{\cos(\pi S_i/2B_i)} dt + Tb_0 \qquad (54)$$

After a series of mathematical transformations, (54) can be further expressed as

$$-\sum_{i=1}^{4} \int_0^T \frac{k_i S_i^2}{\cos(\pi S_i/2B_i)} dt \leq \frac{1}{a_0}(V(0) - V(T) + Tb_0)$$
$$+ \frac{1}{a_0} \int_0^T \left(\sum_{j=2,4} \frac{M_j^2 l_{\vartheta_{j+2}}^2}{2} + \sum_{j=2,4,k=x,y} \frac{M_j^2 d_k^2}{2} \right) dt. \qquad (55)$$

Since $-\frac{V(T)}{a_0} \leq 0$, Equation (55) can be further expressed as follows

$$-\sum_{i=1}^{4} \int_0^T \frac{k_i S_i^2}{\cos(\pi S_i/2B_i)} dt \leq \frac{1}{a_0}(V(0) + Tb_0)$$
$$+ \int_0^T \left(\sum_{j=2,4} \frac{M_j^2 l_{\vartheta_{j+2}}^2}{2} + \sum_{j=2,4,k=x,y} \frac{M_j^2 d_k^2}{2} \right) dt. \qquad (56)$$

The convergence results show that the accuracy of the final error mainly depends on the upper bound of external disturbances and approximation errors.

Numerical simulation

In this section, the results of the numerical simulation analysis are provided to testify the effectiveness of our scheme. Suppose that the initial values of the MEMS gyroscope are chosen as $x_1(0) = 0,4$, $x_2(0) = 0$, $x_3(0) = 0,6$ and $x_4(0) = 0$, the tracking trajectories are set as $x_{1d} = 0,1\sin(4,17t+1) + 0,1$, and $x_{3d} = 0,12\sin(5,11t+1,2) + 0,12$. The external disturbances can be defined as $d_x = x_1\sin(t)$ and $d_y = x_3\sin(t)$. The parameters of the designed controller are set as $k_1 = 112$, $k_2 = 64$, $k_3 = 128$, $k_4 = 72$, $\gamma_2 = 2$, $\gamma_4 = 2$, $\lambda_2 = 1,5$, $\lambda_4 = 1,5$. Additionally, the center of membership functions are chosen as $[-1, -0,5, 0, 0,5, 1]$. The parameters of the T2SFNN are selected as $\sigma_{\bar{\mu}_j^i} = 1$, $\sigma_{\underline{\mu}^i} = 0,1$, $\sigma_{\bar{f}_j} = 0,5$, $\sigma_{\underline{f}_j} = 0,05$ and $r = 0,05$.

Trajectory tracking is shown in Figure 5. It is obvious that the desired tracking trajectories almost match the actual signal trajectories throughout the course of time, while it shows that the proposed scheme can suppress chaotic motion. Trajectory tracking errors of x-axis and y-axis for different external disturbances are depicted in Figure 6. For different external disturbances, tracking errors only have a small fluctuation in the beginning. This shows that the designed control scheme can eliminate the interference originated from external disturbances. Control inputs for different Ω_z are depicted in Figure 7. From it, we can determine that the control output is almost unaffected as parameter Ω_z changes. Obviously, the proposed control scheme has a strong robustness to parameter perturbations.
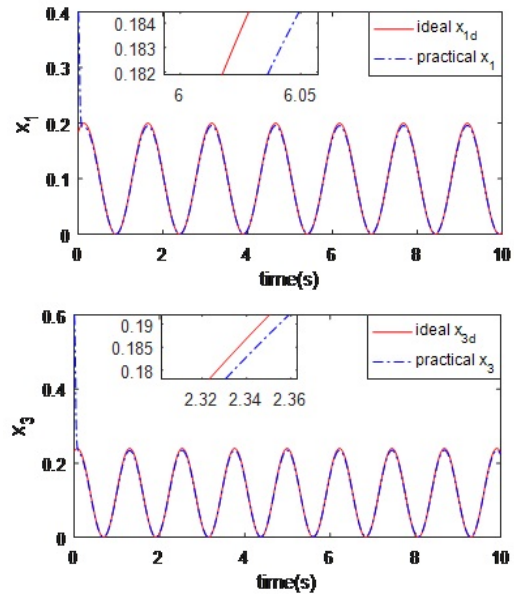
Figure 5. Position tracking of x-axis and y-axis.
Source: Authors
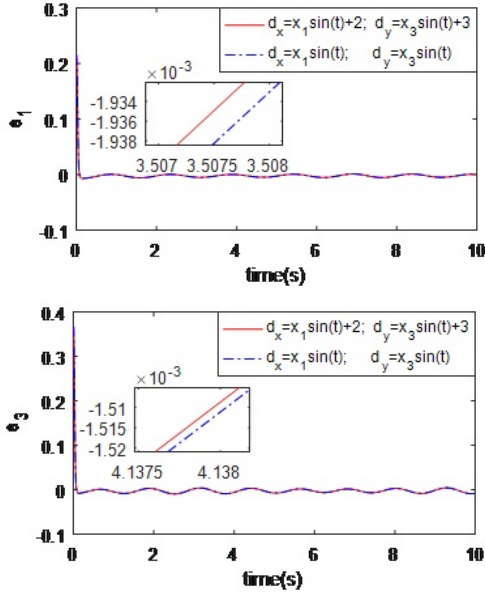
Figure 6. Position tracking errors of x-axis and y-axis for different external disturbances.
Source: Authors

Figure 7. Control inputs of x-axis and y-axis for different Ω_z.
Source: Authors

Figure 8. Position tracking contrast of x-axis and y-axis between adaptive fuzzy dynamic surface control and the proposed method.
Source: Authors
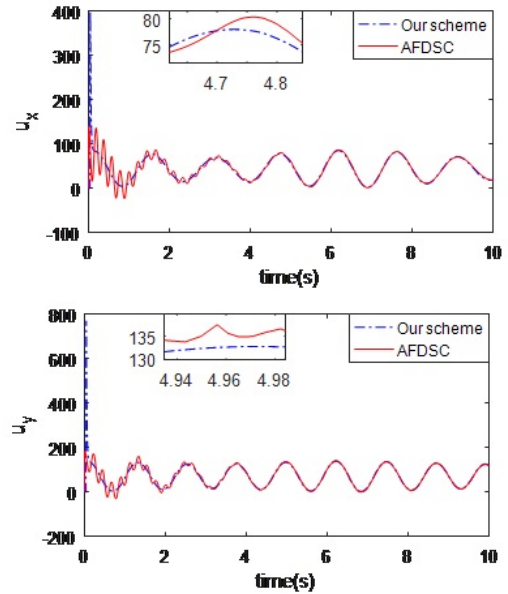
Figure 9. Control inputs contrast of x-axis and y-axis between adaptive fuzzy dynamic surface control and the proposed method.
Source: Authors

To show the superiority of our scheme, we made a comparison with adaptive fuzzy dynamic surface control (AFDSC) originated from (Lei, Cao, Wang, and Fei, 2017), and the control input can be written as follows:

$$u = -\hat{\theta}^T \xi(x) + \dot{\alpha}_1 - c_2 z_2 - \eta sgn(z_2), \qquad (57)$$

where $z_2 = x_2 - \alpha_1$, c_2 is a non-zone positive constant, the sliding mode term $\eta sgn(z_2)$ is a kind of compensation for the error of the fuzzy approximation, and η is a positive constant.

Figures 8 and 9 illustrate the trajectory tracking performance contrast between the adaptive fuzzy dynamic surface control and the proposed method. In turn, from Figures 7 and 8, it can be clearly concluded that the proposed control scheme has better performance than the adaptive fuzzy dynamic surface control.

Conclusion

In this paper, an accelerated adaptive backstepping control algorithm is proposed to address the control problem of the MEMS gyroscope with chaotic behavior, unknown external disturbances, and dead-zone inputs. In order to better reveal chaotic behavior of the MEMS gyroscope, the phase diagram and corresponding time history diagram are established. In the controller design process, the Lyapunov energy function is designed to make sure the output state of this system is constrained, the dead-zone control inputs are established to eliminate the adverse influence of the dead-zone input on the performance of the MEMS gyroscopes and T2SFNN is used to approximate unknown functions of the dynamic system. In order to accelerate the convergence speed and ensure that the system reaches a steady state faster, the speed function is established. The problem of complex terms explosion in traditional backstepping method is solved by combining the tracking differentiator with backstepping method. The stability analysis shows that the proposed scheme can ensure the global asymptotic stability of the closed-loop system. Finally, the simulation and comparison results show that the proposed control scheme has better control performance. In the near future, we will construct analog circuits to reveal the dynamic behavior of the fractional order MEMS gyroscope, and then design an effective controller to perform stable control of the fractional order MEMS gyroscope.

Acknowledgments

References

Chong, S., Rui, S., Jie, L., Xiaoming, Z., Jun, T., Yunbo, S., Jun, L., and Huiliang, C. (2016). Temperature drift modeling of MEMS gyroscope based on genetic-Elman neural network. *Mechanical Systems And Signal Processing, 72*, 897-905. 10.1016/j.ymssp.2015.11.004

Delavari, H., Lanusse, P., and Sabatier, J. (2013). Fractional order controller design for a flexible link manipulator robot. *Asian Journal of Control, 15*(3), 783-795. 10.1002/asjc.677

Fang, Y., Fei, J., and Yang, Y. (2018). Adaptive Backstepping Design of a Microgyroscope. *Micromachines, 9*(7), 338. 10.3390/mi9070338

Fang, Y., Yuan, Z., and Fei, J. (2015). Adaptive Fuzzy Backstepping Control of MEMS Gyroscope Using Dynamic Sliding Mode Approach. *Information Technology and Control, 44*(4), 380-386 10.5755/j01.itc.44.4.9110

Fei, J. and Chu, Y. (2016). Dynamic Global PID Sliding Mode Control for MEMS Gyroscope Using Adaptive Neural Controller. In IEEE (Eds.) 2016 Joint 8th International Conference on Soft Computing and Intelligent Systems (SCIS) and 17th International Symposium on Advanced Intelligent Systems (ISIS) (pp. 16-21). New York, NY: IEEE. 10.1109/SCIS-ISIS.2016.0018

Fei, J. and Zhou, J. (2012). Robust adaptive control of MEMS triaxial gyroscope using fuzzy compensator. *IEEE Transactions on Systems, Man, and Cybernetics, Part B (Cybernetics), 42*(6), 1599-1607. 10.1109/TSMCB.2012.2196039

Gao, Ying, Tong, Shaocheng, Yongming, Liu, and Yan-Jun. (2016). Fuzzy Approximation-Based Adaptive Backstepping Optimal Control for a Class of Nonlinear Discrete-Time Systems With Dead-Zone. *IEEE Transactions on Fuzzy Systems: A Publication of the IEEE Neural Networks Council, 24*(1), 16-28. 10.1109/TFUZZ.2015.2418000

Gao, S., Dong, H., Ning, B., Tang, T., and Li, Y. (2018). Nonlinear mapping-based feedback technique of dynamic surface control for the chaotic PMSM using neural approximation and parameter identification. *IET Control Theory and Applications, 12*(6), 819-827. 10.1049/iet-cta.2017.0550

Juan, W. and Fei, J. (2013). Adaptive fuzzy approach for non-linearity compensation in MEMS gyroscope. *Transactions of the Institute of Measurement and Control, 35*(8), 1008-1015. 10.1177/0142331212472224

Lei, D., Cao, D., Wang, T. and Fei, J. (2017). Adaptive Dynamic Surface Control of MEMS Gyroscope Sensor Using Fuzzy Compensator. *IEEE Access, 4*, 4148-4154. 10.1109/ACCESS.2016.2596538

Li, Z. and Kang, Y. (2010). Dynamic coupling switching control incorporating support vector machines for wheeled mobile manipulators with hybrid joints. *Automatica, 46*(5), 832-842. 10.1016/j.automatica.2010.02.019

Lin, J., Li, Y., and Yang, G. (2020). FPGAN: Face de-identification method with generative adversarial networks for social robots. *Neural Networks, 133*, 132-147. 10.1016/j.neunet.2020.09.001

Liu, Y.-J., Gao, Y., Tong, S., and Li, Y. (2015). Fuzzy approximation-based adaptive backstepping optimal control for a class of nonlinear discrete-time systems with dead-zone. *IEEE Transactions on Fuzzy Systems, 24*(1), 16-28. 10.1109/TFUZZ.2015.2418000

Luo, S., Li, J., Li, S., and Hu, J. (2020). Dynamical analysis of the fractional-order centrifugal flywheel governor system and its accelerated adaptive stabilization with the optimality. *International Journal of Electrical Power and Energy Systems, 118*, 105792. 10.1016/j.ijepes.2019.105792

Luo, S. and Song, Y. (2016). Chaos analysis-based adaptive backstepping control of the microelectromechanical resonators with constrained output and uncertain time delay. *IEEE Transactions on Industrial Electronics, 63*(10), 6217-6225. 10.1109/TIE.2016.2569462

Mohammadzadeh, A., and Ghaemi, S. (2018). Robust synchronization of uncertain fractional-order chaotic systems with time-varying delay. *Nonlinear Dynamics, 93*, 1809-1821. 10.1007/s11071-018-4290-2

Na, J. (2013). Adaptive prescribed performance control of nonlinear systems with unknown dead zone. *International Journal of Adaptive Control and Signal Processing, 27*(5), 426-446. 10.1002/acs.2322

Ouakad, H. M., Nayfeh, A. H., Choura, S., and Najar, F. (2015). Nonlinear feedback controller of a microbeam resonator. *Journal of Vibration and Control, 21*(9), 1680-1697. 10.1177/1077546313494112

Pan, Y., Wang, H., Li, X., and Yu, H. (2017). Adaptive command-filtered backstepping control of robot arms with compliant actuators. *IEEE Transactions on Control Systems Technology, 26*(3), 1149-1156. 10.1109/TCST.2017.2695600

Rahmani, M. (2018). MEMS gyroscope control using a novel compound robust control. *ISA transactions, 72*, 37-43. 10.1016/j.isatra.2017.11.009

Rahmani, M. and Rahman, M. H. (2018). A new adaptive fractional sliding mode control of a MEMS gyroscope. *Microsystem Technologies, 25*, 3409-3416.. 10.1007/s00542-018-4212-8

Rahmani, M. and Rahman, M. H. (2019). A novel compound fast fractional integral sliding mode control and adaptive PI control of a MEMS gyroscope. *Microsystem Technologies*, 1-7. 10.1007/s00542-018-4284-5

Sambas, A., Chang, H. L., Dolvis, L. G., Jacques, K., and Vaidyanathan, S. (2019). A new five-dimensional four-wing hyperchaotic system with hidden attractor, its electronic circuit realisation and synchronisation via integral sliding mode control. *International Journal of Modelling Identification and Control, 32*(1), 30-45. 10.1504/IJMIC.2019.10023534

Sambas, A., Mamat, M., Arafa, A. A., Mahmoud, G. M., and Sanjaya, W. S. M. (2019). A new chaotic system with line of equilibria: dynamics, passive control and circuit design. *International Journal of Electrical and Computer Engineering, 9*(4), 2365-2376. 10.11591/ijece.v9i4.pp2336-2345

Sambas, A., Vaidyanathan, S., Mamat, M., and Mohamed, M. A. (2020). Investigation of Chaos Behavior in a New Two-Scroll Chaotic System with Four Unstable Equilibrium Points, its Synchronization via Four Control Methods and Circuit Simulation. *IAENG International Journal of Applied Mathematics, 50*(1), 1-10. http://www.iaeng.org/IJAM/issues_v50/issue_1/IJAM_50_1_03.pdf

Silva-Juarez, A., Rodriguez-Gomez, G., de la Fraga, L. G., Guillen-Fernandez, O., and Tlelo-Cuautle, E. (2019). Optimizing the kaplan–yorke dimension of chaotic oscillators applying de and pso. *Technologies, 7*(2), 38. 10.3390/technologies7020038

Su, Z., Li, Y., and Yang, G. (2020). Dietary Composition Perception Algorithm Using Social Robot Audition for Mandarin Chinese. *IEEE Access*, (99), 8768-8782. 10.1109/ACCESS.2019.2963560

Sun, G. and Ma, Z. (2017). Practical tracking control of linear motor with adaptive fractional order terminal sliding mode control. *IEEE/ASME Transactions on Mechatronics, 22*(6), 2643-2653. 10.1109/TMECH.2017.2766279

Sun, T. and Pan, Y. (2019). Robust adaptive control for prescribed performance tracking of constrained uncertain nonlinear systems. *Journal of the Franklin Institute, 356*(1), 18-30. 10.1016/j.jfranklin.2018.09.005

Tian, D. P., Shen, H. H., and Dai, M. (2014). Improving the Rapidity of Nonlinear Tracking Differentiator via Feedforward. *IEEE Transactions on Industrial Electronics, 61*(7), 3736-3743. 10.1109/TIE.2013.2262754

Tong, S. and Li, Y. (2011). Adaptive fuzzy output feedback tracking backstepping control of strict-feedback nonlinear systems with unknown dead zones. *IEEE Transactions on Fuzzy Systems, 20*(1), 168-180. 10.1109/TFUZZ.2011.2171189

Vaidyanathan, S., Sambas, A., and Mamat, M. (2018). A new chaotic system with axe-shaped equilibrium, its circuit implementation and adaptive synchronization. *Archives of Control Sciences, 28*, 443-462. 10.24425/acs.2018.124711

Xiong, L., Wang, J., Mi, X., and Khan, M. W. (2017). Fractional order sliding mode based direct power control of grid-connected DFIG. *IEEE Transactions on Power Systems, 33*(3), 3087-3096. 10.1109/TPWRS.2017.2761815

Xu, B., Zhang, R., Li, S., He, W., and Shi, Z. (2019). Composite Neural Learning-Based Nonsingular Terminal Sliding Mode Control of MEMS Gyroscopes. *IEEE Transactions on Neural networks and learning systems, 31*(4), 1375-1386. 10.1109/TNNLS.2019.2919931

Yan, W., Hou, S., Fang, Y., and Fei, J. (2016). Robust adaptive nonsingular terminal sliding mode control of MEMS gyroscope using fuzzy-neural-network compensator. *International Journal of Machine Learning and Cybernetics, 8*, 1287-1299. 10.1007/s13042-016-0501-7

Hang, X., Zhang, H., Liu, D., and Kim, Y. (2009). Neural-network-based reinforcement learning controller for nonlinear systems with non-symmetric dead-zone inputs. Paper presented at the 2009 IEEE Symposium on Adaptive Dynamic Programming and Reinforcement Learning, 124-129. 10.1109/ADPRL.2009.4927535

Hazard Maps of Shallow Landslides Associated to Infiltration Processes in the Sapuyes River Basin

Mapas de amenaza por deslizamientos superficiales relacionados con procesos de infiltración en la cuenca del río Sapuyes

Cristhian Alexander Rosales Rodríguez[1]

ABSTRACT

Hazard mapping of shallow landslides associated with infiltration processes at a regional scale was carried out by means of the spatial and temporal distribution of safety factor and its classification, within hazard level ranges, into cells that represent hillside units in Sapuyes river basin, located near the city of Pasto in the Nariño department. Hazard assessment follows the theoretical approaches of the Iverson model, which takes into account the redistribution of underground pore pressures associated with the transient infiltration of the rain and its effects on the time and location of landslides, considering that shallow landslides are associated with periods of rain with a short duration and greater intensity. Results showed that both the pressure heads and the safety factor are valid approximations for hazard analysis at regional scale and allow observing the transient physical process involved in the development of shallow landslides.

Keywords: shallow landslides, deterministic approach, infiltration, hazard map, risk assessment

RESUMEN

La elaboración de mapas de amenaza por deslizamientos superficiales relacionados con procesos de infiltración a escala regional se realizó mediante la distribución espaciotemporal del factor de seguridad y su clasificación en rangos de nivel de amenaza, en celdas que representan unidades de ladera en la cuenca del río Sapuyes, situada cerca de la ciudad de Pasto, en el departamento de Nariño. La evaluación de la amenaza sigue las aproximaciones teóricas del modelo de Iverson, que tiene en cuenta la redistribución de las presiones de poros subterráneas asociadas a la infiltración transitoria de la lluvia y sus efectos en el tiempo y ubicación de deslizamientos, teniendo en cuenta que los deslizamientos superficiales están asociados a periodos de lluvia de corta duración y de mayor intensidad. Los resultados mostraron que tanto las cabezas de presión como el factor de seguridad son aproximaciones válidas para un análisis de amenaza a escala regional y permiten observar el proceso físico transitorio involucrado en el desarrollo de deslizamientos superficiales.

Palabras clave: deslizamientos superficiales, enfoque determinístico, infiltración, mapa de amenaza, evaluación de riesgo

Introduction

Landslides are strongly related to rainfall events as a triggering factor (Chien, Hsu, and Yin, 2015), which mainly cause shallow landslides. Landslide hazard is evaluated as an instrument for territorial planning, decision making, contribution to the state of the art, and a component of risk assessment. It has also been studied under the guidelines of heuristic, probabilistic, statistical and empirical methodological approaches (van Westen, van Asch, and Soeters, 2006). However, a deterministic landslide modeling approach can be more reliable to assess and analyze the physical processes that govern the issue of slope instability, generally associated with changes in the stress state of the soil.

These changes are due, among other factors, to the hydrogeological conditions of the soil, expressed in terms of variations in the position of the water table or changes in pore pressures caused by the intensity of rain precipitation. Thus, events of less intensity (longer duration) are associated with

changes in the position of the water table, which causes deep landslides; and events of greater intensity (shorter duration) are associated with changes in pore pressures, which causes shallow landslides (Ran, Hong, Li, and Gao , 2018; Aristizábal, Martínez, and Vélez, 2010).

Shallow landslides should be assessed considering that the infiltration of the rain is the main triggering factor that generates slope instability, and its study should lead to determine variations in the groundwater regime that generate changes in the safety factor (Iverson, 2000). The Iverson model allows evaluating the redistribution of underground

---

[1]Civil Engineer, Universidad de Nariño, Colombia. M.Sc. Civil Engineer, Pontificia Universidad Javeriana, Colombia. Affiliation: Professor, Universidad Mariana, Colombia. E-mail: cristhianrosalesr@outlook.com

pore pressures associated to the transitory infiltration of the rain and its effects on the time and location of landslides. In addition, the use of geographic information systems (GIS) allows the spatial and temporal distribution of safety factors and their classification to generate hazard maps.

This paper aims to show the guidelines for the generation of hazard maps according to shallow landslides associated with infiltration processes by means of a deterministic approach, using the Iverson model (2000) at a regional scale in the Sapuyes river basin. The data of the study area were obtained from studies carried out by entities such as IGAC, IDEAM, SGC, Corponariño, and they were processed with a GIS. The Iverson model was used to calculate pressure heads and safety factors into cells of 12,5 m, according to the resolution of the Digital Elevation Model (DEM) through an open access software (GRAS GIS). Finally, the safety factor was classified into ranges that allowed visualizing the hazard level.

Materials and methods

Study area

The study area was the Sapuyes River basin in the department of Nariño, located approximately between the geographical coordinates 77°48'20"W - 00°54'16"N and 77°28'30"W-01°07'55"N. It has an approximate area of 515 km² and an average elevation of 3314 meters above sea level. There are 8 municipalities in the region, as well as the main route between Tumaco port and Pasto city. Figure 1 shows the location of the study area at regional and local revels.
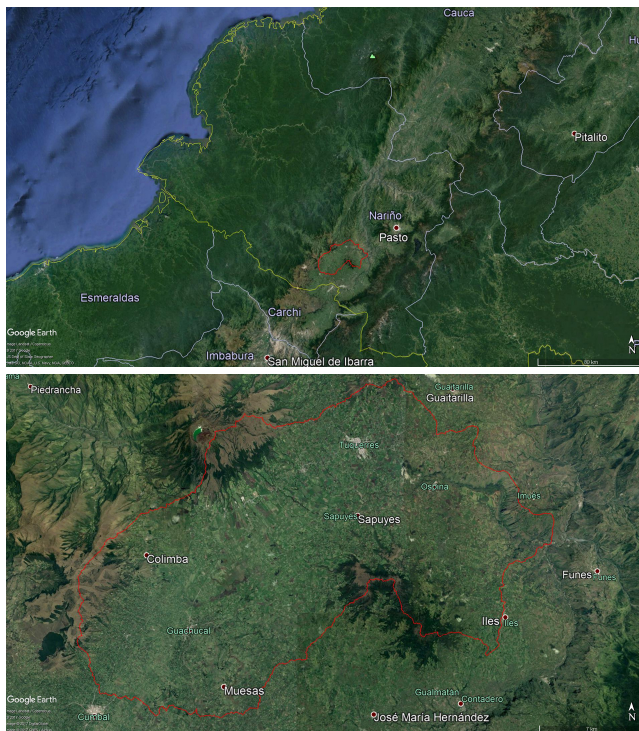
Figure 1. Location of the study area.
Source: Google Earth

Resources

The resources used in the deterministic evaluation to create hazard maps are presented in Table 1.

Table 1. Resources used

Input date	Description	Source
Digital Elevation Model	12,5-meter resolution	GeoSpatial
Rain records	24-hour rainfall	IDEAM
Physical and mechanical properties of soil	Correlations from soil study	IGAC, SGC, Corponariño

Source: Author

Methodology

Background: Scientific literature and research papers were reviewed to identify a physical model which considers variations in the pressure head as a factor that generates instability, with an analytical solution and minimum input parameters.

Model identification: The Iverson model was chosen to perform the hazard modeling. Iverson (2000) uses rational approximations to develop a theoretical model by means of the effective stress principle in an infinite slope stability analysis, while also considering the redistribution of subsurface pore pressures associated with transient rainfall infiltration, in order to evaluate the effects of rain on time and location of landslides.

The analytical solution of the Iverson model to calculate pressure heads (ψ) is shown in Equation 1, whereas Equation 2 is used to calculate safety factors (FS).

$$\psi(Z, t \leq T) = \left\{ \beta \left(1 - \frac{d}{Z}\right) + \frac{I_Z}{K_Z} [R(t^*)] \right\} * Z \qquad (1)$$

$$FS = \frac{\tan\varphi}{\tan\alpha} + \frac{c - \psi(Z,t)\gamma_w \tan\varphi}{\gamma_s Z \sin\alpha \cos\alpha} \qquad (2)$$

where d is the water table depth measured normal to the ground surface, Z is the soil depth, I_Z is the rainfall intensity, K_Z is the soil hydraulic conductivity, φ is the soil friction angle, α is the slope angle, c is soil cohesion, γ_w is the unit weight of groundwater, and γ_s is the soil unit weight.

Treatment of input data: The parameters of the Iverson model were grouped into conditioning and triggering factors. Among the conditioning factors are the properties of the slope and the soil, while the triggering factor is rainfall intensity.

The DEM obtained from satellite images was processed to obtain and make correlations between the hillside slope and the stratum soil thickness . From IGAC information, the physical properties of the soil such as hydraulic conductivity and diffusivity, and unit weight were correlated, as well as mechanical properties such as cohesion and internal friction angle.

The rainfall data were processed to obtain equations of intensity $i = C_0 * T_r^{C_1} * D^{C_2}$ from meteorological stations

in the study area. All the obtained information was spatially distributed using a GIS. Some parameters ($\varphi, c, K_Z, \gamma_s$) were assigned to the soil units of the IGAC, and others were interpolated (Z, I_Z, d).

Modeling: The Iverson model was programmed in GRASS GIS to calculate pressure heads, safety factors, as well as to classify the hazard.

Hazard mapping was carried out by classifying the safety factor based on the values in Table 2.

Table 2. Hazard categories

Level	Safety factor
Low hazard	> 1,5
Medium hazard	1,1 – 1,5
High hazard	< 1,1

Source: Modified from Ávila *et al.* (2015).

Also, an additional classification of the maps was made to show unstable slopes with a factor of safety of less than 1,0.

The flow diagram in Figure 2 explains the guidelines for hazard mapping in general terms.
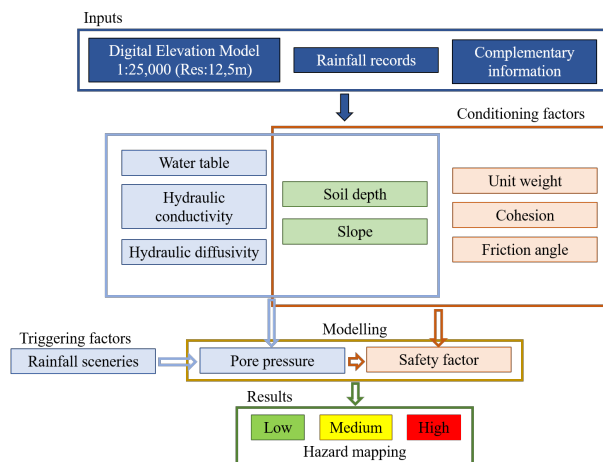
Figure 2. Flow diagram of the hazard mapping methodology.
Source: Author

Results

The hillside slopes map (Figure 3) showed an average slope of 12°; 51% of the slopes have values between 0° and 10°, 31% between 10° and 20°, 12% between 20° and 30°, and 6% greater than 30°.

Ten soil units were identified (Figure 4), and physical and mechanical properties were assigned based on the soil study of the department of Nariño (IGAC, 2004).

For each meteorological station (Figure 5), a time series was generated, an approximated extreme values (Gumbel) probability distribution function was made, and a multiple linear correlation was performed to obtain the intensity parameters (C_0, C_1, C_2).
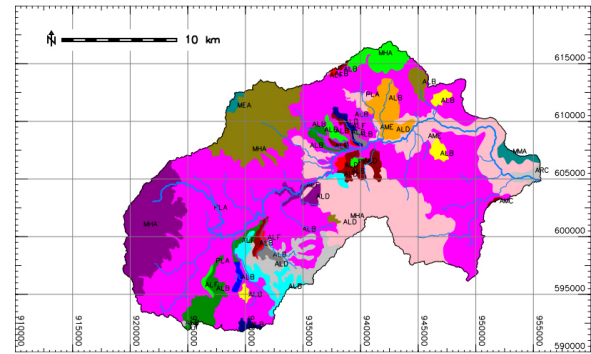
Figure 3. Hillside slopes map
Source: Author
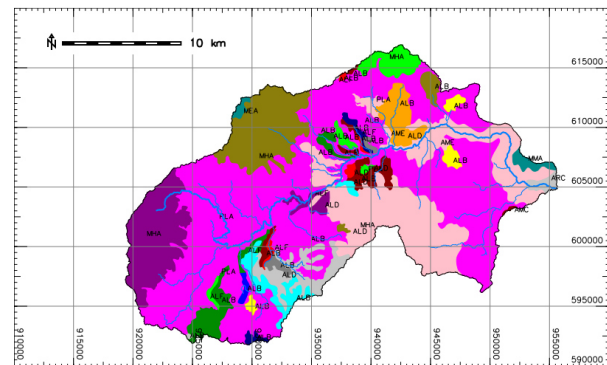
Figure 4. Soil map of the department of Nariño.
Source: Author
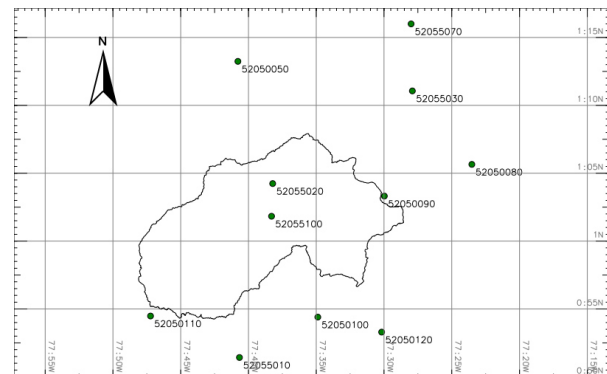
Figure 5. Geographical location of the meteorological stations in the study area.
Source: Author

Figure 6 shows a rain intensity map and isohyets generated for a 30-minute rainfall and a return period of 2,33 years. Likewise, intensity maps for return periods of 2,33, 20, and 100 years were generated, a s well as rainfall durations of 30, 60, and 120 minutes.
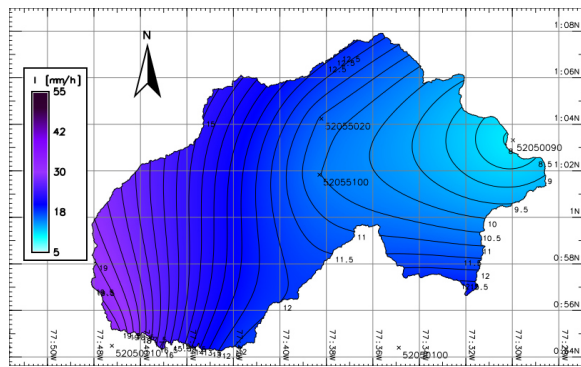
Figure 6. Rain intensity map.
Source: Author

Pressure head

Pressure head changes, as a function of the depth and evaluation time in an individual cell (Figure 7), show the quick response of the pressure head in a depth equal to the soil stratum depth. This can be observed in the spatial distribution map (Figure 8). The pressure head evaluated at the depth of the soil layer does not strictly represent the most critical condition, that is, the highest pressure head.
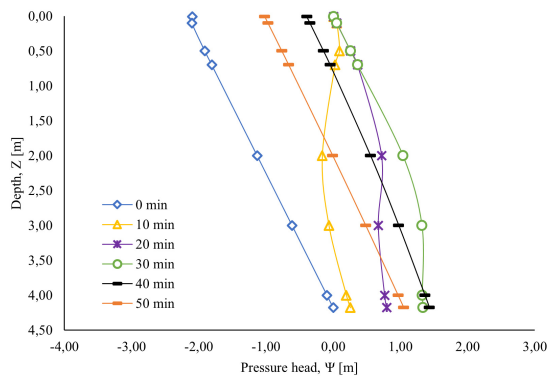
Figure 7. Response of the pressure head in a single cell.
Source: Author

Both the spatial distribution of the pressure head (Figure 8) and the pressure head in individual cells (Figure 9) with different parameters, show the maximum condition of the pressure head around at $t = 30$ min, when the rain has already ended. In addition, although thinner soils develop smaller pressure heads than thicker soils, hydraulic diffusivity can generate changes in the pressure head for soils of equal thickness.

Figure 10a shows the maximum sustainable pressure head with a water table located at a depth of 2,0 m, which, at a time $t > 0$ min, cannot exceed the hydrostatic pressure in any case. Aditionally, Figure 10b shows heads of pressure greater than those observed when the water table is located at a 5,0 m depth (Figure 8). It indicates that the position of the shallow water table generates a pressure head greater than at a deeper water level.
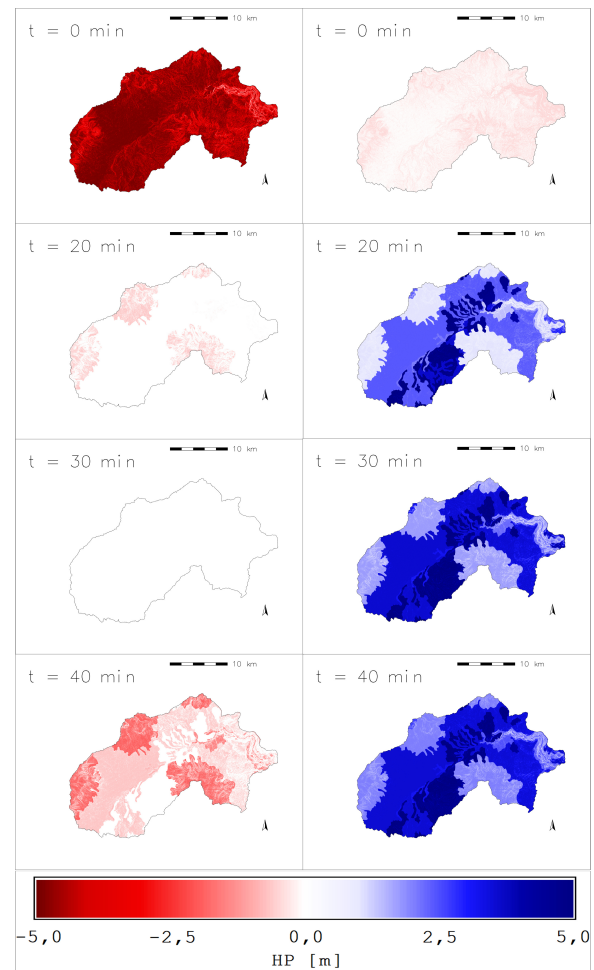
Figure 8. Maps of the spatial and temporal distribution of the pressure head: Left) on the surface, Right) at the depth of the soil layer.
Source: Author
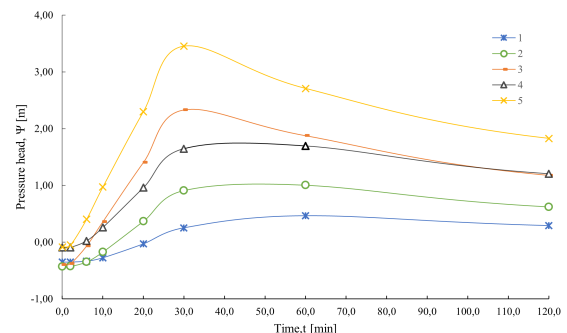
Figure 9. Temporal changes of head of pressure on individual slopes for a rain of 30 minutes in 5 individual slopes.
Source: Author

Pressure head variations at different evaluation depths were evinced when the water level was located at the same depth of the soil stratum. It could also be observed that the pressure head is equal to the hydrostatic pressure at the surface of the soil layer at the end of the rain ($t = 30$ min) and at the depth of the soil layer at the beginning of the rain ($t = 0$ min). Negative pressure heads at $t = 0$ min indicate suction in the

soil, while positive pressure heads are developed at $t > 0$ min. This tendency is more evident when the pressure head is evaluated on individual slopes (Figure 11). It is also seen that, in some slopes, the response of the pressure head is associated to the hydraulic diffusivity of the soil. In other words, soils with lower hydraulic diffusivity may have lower pressure heads (Figure 11, point 4).
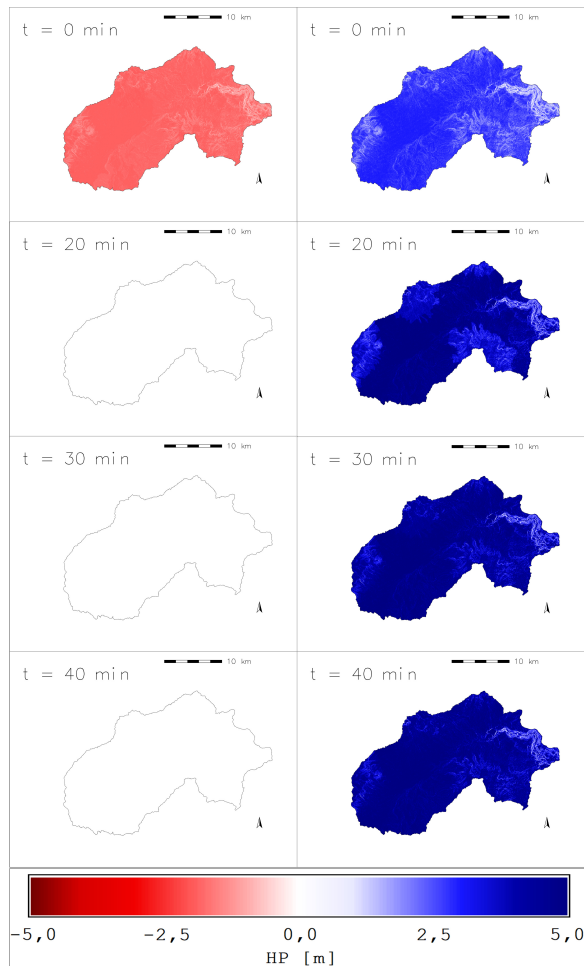
Figure 10. Maps of the spatial and temporal distribution of pressure head with water table located at 2 m depth: Left) on the surface, Right) at the depth of the soil layer.
Source: Author

Figure 11. Response of the pressure head on individual slopes at the beginning (left) and at the end (right) of the rain.
Source: Author
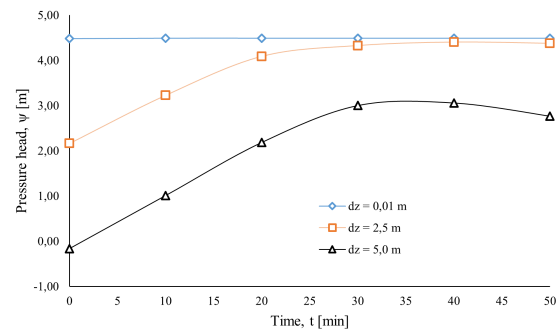
Figure 12. Changes of the pressure head as a function of the depth of the water table.
Source: Author

Figure 12 shows the changes in the average value of the pressure head at the same depth of the soil stratum for different positions of the water table. In general, the pressure head is greater when the position of the water table is superficial, and lower when the position of the water table is located at a greater depth. In addition, the response of the pressure head is greater when the water table is deeper.

Once the rain has finished, the response of the pressure head decreases in an approximately parallel way (Figure 13). In addition, in soils with low hydraulic conductivity, the ratio $I_Z/K_Z > 1,0$ generates an equal pressure head for different rain durations (different intensity), since Equation 1 is only conditioned in this case by the response function $R(t^*)$. In the same way, it was identified that, in soils of low hydraulic

conductivity, increases in rainfall intensity with the return period do not generate changes in the pressure head.
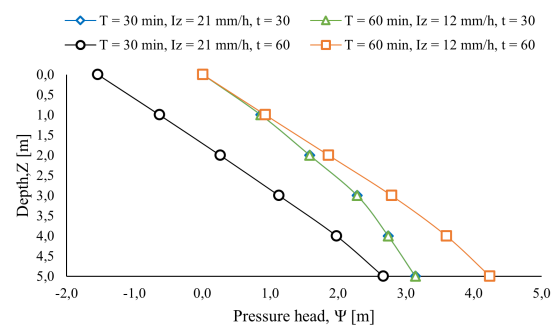
Figure 13. Changes in pressure head for rainfall of different intensity.
Source: Author

When the ratio $\frac{I_Z}{K_Z} = 1,0$ (low permeable soils and high rainfall intensity), the response of the pressure head is equal for rains of any duration until the moment the rain ends. Furthermore, when the ratio $I_Z/K_Z < 1,0$, the response of the pressure head is different during and after the rain (Figure 14).

In addition, the time for the pressure head to return to its initial condition tends to be greater for longer duration rains, i.e. it depends on the duration of the rain (i.e. for a 30-minute

rainfall the estimated time for the pressure head to return to its initial condition is 100 000 minutes (70 days) at any depth of evaluation) (Figure 15).
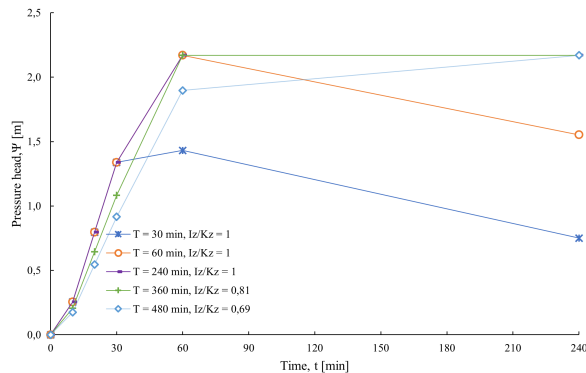
Figure 14. Response of the pressure head of an individual slope for rains of different duration.
Source: Author
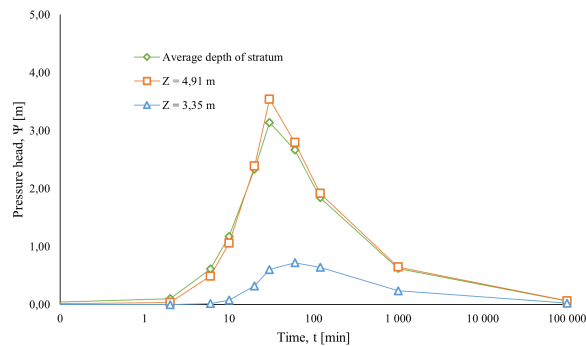
Figure 15. Recovery of the pressure head as a function of time.
Source: Author

Factor of safety

Figure 16 shows that FS changes for different rain evaluation times, and smaller FS values can be identified when $t \sim T$ (30 min). Increases in FS evaluated at $t > T$ are presented by the reduction of ψ at $t > T$ (Figures 8 and 10).

Although the safety factor can be recovered and returned to its initial condition over time (Figure 17, line 4) like the recovery of the pressure head, the same analogy should not be made once the slope has reached failure (Figure 17, lines 1 and 3), and the analysis is performed until the time when $FS \leq 1,0$. Therefore, a suitable way to interpret the variations of FS as a function of t is to analyze until the moment in which the minimum value of FS is reached, considering that this moment is close to the duration of the rain.

Due to the fact that minimum FS values do not occur at the same time on all slopes, since some may fail at different times, Figure 18 shows the minimum FS value for each slope, found from the evaluation of FS at different times. Figure 19 shows the FS decrease until an instant $t \sim T$. Additionally, it

can be observed that the safety factor is recovered after the rain has finished. In this sense, the FS value corresponds to the minimum FS values evaluated at $t = 0, 10, 30, 40, 60$ min.
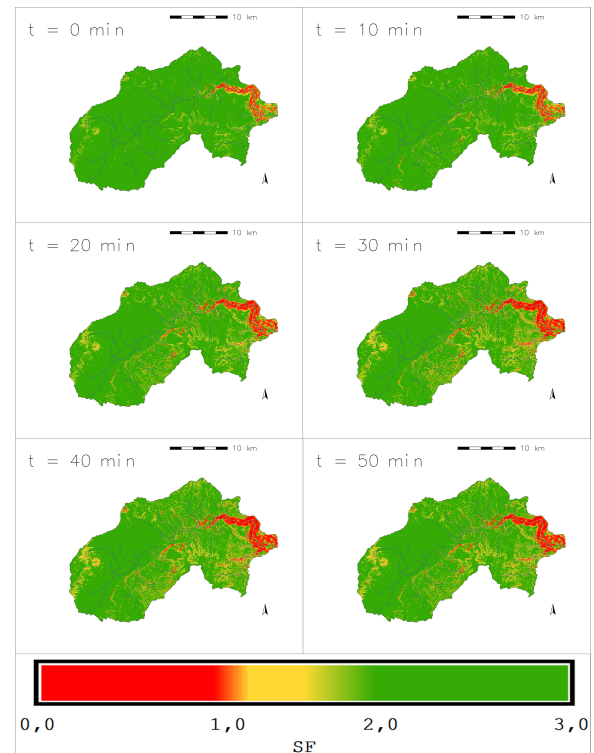
Figure 16. Spatial distribution of the safety factor for a 30-minute rainfall.
Source: Author
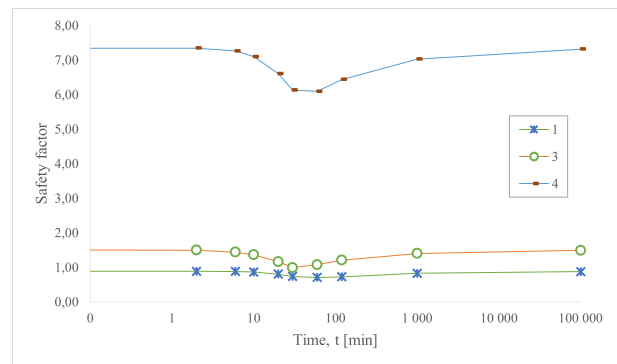
Figure 17. Recovery of the safety factor as a function of time.
Source: Author

In Figure 20, variations in the average FS values associated with the initial position of the water table (d_Z) can be observed. Lower values of FS occur when d_Z is more superficial, and there are greater values when d_Z is deeper. On the other hand, a trend of minimum FS values is observed in moments close to T. In addition, the FS variations over time remain almost constant for surface values of d_Z and decrease more quickly for deeper values of d_Z.
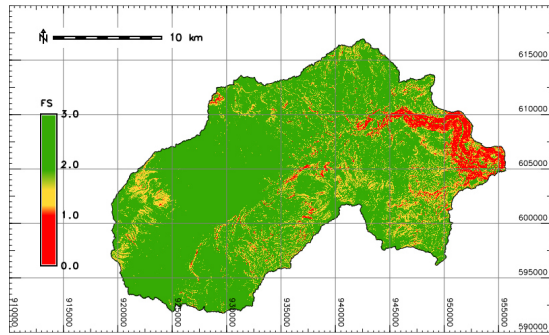
Figure 18. Map with the minimum safety factor value for all evaluation times.
Source: Author
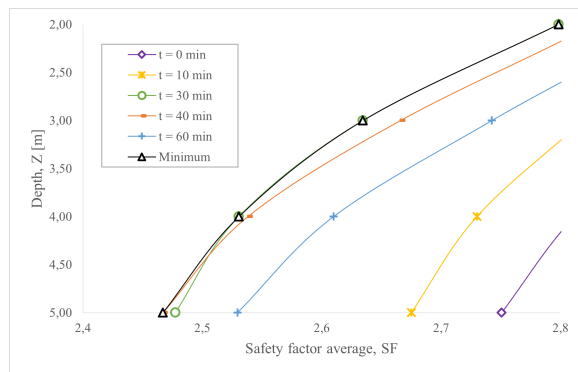
Figure 19. Changes in the safety factor according to the depth and time of evaluation.
Source: Author
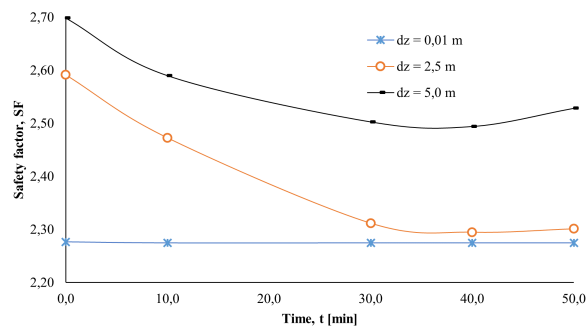
Figure 20. Changes in the factor of safety with variations in the position of the water table.
Source: Author

Thus, it can be inferred that the response in slope stability is directly associated with the location of the water table in the slope. Therefore, in slopes with a shallow water table position, the safety factor remains almost constant during and after the rainfall duration. An FS value that does not change over time means that the slope always remains in its original condition (stability or instability).

Hazard mapping

The mapping of hazard as a time function is presented for the instant in which the safety factor is at its lowest in each slope

(cell) at all evaluation times (Figure 18). Figure 21 shows the hazard map by FS classification according to the criteria of Table 2; the scenario considers the minimum FS value for all the evaluation times.
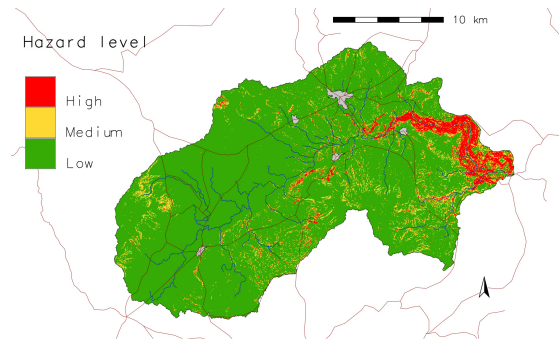
Figure 21. Hazard map for a 30-minute rain.
Source: Author

Discussion

The spatial distribution maps of $\psi(Z, t)$ show the response of the pressure head for high intensity rain events (I_Z) and low hydraulic conductivity soils (K_Z), *i.e.* $I_Z/K_Z \geq 1$. Furthermore, the maximum pressure head develops very closely to the duration of the rain at times (Figure 14). The above is observed in a similar way by the determination of pressure heads for maximum precipitation events from instrumentation with piezometers (Fannin *et al.*, 2000). The temporary variations of the pressure head, under different ratios I_Z/K_Z determine the stability of the slope, because soils with greater hydraulic conductivity generate more positive pore pressures. In this way, the factor of safety at different depths decreases the lower the value of I_Z/K_Z (Zhang, Zhu, and Zhang, 2020)

Although the pressure head evaluated at the end of rain is less for a higher intensity rain (Figure 13) in soils with an ratio $I_Z/K_Z = 1$, when the ratio $I_Z/K_Z \leq 1$ is obtained higher pressure heads for higher intensity rains (Figure 14) (Zhang *et al.*, 2020). In fact, measurements of pressure heads from instrumentation with piezometers also show this behavior (Fannin, Jaakkola, Wilkinson, and Hetherington, 2000). This is related to the generation of positive pore pressures and the occurrence of surface landslides associated with periods of high intensity rainfall (Sidle and Ochiai, 2006; Aristizábal, Martínez, and Vélez, 2010; Cho, 2009). Likewise, the pressure head variation rate in terms of depth is at times equal to or greater than at the end of rain (Figure 14), that is, pore pressure tends to dissipate steadily throughout the range of depth. According to Ivanov *et al.* (2020), there is an inverse correlation between I_Z/K_Z and the slope's time of failure, implying that higher intensity rainfalls need less time to cause failure. This is directly related to the development of higher pressure heads, which will cause decrease soil strength and the fall of slopes as well.

The analysis of short-term duration rainfalls with the Iverson model implies that the hydraulic diffusivity value applies for

conditions close to soil saturation, while the recovery of the pressure head with time implies a decrease in soil saturation for instants after the end of the rain. Thus, it can be concluded that the recovery time of the pressure head is more associated to hydraulic diffusivity than to the duration of the rain (Figure 14).

Both Figure 15 and Figure 17 indicate that the pressure head and the safety factor tend to return to their initial condition after very long periods of time (70 days). However, the prediction made may not be significant, considering that the Iverson equations are considered for short evaluation periods, as well as the fact that it differs from observations made with piezometers (Fannin *et al.*, 2000), in which it is observed that pressure heads return to their initial condition after much shorter times.

The spatial distribution of the safety factor (Figure 16) is closely related with pore pressure variations. In addition, these variations in the FS are observed both in the analysis of an individual slope and in the spatial distribution. In fact, the spatial distribution of the safety factor and its relationship with pore pressures can be studied through the application of deterministic models that perform a physical analysis of the problem (Kim, Im, Lee, Hong, and Cha, 2010; Baum, Godt, and Savage, 2010).

Pradel and Raad (1993) stated that surface failures are more likely to occur in sandy or gravel soils (high hydraulic conductivity), but there is a higher potential for failure in silt and clays (low hydraulic conductivity) in natural slopes, *i.e.* the influence of hydraulic conductivity on slope stability is not clear. Similarly, downscale tests in sands have showed that hydraulic conductivity (K_z) is a parameter that governs soil stability, considering that soils with a higher void ratio allow a quicker redistribution of rainfall water (Ivanov *et al.*, 2020). However, taking into account that FS variations depend on variations in $\psi(Z, t)$ and, in turn, variations in $\psi(Z, t)$ depend on the hydraulic conductivity of the soil (K_{sat}) and rainfall intensity (I_Z), it is possible that large variations in $\psi(Z, t)$ are not observed for higher rainfall intensities, since the water response is conditioned by the I_Z/K_Z ratio.

Some authors refer to shallow landslides as those in which the sliding mass has a thickness between 2,0 and 3,0 meters (Baum, Godt, and Savage, 2010; Anderson and Sitar, 1995), while others refer to a depth less than 2,0 meters to consider a surface-type slip (Pradel and Raad 1993; Iida, 1999; Schilirò, Montrasio, and Scarascia Mugnozza, 2016; Aristizábal *et al.*, 2010; Chae, Lee, Park, and Choi, 2015). Although it is not easy to define a single criterion for the classification of shallow landslides, the simulations of the safety factor allowed observing that most of the slopes failed for an evaluation depth of less than 3,0 meters under the considerations of this case study.

Regarding the results, physics-based deterministic methods that explain the variations in the groundwater regime (Kim *et al.*, 2010; Montrasio and Valentino, 2008) are similar to those obtained through the methodological application made in this investigation for obtaining hazard maps. The current approach allows to consider the dynamics of the hydrologic

events from real rainfall intensity values (I_z) and temporal variations, which play an important role for the development of instability (Ivanov *et al.*, 2020)

Some deterministic approaches and methodologies for the evaluation of landslide hazards (Avila *et al.*, 2015; Westen and Terlien, 1996) calculate the FS by assigning a water table height that is related to the amount of rainfall that precipitates for different periods of rain or return periods. Although these approaches have valid physical assumptions, they are not the most adequate for the evaluation of the physical process that conditions the instability of the slope. Additionally, the application of the models in question does not allow evaluating the temporal variations of the safety factor.

Furthermore, the proposed approach allows evaluating infinite scenarios based on the variables of the Iverson model (2000), mainly as a function of rainy weather, that is, during the entire duration of the storm, or even after it.

Conclusions

The possibility of performing temporary analyses of variations in the pressure head and the safety factor in slopes was identified as one of the main advantages of the methodological approach used in this study. Compared to other methodologies, temporality is a relevant factor when you want to deepen the knowledge of the process that leads to slope instability in periods of time that are approximately equal to the duration of the precipitation event.

It was determined that pore pressure modeling is very sensitive to variations in the initial location of the water table. Therefore, in the subsoil exploration stage, an additional effort must be made to determine the depths of the water table and make an adequate spatial distribution of the data.

Based on the results of the safety factor for different soil thicknesses, it was determined that a good criterion for the classification of surface landslides ($\sim 3,0$ m) results from the application of deterministic models for FS spatial distribution.

The hazard assessment of landslides associated with changes in pore pressures indicates potentially unstable areas in the Sapuyes River basin. Hazard mapping did not include the validation of the Iverson model, which could be carried out based on landslide inventories, with databases such as the Mass Movements Information System (SIMMA). The validation of the model implies a sensitivity analysis to determine the rate of true positives (Nguyen, Lee, and Kim, 2019).

References

Anderson, S. A., and Sitar, N. (1995). Analysis of Rainfall-Induced Debris Flows. *Journal of Geotechnical Engineering, 121*(7), 544-552. 10.1061/(ASCE)0733-9410(1995)121:7(544)

Aristizábal, E., Martínez, H., and Vélez, J. I. (2010). Una revisión sobre el estudio de movimientos en masa detonados por lluvias. *Revista de la Academia Colombiana de Ciencias Exactas, físicas y Naturales, 34*(131), 209-227. https://raccefyn.co/index.php/raccefyn/issue/view/181/169

Avila, G. E., Cubillos, C. E., Granados, A. E., Medina, E., Rodríguez, É. A., Rodríguez, C. E., and Ruiz, G. L. (2015). *Guía Metodológica: Para Estudios de Amenaza, Vulnerabilidad y Riesgo por Movimientos en Masa*. Bogotá: Universidad Nacional de Colombia, Servicio Geológico Colombiano.

Avila Álvarez, G. E., Cubillos Peña, C. E., Granados Becerra, A. E., Medina Bello, E., Rodríguez Castiblanco, É. A., Rodríguez Pineda, C. E., and Ruiz Peña, G. L. (2015). *Guía Metodológica: Para Estudios de Amenaza, Vulnerabilidad y Riesgo por Movimientos en Masa*. Bogotá: Universidad Nacional de Colombia, Servicio Geológico Colombiano.

Baum, R. L., Godt, J. W., and Savage, W. Z. (2010). Estimating the timing and location of shallow rainfall-induced landslides using a model for transient, unsaturated infiltration. *Journal of Geophysical Research-Earth Surface, 115*. 10.1029/2009jf001321

Chae, B. G., Lee, J. H., Park, H. J., and Choi, J. (2015). A method for predicting the factor of safety of an infinite slope based on the depth ratio of the wetting front induced by rainfall infiltration. *Natural Hazards and Earth System Sciences, 15*(8), 1835-1849. 10.5194/nhess-15-1835-2015

Chien, L. K., Hsu, C. F., and Yin, L. C. (2015). Warning Model for Shallow Landslides Induced by Extreme Rainfall. *Water, 7*(8), 4362-4384. 10.3390/w7084362

Cho, S. E. (2009). Infiltration analysis to evaluate the surficial stability of two-layered slopes considering rainfall characteristics. *Engineering Geology, 105*(1-2), 32-43. 10.1016/j.enggeo.2008.12.007

Fannin, R. J., Jaakkola, J., Wilkinson, J. M. T., and Hetherington, E. D. (2000). Hydrologic response of soils to precipitation at Carnation Creek, British Columbia, Canada. *Water Resources Research, 36*(6), 1481-1494. 10.1029/2000WR900027

IGAC (2004). *Estudio general de suelos y zonificación de tierras Departamento de Nariño*. Bogotá: Instituto Geográfico Agustín Codazzi.

Iida, T. (1999). A stochastic hydro-geomorphological model for shallow landsliding due to rainstorm. *CATENA, 34*(3), 293-313. 10.1016/S0341-8162(98)00093-9

Ivanov, V., Arosio, D., Tresoldi, G., Hojat, A., Zanzi, L., Papini, M., and Longoni, L. (2020). Investigation on the Role of Water for the Stability of Shallow Landslides–Insights from Experimental Tests. *Water, 12*(4), 1203. 10.3390/w12041203

Iverson, R. M. (2000). Landslide triggering by rain infiltration. *Water Resources Research, 36*(7), 1897-1910.

Kim, D., Im, S., Lee, S. H., Hong, Y., and Cha, K.-S. (2010). Predicting the rainfall-triggered landslides in a forested mountain region using TRIGRS model. *Journal of Mountain Science, 7*(1), 83-91. 10.1007/s11629-010-1072-9

Montrasio, L. and Valentino, R. (2008). A model for triggering mechanisms of shallow landslides. *Natural Hazards and Earth System Sciences, 8*(5), 1149-1159. 10.5194/nhess-8-1149-2008

Nguyen, B.-Q.-V., Lee, S.-R., and Kim, Y.-T. (2020). Spatial probability assessment of landslide considering increases in pore-water pressure during rainfall and earthquakes: Case studies at Atsuma and Mt. Umyeon. *CATENA, 187*, 104317. 10.1016/j.catena.2019.104317

Pradel, D. and Raad, G. (1993). Effect of permeability on surficial stability of homogeneous slopes. *Journal of Geotechnical Engineering, 30*(5), 17. 10.1061/(ASCE)0733-9410(1993)119:2(315)

Ran, Q., Hong, Y., Li, W., and Gao, J. (2018). A modelling study of rainfall-induced shallow landslide mechanisms under different rainfall characteristics. *Journal of Hydrology, 563*, 790–801. 10.1016/j.jhydrol.2018.06.040

Schilirò, L., Montrasio, L., and Scarascia Mugnozza, G. (2016). Prediction of shallow landslide occurrence: Validation of a physically-based approach through a real case study. *Science of The Total Environment, 569–570*, 134-144. 10.1016/j.scitotenv.2016.06.124

Sidle, R. C. and Ochiai, H. (2006). Characteristics of Various Types of Landslides. In Ochiai, H. (Ed-) *Landslides: Processes, Prediction, and Land Use* (pp. 23-39). Washington D.C.: American Geophysical Union.

van Westen, C. J., van Asch, T. W. J., and Soeters, R. (2006). Landslide hazard and risk zonation–why is it still so difficult? *Bulletin of Engineering Geology and the Environment, 65*(2), 167-184. 10.1007/s10064-005-0023-0

van Westen, C. J. and Terlien, M. J. T. (1996). An approach towards deterministic landslide hazard analysis in GIS. A case study from Manizales (Colombia). *Earth Surface Processes and Landforms, 21*(9), 853-868. 10.1002/(SICI)1096-9837(199609)21:9<853::AID-ESP676>3.0.CO;2-C

Zhang, J., Zhu, D., and Zhang, S. (2020). Shallow slope stability evolution during rainwater infiltration considering soil cracking state. *Computers and Geotechnics, 117*, 103285. 10.1016/j.compgeo.2019.103285

Analysis of the Efficiency of Traffic Lights Turning Red in Case of Exceeding Speed Limit

Análisis de la eficacia de los semáforos que se ponen rojo en caso de exceder el límite de velocidad

Heriberto Pérez-Acebo [1], Xabier Otxoa-Muñoz[2], Mikel Marquina-Llaguno[3], and Hernán Gonzalo-Orden[4]

ABSTRACT

Due to the presence of various traffic calming measures (TCM) and traffic lights in urban areas, the speed of vehicles is maintained low. Nevertheless, a problem arises in the frontier between urban and non-urban areas because drivers must adapt their speed and behavior to new conditions. This risk becomes even greater in rural roads that penetrate small villages without a bypass and with a short urban segment, since drivers do not normally speed down in these segments. Various measures can be installed, but traffic lights that turn red if the speed limit is exceeded is not usually considered as a TCM in the literature. Therefore, this paper aims to analyze the efficiency of traffic lights turning red in case of exceeding speed limit. The village of Ábalos in Spain was selected for this research, with an urban area of 630 m and this type of traffic lights in both directions. Results showed that drivers do not respect the speed limit - and hence, the red light - when they are placed separately. However, if they are placed next to a crosswalk, their effect is increased. Consequently, it is recommended to place these traffic lights with a crosswalk to reinforce the efficiency of both TCMs.

Keywords: traffic calming measure, road safety, urban area, pedestrian, traffic lights, speed limit, crosswalk

RESUMEN

Debido a la presencia de varias medidas de calmado de tráfico (MCT) y semáforos en zonas urbanas, la velocidad de los vehículos se mantiene baja. No obstante, un problema aparece en la frontera entre áreas urbanas y no urbanas porque los conductores deben adaptar su velocidad y comportamiento a nuevas condiciones. Este riesgo se vuelve incluso mayor en las carreteras interurbanas que penetran en pequeñas poblaciones sin circunvalación y con un corto tramo urbano, pues normalmente los conductores no reducen su velocidad en estos tramos. Varias medidas pueden ser instaladas, pero los semáforos que se ponen rojos si se sobrepasa el límite de velocidad no suelen considerarse como MCT en la literatura. Por lo tanto, el objetivo de este artículo es analizar la eficacia de los semáforos que se ponen rojos en caso de exceder el límite de velocidad. La población de Abalos en España fue seleccionada para esta investigación, con un área urbana de 630 m y con este tipo de semáforos en ambas direcciones. Los resultados muestran que los conductores no respetan el límite de velocidad - y por tanto, el semáforo en rojo - cuando son colocados por separado. Sin embargo, si son colocados junto a un paso de peatones, se aumenta su efecto. En consecuencia, se recomienda disponer este tipo de semáforos junto con un paso de peatones para reforzar la eficacia de ambas MCT.

Palabras clave: medida de calmado de tráfico, seguridad vial, área urbana, peatón, semáforo, límite de velocidad, paso de peatones

Introduction

Despite the important decrease registered in the total number of fatalities in road traffic in developed countries during the last years, road safety is still a major problem around the world, and it has become the leading cause of premature death (Studer *et al.*, 2018; Ptak, 2019; Llopis-Castelló and Findley, 2019; Shah and Ahmad, 2019). To give some figures, in the European Union (EU-28), the number of fatalities in collisions decreased from 57 006 to 25 767 between 2000 and 2016 (54,7%) (EUROSTAT, 2018). In the United States, a rate of 35 000 people dead in crashes per year is registered (FHWA, 2018).

In Spain, even a higher decrease was observed in the same period (2000-2016), 68,7% (from 5 776 to 1 810) (EUROSTAT, 2018). In 2018, 102 299 accidents with injured people were

[1] Civil Engineer and Master of Science, Universidad de Burgos, Spain. Doctor in Mechanical Engineering, Universidad del País Vasco UPV/EHU, Spain. Affiliatin: Assistant Professor, Universidad del País Vasco UPV/EHU, Spain.
E-mail: heriberto.perez@ehu.eus
[2] Civil Engineer, Universidad del País Vasco UPV/EHU, Spain. Master of Science, Universidad Politécnica de Madrid, Spain. Affiliation: Civil Engineer at GIRDER Ingenieros, S.L.P., Spain. E-mail: xotxoa@girder.es
[3] Undergraduate, Universidad del País Vasco UPV/EHU, Spain.
E-mail: mmarquina003@ikasle.ehu.eus
[4] Civil Engineer and Master of Science, Universidad de Cantabria, Spain. Doctor in Engineering, Universidad de Burgos, Spain. Affiliation: Professor, Universidad de Burgos, Spain. E-mail: hgonzalo@ubu.es

registered, with a total number of fatalities of 1 806 people, 1 317 of which died in an interurban road, as well as 489 in urban roads. In 2010, there were 122 823 crashes with people injured, and 2 478 people died (a decrease of 27,1%). However, the decrease in interurban roads, 31,7 % (from 1 928 to 1 317), was higher than in urban roads, which was only 11% (from 550 to 489) (DGT, 2019). Consequently, although an important reduction was obtained in interurban roads, similar figures were not achieved in urban areas.

With the aim of improving road safety in urban areas, in 2010, the European Commission published policy orientations and indicated that vulnerable road users (motorcycle riders, mopeds, cyclist, and pedestrians) must be specially protected (EC, 2010). For example, from the 489 people that died in urban accidents in 2018, 149 were pedestrians (30,4%) (DGT, 2019). To reduce these figures, traffic calming measures (TCM) are being displayed in urban roads. They may be defined as "the combination of mainly physical measures that reduce the negative effect of motor vehicle use, alter driver behavior and improve conditions for non-motorized street users" (Lockwood, 1997, p. 2). The main objective of the TCMs is to reduce vehicle speed and volumes in an area, since they were determined to be vital factors to reduce the probability of death for pedestrians involved in a crash (Table 1) (TRB, 2010; Tefft, 2011).

Table 1. Chance of pedestrian death if hit by a motor vehicle

Speed of collision (km/h)	80	65	50	32
Chance of pedestrian death (%)	100	80	40	5

Source: TRB (2010).

Usual classifications for TCMs include four categories: vertical deflections (speed humps, speed cushions, rumble strip, raised intersection, raised crosswalk, etc.); horizontal deflections (chicane, raised median island, gateway, curb-extension, etc.); physical obstructions (raised median through intersections, semi and diagonal diverter, right-in and right-out island, etc.); and signs and pavement markings (Kveladze and Agerholm, 2018; Gonzalo-Orden, Rojo, Pérez-Acebo and Linares, 2016; Pérez-Sansalvador, Lakouari, García-Díaz, and Pomares Hernández, 2020; Torres, Cloutier, Bergeron, and St-Denis, 2019; Ziolkowski, 2018). In urban areas, the succession of traffic calming measures and traffic lights maintains the speed of vehicles low. However, a problem appears in the transition from an interurban area to an urban area (Gonzalo-Orden, Pérez-Acebo, Linares-Unamunzaga, and Rojo Arce, 2018). This problem becomes even greater when interurban road penetrates in the urban area of a small village that is not bypassed. If the road segment inside the urban area is short, drivers may not reduce the speed appropriately because the village is not their final destination, and they circulate at high speeds, increasing the probability of pedestrian deaths (Table 1). To reduce the speed of vehicles, traffic calming measures are displayed before the unbypassed village. Various TCMs are placed at the border between non-urban and urban areas: raised crosswalks, sign with speed limits, panels displaying vehicle speed, radars, etc. Their efficiency has been analyzed in the literature

(Daniels *et al.*, 2019; Gonzalo-Orden *et al.*, 2018). Under these circumstances, a usual measure in Spain consists of traffic lights that turn red if the speed limit is exceeded. These lights detect an approaching vehicle, and if its speed is higher than the limit, they try to stop it. Hence, the risk of accidents of pedestrians trying to cross the main road is reduced. Scarce research can be found about this type of TCM. Normally, papers focus on traffic offenses involving red lights and on the effectiveness of red light cameras on accidents (Baratian-Ghorghi, Zhou, and Zech, 2016; Llau, Ahmed, Khan, Cevallos, and Pekovic, 2015; Jensupakarn and Kanitpong, 2018), but the efficiency of the traffic lights used for this research is not analyzed as a TCM in the literature.

Consequently, the aim of this paper is to analyze the efficiency of said TCMs in rural roads that penetrate in villages with a short urban segment. For this purpose, the LR-124 road in Ábalos, in the region of La Rioja (Spain) was selected. This type of traffic lights is placed in both directions at the entrance of the village. After them, two crossing walks are located for pedestrians to communicate both parts of the village. Speed is controlled in the traffic lights and the crosswalk to know the memory effect of the TCM in the subsequent crosswalks.

Methodology and case study

The LR-124 road in the Autonomous Region of La Rioja was selected for taking field measures in order to conduct an analysis of the efficiency of traffic lights turning red if the speed limit is exceeded. The road belongs to the regional government of La Rioja, and it is included in the Regional Basic Network, the most important road network managed by the regional government. Above this category, there is only the RCE (Red de Carreteras del Estado, the State Road Network), which is the road network that belongs to the Spanish Government, under the Ministry of Transportation and Urban Mobility, and includes freeways and national roads (Pérez-Acebo, 2018). The LR-124 road goes from Logroño (the capital of La Rioja) to Briñas, but it is divided in 3 segments, since it also goes through the province of Alava, with the name of A-124, and those segments belong to the Regional Government of Alava (Pérez-Acebo, 2018). In the central segment, between the two borders with the province of Alava, the road goes from Ábalos to San Vicente de la Sonsierra, with a length of 8,6 km, and it goes through the village of Ábalos.

In 2011, this segment of the LR-124 had an Annual Average Daily Traffic (AADT) of 2 043 vehicles/day with a percentage of heavy traffic of 7,42% (MFOM, 2012). In Spain, a vehicle is considered to be heavy when its total weight is over 3 500 kg (MFOM, 2003; Pérez-Acebo, Linares-Unamunzaga, and Gonzalo-Orden, 2020). The last available data showed an AADT of 2 390 and 2 457 vehicles in 2015 and 2016, respectively, with 8,7% of heavy vehicles in both years (MFOM, 2016, 2017).

The LR-124 road crosses the village of Ábalos, in a segment of approximately 630 m, which divides the urban area in two parts, one of them being quite bigger than the other

(Figure 1). However, the only ways to go from one part to the other are the existing two crosswalks. Pedestrians must cross this interurban road with a significant amount of traffic. With the aim of reducing the speed of vehicles when going through the village, traffic lights turning red if the speed limit is exceeded were installed in both directions as a TCM. Their location, as well as that of the crosswalks, is shown in Figure 1. In each direction, the sequence of the TCMs is as follows:

- Logroño – Briñas direction (east – west) (Figure 2):

- Point A1: Traffic lights warning about the presence of traffic lights and a sign for a maximum speed of 40 km/h.

- Point A2: A maximum speed sign of 40 km/h and the traffic light turning red if the speed limit is exceeded.

- Point A3: A non-raised crosswalk.

- Point A4: A non-raised crosswalk.

- Briñas – Logroño direction (west – east) (Figure 3):

- Point B1: rumble strips and a maximum speed sign of 50 km/h.

- Point B2, a traffic light warning about the presence of traffic lights and a sign explaining that the next traffic light will turn red if the speed limit (40 km/h) is exceeded.

- Point B3: the traffic light turning red if speed limit is exceeded and a non-raised crosswalk

- Point B4: a non-raised cross walk.
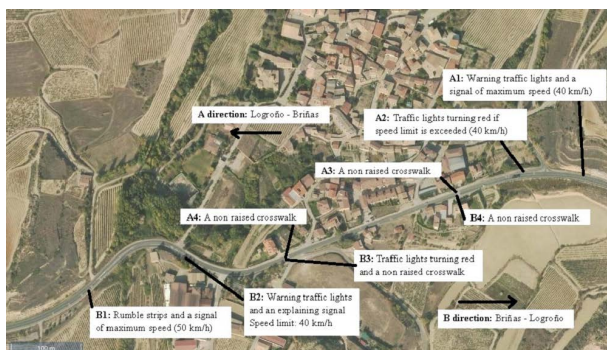
Figure 1. Aerial photo of the village of Ábalos and locations of the traffic calming measures and crosswalks.
Source: Authors

As seen, points A3 and B4 refer to the same crosswalk, and similarly, points A4 and B3.

Measurements were carried out on August 30 and 31, in 2019, in summer, when this kind of village has a higher population, given that a lot of people spend their vacations in these villages, outside the big cities. A fixed radar was placed on the crosswalk with the traffic lights of point B3/A4 for 24 hours, from August 30 at 11:30 a.m. to August 31

at 11:30 a.m. It controlled both directions. Then, the radar was hidden in a car and took measurements in the crosswalk of point A3/B4 for more than 8 hours (from 11:45 a.m. to 8:00 p.m.). Additionally, a gun radar was employed to take measures at the traffic light of point A2 on both days during more than one hour each.

These points were selected because the speed of the vehicles at the crosswalks had to be determined, as they are the place that pedestrians use to cross the road. Hence, these points must be the place where speed must be at its minimum level to reduce the probability of pedestrian deaths related to accidents (TRB, 2010; Tefft, 2011). Additionally, the traffic lights turning red in point A2 were checked to know if they were respected by drivers. If they exceeded the maximum speed of 40 km/h, the traffic light would turn red, and, under these circumstances, they had to stop their vehicles. Consequently, drivers who pass by this section with a speed over 40 km/h, and with a red traffic light, could be fined if the police are present.

Results and discussion

More than 4 300 vehicles were measured in this research. Table 2 presents the average speed of the vehicles, V_m; the percentile 85th of the speed, V_{85}, which is the speed not reached by 85% of vehicles or, in other words, the speed achieved or exceeded by 15% of the vehicles); the maximum speed, V_{max}; and the total number of vehicles controlled. Additionally, the number of vehicles that exceeded the speed limit (40 km/h) and the percentages of vehicles exceeding this limit are shown.

Table 2. Values of selected variables at control points

Direction	Logroño – Briñas			Briñas – Logroño	
Points	A2	A3	A4	B3	B4
V_m (km/h)	50,5	41,9	37,3	30,5	47,5
V_{85} (km/h)	60	51	47	42	58
V_{max} (km/h)	85	74	80	80	93
Total number	261	638	1 329	1 411	751
Vehicles with v > 40 km/h (number)	224	349	488	255	592
Vehicles with v > 40 km/h (%)	85,8	54,7	36,7	18,1	78,8

Source: Authors

As seen, in the Logroño – Briñas direction, the average value of the speed at point A2 was 50,5 km/h, which indicates that approximately the 86% of the vehicles did not respect the speed limit and continued their way even with a red light. Fortunately, in the next point, A3, when a non-raised crosswalk was installed, the average speed was reduced to 41,9 km/h, near the speed limit. Furthermore, the V_{85} was 51 km/h, which indicates that the 54,7% of vehicles did not respect the limit. Finally, in point A4, with the crosswalk and the traffic light in the other direction, both V_m and V_{85} were even more reduced. This shows that drivers were aware of the presence of an urban area, and, in the second crosswalk

they reduced their speed even more. At this point, only 36,7% of the drivers went faster than allowed (Figure 4a).

In the other direction, (Briñas – Logroño) values in point B3 were quite satisfactory, since both V_m and V_{85} were near 40 km/h. Only 18,1% of the drivers did not respect the signs and the red light. In this case, drivers speeded up from point B3 to B4, and the average speed was over the limit. V_{85} also had a value of 58 km/h. Hence, 78,8% of drivers exceeded the speed limit in their second crosswalk (Figure 4b).

Figure 2. Traffic calming measures in direction A (Logroño–Briñas).
Source: Authors

If we compare the values in both traffic lights, the one in point B3 resulted in a greater speed reduction than the one

Figure 3. Traffic calming measures in direction B (Briñas – Logroño).
Source: Authors

in A2. This lower speed was due to the presence of a crosswalk. Drivers might not have respected a red light or a fine, but if there were crosswalks, they would know that a pedestrian might want to cross the carriageway, and, they would unconsciously speed down to have time to stop the vehicle if such pedestrian appeared. This trend was also observed in direction A, since lower speeds were registered in the crosswalks than in the traffic lights. Drivers might not have respected the red light, but they preferred to speed down in the presence of a crosswalk due to the possible presence of pedestrians. Figure 5 shows the cumulated distribution of the registered speeds in each point.
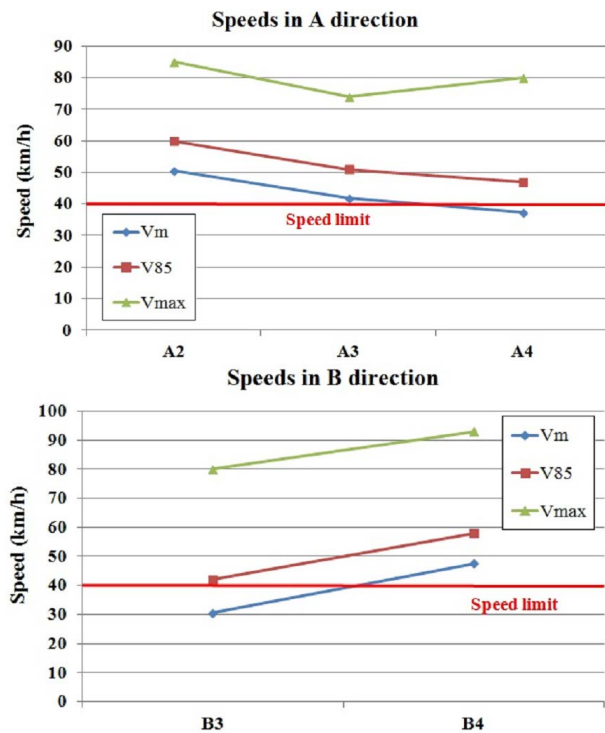
Figure 4. Speeds at each controlled point: a) in direction A, b) in direction B.
Source: Authors
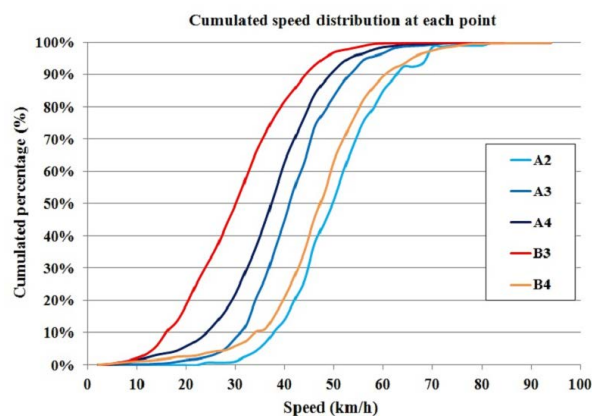
Figure 5. Cumulated distribution of speeds at each point.
Source: Authors

Finally, the speed values registered in point A4/B3 for 24 hours were classified in two periods: day and night, according to the presence of natural light. On August 30 in 2019, the sun set at 8:45 p.m. in Ábalos, it and went up at 07:35 a.m. on August 31. Obtained values for each period are presented in Table 3. The speed distribution in each point during the day and night is shown in Figure 6.

As seen, speeds at night were higher than during the day. Both values of V_m and V_{85} followed this trend. Moreover, the standard deviation at night was also higher. Generally speaking, during dark hours, average and V_{85} speeds tend to be lower, although the standard deviation is higher (Kraemer *et al.*, 2005; Pérez-Acebo, 2018). However, research about

speed in speed humps and in control sections with similar values between daylight and darkness can be found in the literature (Jägerbrand, Johansson, and Laike, 2018). However, in this road, drivers tended to go faster at night, as they assumed that very few pedestrians might be crossing the carriageway.

Table 3. Values of selected variables at point A4/B3 during day and night

	Point A4		Point B3	
	Day	Night	Day	Night
V_m (km/h)	36,8	40,5	29,9	34,9
Standard deviation	10,2	10,6	10,5	11,1
V_{85} (km/h)	46	50	41	46
V_{max} (km/h)	74	80	80	65
Total number	1 117	212	1 231	180
Vehicles with v > 40 km/h (number)	383	105	196	59
Vehicles with v > 40 km/h (%)	34,3	49,5	15,9	11,1

Source: Authors
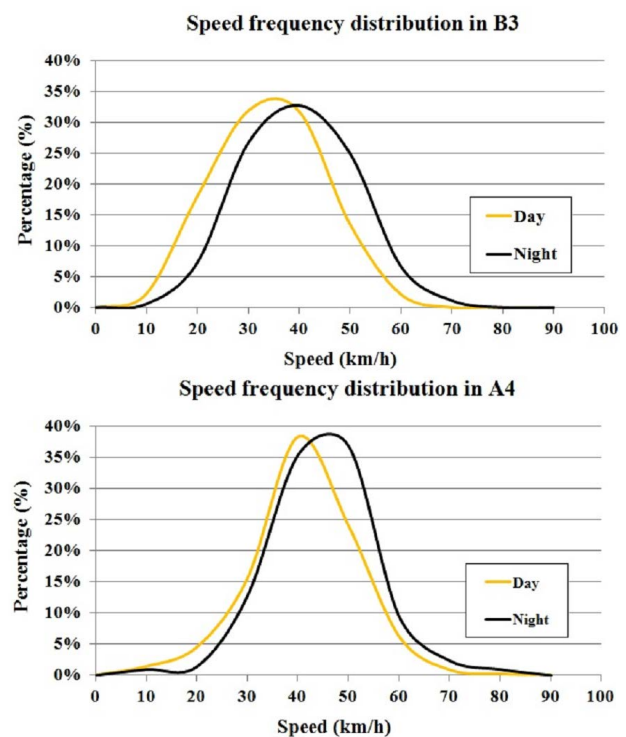
Figure 6. Speed frequency distribution in point A4/B3 during the daylight and night: a) in point B3, b) in point A4.
Source: Authors

Conclusions

In this paper, traffic lights turning red if the speed limit is exceeded were controlled to assess their efficiency as traffic calming measures, installed in the transition between an interurban and an urban area, in the case of interurban roads crossing a small, unbypassed village for a short length.

It was observed that few drivers respected the established speed limit by means of this kind of traffic lights if they are installed separately. However, their presence serves as a real traffic calming measure, given that, in the adjacent urban area, lower speeds were registered at the two crosswalks. Therefore, although these traffic lights are not widely respected, they suppose a warning signal about the presence of an urban area.

When the traffic lights are placed next to a crosswalk, their effect is improved, reaching a high percentage of compliance with the speed limit. Drivers really slow down due to this type of traffic lights and the crosswalk since a pedestrian may cross the road. Moreover, when comparing this effect with another crosswalk in the same direction after them, the traffic lights really work. Hence, placing the traffic lights and the crosswalk together reinforces the effect of both TCMs.

Finally, there is a difference between the speeds during daylight and dark hours. Speeds are higher at night and have a greater standard deviation in the crosswalk, even if the traffic lights are present. It seems that drivers do not respect the speed limit as they do during the day because they think that a pedestrian is less likely to be crossing the road.

Funding

References

Baratian-Ghorghi, F., Zhou, H., and Zech, W. C. (2016). Red-light running traffic violations: A novel time-based method for determining a fine structure. *Transportation Research Part A*, *93*, 55-65. 10.1016/j.tra.2016.08.015

Daniels, S., Martensen, H., Schoeters, A., Van de Berghe, W., Papadimitrou, E., Ziakopoulos, A., Kaiser, S., Aigner-Breuss, E., Soteropoulos, A., Wijnen, W., Weijermars, W., Carnis, L., Elvik, R., and Martín Pérez, O. (2019). A systematic cost-benefit analysis of 29 road safety measures. *Accident Analysis and Prevention*, *133*, 105292. 10.1016/j.aap.2019.105292

DGT (Dirección General de Tráfico) (2019). *Anuario estadístico de accidentes 2018*. Madrid, Spain: Dirección General de Tráfico, Ministerio del Interior.

EC (European Commission) (2010). *Towards a European road safety area: policy orientations on road safety 2011-2020. COM (2010) 389 final*. Brussels, Belgium: European Commission.

EUROSTAT (2018). *Energy, transport and environmental statistics – 2018*. Luxembourg, Luxembourg: Publications Office of the Union.

FHWA (Federal Highway Administation) (2018). *Facts & Statistics*. https://safety.fhwa.dot.gov/facts_stats/

Gonzalo-Orden, H., Rojo, M., Pérez-Acebo, H. and Linares, A. (2016). Traffic Calming Measures and their Effect on the Variation of Speed. *Transportation Research Procedia*, *18*, 349-356. 10.1016/j.trpro.2016.12.047

Gonzalo-Orden, H., Pérez-Acebo, H., Linares-Unamunzaga, A., and Rojo Arce, M. (2018). Effects of traffic calming measures in different urban areas. *Transportation Research Procedia*, *33*, 83-90. 10.1016/j.trpro.2018.10.079

Jägerbrand, A. K., Johansson, M., and Laike, T. (2018). Speed responses to speed humps as a affected by time of day and light conditions on a residential road with Light-Emitting Diode (LED) road lighting. *Safety, 4*, 10. 10.3390/safety4010010

Jensupakarn, A., and Kanitpong, K. (2018). Influences of motorcycle rider and driver characteristics and road environment on red light running behavior at signalized intersections. *Accident Analysis and Prevention*, *113*, 317-324. 10.1016/j.aap.2018.02.007

Kraemer, C., Pardillo, J. M., Rocci, S., Romana, M. G., Sánchez Blanco, V., and del Val, M. A. (2003). *Ingeniería de carreteras- Volumen I, 2ª edición*. Madrid, Spain: McGraw-Hill Interamericana.

Kveladze, I. and Agerholm, N. (2018). *Visual analysis of speed bumps using floating car dataset*. *Journal of Location Based Services*, *12*(2), 119-139. 10.1080/17489725.2018.1521010

Llau, A. F., Ahmed, N. U., Khan, H. M. R. U., Cevallos, F. G., and Pekovic, V. (2015). The Impact of Red Light Cameras on Crashes within Miami-Dade County, Florida. *Traffic Injury Prevention*, *16*, 773-780. 10.1080/15389588.2015.1023896

Llopis-Castelló, D. and Findley, D. J. (2019). Influence of Calibration Factors on Crash Prediction on Rural Two-Lane Two-Way Roadway Segments. *Journal of Transportation Engineering, Part A: Systems*, *145*(6), 040190241-04010249. 10.1061/JTEPBS.0000245

Lockwood, I. M. (1997). ITE Traffic Calming Definitions. *ITE J.*, 67, 22-24.

MFOM (Ministerio de Fomento) (2003). *FOM/3640/2003, de 28 de noviembre, por la que se aprueba la Norma 6.1-IC "Secciones de Firme", de la Instrucción de Carreteras*. Madrid, Spain: Ministerio de Fomento.

MFOM (Ministerio de Fomento) (2012). *Mapa de tráfico por provincias 2011*. Madrid, Spain: Dirección General de Carreteras.

MFOM (Ministerio de Fomento) (2016). *Mapa de tráfico por provincias 2015*. Madrid, Spain: Dirección General de Carreteras.

MFOM (Ministerio de Fomento) (2017). *Mapa de tráfico por provincias 2016*. Madrid, Spain: Dirección General de Carreteras.

Pérez-Acebo, H. (2018). *Carreteras. Volumen I: Red viaria y tráfico*. Bilbao, Spain: Servicio Editorial Universidad del País Vasco UPV/EHU.

Pérez-Acebo, H., Linares-Unamunzaga, A., Rojí, E., and Gonzalo-Orden, H. (2020). IRI performance models for flexible pavements in two-lane roads until first maintenance and/or rehabilitation work. *Coatings, 10*(2), 97. 10.3390/coatings10020097

Pérez-Sansalvador, J. C., Lakouari, N., García-Díaz, J., and Pomares Hernández, S. E. (2020). The effect of speed humps on instantaneous traffic emissions. *Applied Sciences*, *10*(5), 1592. 10.3390/app10051592

Ptak, M. (2019). *Method to Assess and Enhance Vulnerable Road User Safety during Impact Loading. Applied Sciences*, 9(5), 1000. 10.3390/app9051000

Shah, S. A. R. and Ahmad, N. (2019). Road Infrastructure Analysis with Reference to Traffic Stream Characteristics and Accidents: An Application of Benchmarking Based Safety Analysis and Sustainable Decision Making. *Applied Sciences, 9*(5), 2320. 10.3390/app9112320

Studer, L., Paglino, V., Gandini, P., Stelitano, A., Triboli, U., Gallo, F., and Andreoni, G. (2018). Analysis of the Relationship between Road Accidents and Psychophysical State of Drivers through Wearable Devices. *Applied Sciences, 8*(8), 1230. 10.3390/app8081230

Tefft, B.C. (2011). *Impact Speed and a Pedestrian's Risk of Severe Injury or Death*. Washington, D.C., USA: AAA Foundation for Traffic Safety. 10.1037/e550422012-001

Torres, J., Cloutier, M. S., Bergeron, J. and St-Denis, A. (2020).They installed a speed bump: children's perception of traffic calming measures around elementary schools. *Children's Geographies, 18*(4), 477-489. 10.1080/14733285.2019.1685075

TRB (Transportation Research Board) (2010). *NCHRP Report 672. Roundabouts: An Informational Guide*. Washington, D.C., USA: Transportation Research Board.

Ziolkowski, R. (2018). *Speed management efficacy on national roads – Early experiences of sectional speed system functioning in Podlaskie Voivodship. Transport Problems, 13*(2), 5-12. 10.20858/tp.2018.13.2.1

Simulation Strategy to Reduce Quality Uncertainty in the Sugar Cane Honey Process Design

Estrategia de simulación para reducir la incertidumbre de la calidad en el diseño del proceso de miel de caña de azúcar

Victor Cerda-Mejía [1], Amaury Pérez-Martínez [2], Estela Guardado-Yordi [3], Galo Cerda-Mejia [4], Karel Diéguez-Santana [5], Isnel Benítez-Cortés [6], and Erenio González-Suárez [7]

ABSTRACT

This work proposes to increase the acceptability of the sensory quality attributes of sugarcane honey by simulating and decreasing the uncertainty of operational parameters. To this effect, it relies on the development of a case study through a strategy that contemplates the analysis of the initial data and performs calculations through the use of mathematical models, the determination of the Sigma quality level, and the use of the GUM methodology (Guide to the expression of uncertainty in measurement). It was demonstrated that a range with a great variability in the initial operational parameters generated a Sigma level of less than three and a decrease in revenues of 30-52% due to low product sales for the studied productions. By decreasing pH uncertainty from 3,79 to 4,21, and Brix degrees from 75,13 to 76,88, an increase in the Sigma level of quality was observed, which exceeded six, in compliance with product quality specifications, as well as a reduction in economic losses due to defective products. The importance of quality in the product design and the process is evinced, given its influence on the acceptability of the product and the feasibility of the process.

Keywords: sigma quality level, simulation, uncertainty, sugarcane honey

RESUMEN

El trabajo propone incrementar la aceptabilidad de atributos de calidad sensorial del jarabe de caña de azúcar mediante la simulación y disminución de la incertidumbre de parámetros operacionales. Para ello, se apoya en el desarrollo de un estudio de caso a través de una estrategia que contempla el análisis de los datos iniciales y efectúa cálculos a través del empleo de modelos matemáticos, la determinación del nivel Sigma de calidad y de la metodología de la GUM (Guide to the Expression of Uncertainty in Measurement). Se demostró que un rango con gran variabilidad de los parámetros operacionales iniciales generaba un nivel Sigma menor que tres y una disminución de los ingresos del 30 al 52 %, debido a las bajas ventas de productos en las producciones estudiadas. Al disminuir la incertidumbre del pH de 3,79 a 4,21 y los grados Brix de 75,13 a 76,88, se garantizó un incremento del nivel Sigma de calidad superior a seis, en cumplimiento de las especificaciones de calidad del producto, y una reducción en las pérdidas económicas por productos defectuosos. Se evidencia la importancia de la calidad en el diseño del producto y del proceso, dada su influencia en la aceptabilidad del producto y la factibilidad del proceso.

Palabras clave: nivel sigma de calidad, simulación, incertidumbre, miel de caña de azúcar

[1] Food Engineer, Universidad Técnica de Ambato, Ecuador. Affiliation: Agregate Professor, Universidad Estatal Amazónica, Ecuador. E-mail: vcerd@uea.edu.ec
[2] Chemical Engineer, Universidad de Camagüey, Cuba. Ph.D., Universidad de Camagüey, Cuba. Affiliation: Agregate Professor, Universidad Estatal Amazónica, Ecuador. E-mail: amperez@uea.edu.ec
[3] Bachelor of Pharmacy, Universidad de Camagüey, Cuba. Ph.D., Universidad de Santiago de Compostela, España. Affiliation: Auxiliar Professor Universidad Estatal Amazónica, Ecuador. E-mail: e.guardadoy@uea.edu.ec
[4] Mechanical Engineer, Escuela Politécnica Nacional, Ecuador. M.Sc., Universidad de Barcelona, España. Affiliation: Auxiliar Professor, Universidad Estatal Amazónica, Ecuador. E-mail: galocerda.lm@gmail.com
[5] Chemical Engineer, Universidad Central "Martha Abreu" de Las Villas, Cuba. M.Sc., Universidad Central "Martha Abreu" de Las Villas, Cuba, Cuba. Affiliation: Auxiliar Professor, Universidad Estatal Amazónica, Ecuador. E-mail: kdieguez@uea.edu.ec
[6] Chemical Engineer, Universidad de Camagüey, Cuba. Ph.D., Universidad de Camagüey, Cuba. Affiliation: Full Professor, Universidad de Camagüey, Cuba. E-mail: isnel.benites@reduc.edu.cu
[7] Chemical Engineer, Universidad Central "Martha Abreu" de Las Villas, Cuba. D.Sc., Universidad Central "Martha Abreu" de Las Villas, Cuba. Affiliation: Full Professor, Universidad Central "Martha Abreu" de Las Villas, Cuba. E-mail: erenio@ucv.edu.cu

Introduction

Within the agroindustry, there are crucial goals such as quality, which must respond to the growing demands of the consumer. The development of new products and agroindustrial processes results from the interaction of men, materials, and equipment, which should establish an organized system that enables the maximization of benefits (Prieto, Mouwen, López Puente, and Cerdeño Sánchez, 2008). In this sense, process design or redesign in this type of industry acquires a special importance, since it is possible to

obtain the best combination of this interaction and achieve maximum economy at work (Espinel-Ríos and Ruiz-Espinoza, 2019; Pérez-Martínez et al., 2012). During process design, there is a cycle of activities that goes from the generation of alternative solutions to their corresponding analysis and the selection of the optimal alternative.

The non-centrifugal cane sugar industry has a great importance in developing countries because it is a livelihood for many families, due to its local and artisan production. Currently, many companies wish to expand the commercialization of their products without making large investments. There is an interest from many producers in achieving a stable quality in this process and its by-products (Velásquez, Espitia, Mendieta, Escobar, and Rodríguez, 2019). Reaching this technological goal paramount today because this type of product is being revalued in European markets for its nutritional value (Belitz, Grosch, and Schieberle, 2004; Jaffé, 2012; Lee et al., 2018).

In this problematic situation, there are cases of isolated studies in the literature where models and simulations of the non-centrifugal cane sugar manufacturing processes are applied. These are regarded as an alternative for process analysis and with an economic analysis. Theoretical results are also obtained, which helps decision making. However, they have focused primarily on energy efficiency and equipment redesign for non-centrifugal cane sugar production (López and Zuluaga, 2014; Restrepo, Flórez, and Tibaquirá, 2017). In the current literature, the use of these methodologies in the cane honey production process and its quality is little mentioned.

One of the main advantages of mathematical modeling is that shorter execution times are required, and it is cheaper than project execution, thus allowing to reduce the risks that could occur in real situations, as well as to quickly identify the expectations (Molina-Mora, 2017). On the other hand, simulation in the agro-industrial field is used today to predict the results of a process, which gives an answer to the phenomena that occur in it. In such a way, it allows to anticipate the operation of a modified or new process, knowing whether or not it will be viable (Bildea, Dimian, and Kiss, 2014).

Process simulation has been a widely used tool in process design, with or without taking uncertainty into account (Washington and Swartz, 2014). Uncertainty is considered a property from a collection of expectations, judgments about possible outcomes for a future event (Hansen and Pearce, 2014). Natural and technological systems usually face uncertainty (Cerda Mejía, Pérez-Martínez, González-Suárez, and Concepción Toledo, 2018; Rabassa-Olazábal, Eduardo-Guerra, Pérez-Sánchez, González-Suárez, and Pérez-Martínez, 2016; Sahinidis, 2004). Product and process design is not free from it (Bortz et al., 2017; Steimel and Engell, 2016). Due to the empirical and semi-empirical conditions in the production of non-centrifugal cane sugar and its derivatives such as honey this process is subject to uncertainty.

Therefore, there is a need to study it in product and process design (design and operational parameters), as well as in

quality (Rincón Arévalo, 2005). Thereupon, it is evident that uncertainty plays a very important role in the process of ensuring that a product meets certain quality specifications. For this purpose, it must be checked whether or not the analytical result is within a "tolerance" range of values defined in the specifications (Lawless and Heymann, 2010; Maroto, Boqué, Riu, and Rius, 2001).

In the uncertainty analysis during the production of cane honey, there should first be a focus on the raw material, because it can be affected by several factors, which cause variability in the Brix degrees and the pH, these being the main quality attributes for the elaboration of honey. The quality of the final product depends on the initial conditions of the raw material and the operational parameters. Some of the main factors that affect the quality of the cane are variety, cutting age, and cultural practices (Castro, Prado, Paladines, and Cervantes, 2017). Other authors describe that the uncertainty related to the operational parameters is present in temperature, pressure, and flow. Variations in temperature can be experienced during the energy supply stages (evaporation), and pressure variation could occur if vacuum evaporators are used (Espitia, Velásquez, López, Escobar, and Rodríguez, 2020; González Cortés, Pedraza Gárciga, Clavelo Sierra, and González Suárez, 2015).

As mentioned above, quality is a parameter of the product and the process that has a great variability. The quality of food products in the production of non-centrifugal cane sugar and other products of this process (cane honey), is still limited and little documented. Some factors hinder the quality and risk management of the processing, safety, and traceability of food products (Silva, Silva, Perestrelo, Nunes, and Câmara, 2017). However, some references could contribute to promoting the quality of the process and the product, such as the Quality by Design (QbD) approach, which has been applied with good results in the pharmaceutical industry. It is supported by the Design of Experiment (DoE), which allows the operational parameters to be correlated with the quality attributes (Oliva, Fariña, and Llabrés, 2013; Orlandini, Pinzauti, and Furlanetto, 2013; Pasquini et al., 2016; Tol, Kadam, Raotole, Desai, and Samanta, 2016). Along with these emerging approaches, there have been other studies that use artificial intelligence to achieve the same goals (Herwig, Garcia-Aponte, Golabgir, and Rathore, 2015; Uraikul, Chan, and Tontiwachwuthikul, 2007; Zhai, Xuan, Fan, Zhao, and Jiang, 2018).

In the agroindustrial processes and process design, the determining role of quality as an early stage of the process design and its consideration as a parameter, it is little documented (Phadke and Dehnad, 1988). An example of this is the process design carried out for products derived from the sugar industry, where the technological scheme is sometimes established from the experimental data, without holistically considering economic, environmental, technological, and transversal quality aspects (Aguilar-Rivera, Galindo, Fortanelli, and Contreras, 2009; Rabassa-Olazábal et al., 2016; Rabassa Olazábal, González Suárez, Pérez Sánchez, Miño Valdés, and Pérez Martínez, 2015). Moreover, the use of simulations is incipient, as well as the emerging sequential procedures that contemplate it (Yu and Kopcha, 2017).

Current research takes the production of sugarcane honey into consideration, where organoleptic aspects such as viscosity, flavor, and the possible presence of crystals (considered this as a defect) have a significant importance in the quality parameters of the sensory analysis, performed by the consumer, who identifies and personalizes sugarcane honey. Determination of these sensory parameters implies a certain degree of uncertainty because they are subjective.

In previous experimental investigations, a range of operational parameters caused a great variability in the sensory quality attributes of sugarcane honey (Quezada Moreno, González-Suárez, Quezada Torres, and Mera, 2016). Based on this case study, the aim of this research is to increase the acceptability of quality attributes (sensory) through simulation methodologies, and thus reduce uncertainty in operational parameters, as part of the process design to obtain sugarcane honey.

Materials and Methods

Excel macro was the tool used to implement a procedure to increase acceptability. It followed these general steps (Figure 1): 1) Determination (or analysis) of experimental data and mathematical models, 2) Simulation, 3) Determination of the number of defective products, 4) Determination of the Sigma quality level of the process, 5) Determination of the uncertainty (GUM Methodology). Case study was based on the data and models obtained in the research published by Quezada Moreno *et al.* (2016). The analyzed randomized batches were 10, 120, and 1560. These quantities are in accordance with the production that takes place in the Amazon Region of Ecuador for one day, one month, and one year.

Experimental data and mathematical models that correlate the operational parameters and final product quality

Operational parameters (pH and Brix degrees) were considered as independent variables and sensory quality attributes (taste, viscosity, and presence of crystals) as dependent variables. The correlation between sensory and operational parameters was taken from Quezada Moreno *et al.* (2016) in the form of statistical models. The variability of the dependent variables was determined considering the following statistical parameters as ranges: standard deviation and the mean absolute deviation (MAD) (Anderson, Sweeney, and William, 2014).

Simulation

For the simulation:

a) The probability distribution of the experimental data was determined considering the best goodness of fit, by means of the software Arena 7.01.

b) Random numbers were generated from the previous probability distribution, using Microsoft Excel. The
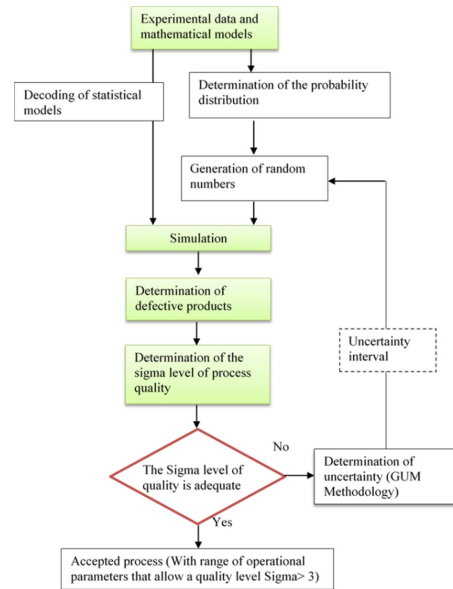
Figure 1. Procedure followed during process design.
Source: Authors

ranges used in the first iteration for this case study were obtained by *Quezada Moreno et al.* (2016), and, for subsequent iterations, they were determined using the GUM methodology (Pérez Hernández, 2012). The number of generated random samples was established according to production for a day, month, and year considering the mass balances.

c) Statistical models were decoded using STATISTIC software version 8,0.

The mathematical models and the obtained random numbers allowed us to calculate the new values of quality attributes such as flavor, viscosity, and the presence of crystals.

Determination of the number of defective products

From the attribute specifications of product quality (dependent variables) obtained from the simulation, defects per unit (DPU) and the percentage of defective products were determined. DPU refers to the quality attribute specifications that were not fulfilled. In this case study, values below six were considered defective in the sensory evaluation scalar test for each sensory attribute, where according to Ávila-de Hernández, González-Torrivilla (2011), and Hernandez Alarcon (2005), the control scale test in the sensory evaluation panels establishes a rating of six for "I like it a little", and 10 for "I like it a lot".

Determination of sigma quality level of the process

Sigma quality level of a process (Eq. 1) is calculated for each production based on its DPU with Equation (1), proposed by Abdelhamid (2003).

$$Z = Z_{DPU} + 1,5 \qquad (1)$$

Where Z is the sigma quality level and Z_{DPU} is the standard normal distribution corresponding to the DPU.

Other Sigma level metrics were also determined according to what was proposed by Keller (2011) and Pyzdek (2003).

a) Defects per million opportunities (DPMO) (Equation 2):

$$DPMO = \frac{DPU}{\text{Opportunities}} * 1\,000\,000 \qquad (2)$$

Where *Opportunities* is the value of the productions.

b) Yield (Yd) (Equation 3):

$$Yd\,(\%) = 100 - DPU \qquad (3)$$

Analysis of the Six-Sigma quality level of the process

In each iteration, it was analyzed whether at least the Three-Sigma quality of the process was reached, as recommended by Alderete, Colombo, Di Stéfano, and Wade (2003). This value is equivalent to a 93,32% acceptance of the total products (Table 1). Methodologically, this is a step in decision making, where Sigma level is reached or exceeded. Moreover, no further iterations were carried out following the procedure of Figure 1.

Table 1. Six-Sigma level values

Sigma level	Defect per million	Yield (%)
6	3,40	99,9997
5	233,00	99,9800
4	6 210	99,3000
3	66 807	93,3000
2	308 537	69,1500
1	690 000	30,8500
0	933 200	6,6800

Source: Gutierrez Pulido and de la Vara Salazar (2013).

Determination of uncertainty by the GUM methodology

In each iteration, the uncertainty of the operational parameters was determined through a modified GUM methodology (Pérez Hernández, 2012) in order to reduce the range of operational parameters until achieving greater acceptability of the quality attributes corresponding to a Sigma level greater than or equal to three. The steps were the following:

1. Mathematically expressing the relationship between the measurand (Y) input quantities (x_i).

2. Determining the estimated value of the input quantities (x_i) from the statistical analysis of a series of observations.

3. Evaluating the standard uncertainty of the input quantities ($u(x_i)$), where the evaluation should be type A or B.

4. Determining the combined standard uncertainty ($uc(y)$) for the measurand, the uncertainty for the input quantity, and covariances associated with input estimates.

5. Determining the value of the expanded uncertainty (Up) to provide an interval ($y - Up, y + Up$) where $Up = u_c(y) * k_p$ and $k_p = 1$ (Coverage factor).

Quantification of the economic benefit

The mass balances were proposed for sugarcane honey production to determine product quantity for each batch. This allowed quantifying and comparing income based on the accepted products. To this effect, referential market sale prices published in Ecuador were used.

Results and discussion

Experimental data and mathematical models that correlate the operational parameters and final product quality

It is known that some of the distinctive characteristics of agro-industries are the variability in the quantity and quality of raw materials. The amount is uncertain due to climatic changes or damage to crops or diseases. Quality varies because standardization of raw materials is still difficult to achieve, which contrasts with the specifications defined for standard materials used in the manufacture of other industries. These variations greatly influence the design and quality control of an agro-industrial plant (Austin, 1984).

The statistical behaviour of the sensory attributes of sugarcane honey is shown in Table 2. The range and mean absolute deviation for the three quality attributes demonstrate the great variability of each of the attributes obtained experimentally in previous studies. For the three attributes, the minimum and maximum values are distant, which results in range above seven. They are also at the extreme values of the hedonic scale used by Quezada Moreno *et al.* (2016). High MAD values represent the variability of the data and, therefore, of a greater dispersion of experimental values (Pérez, Aldana, and Arguello, 2016). Consequently, the new predicted values by the theoretical models will also show variability (Quispe and Purca, 2007).

Table 2. Statistics of the quality attributes of sugarcane honey based on data from Quezada Moreno *et al.* (2016)

Statisticians	Sensory attributes (dependent variables)		
	Viscosity	Flavor	Presence of crystals
Mean	4,2900	6,4800	6,4300
Standard deviation	3,9300	3,3900	3,1900
Range	8,9000	7,3000	8,1000
MAD	3,3900	3,0100	2,6700
Minimum	0,7000	1,9000	1,2000
Maximum	9,6000	9,2000	9,3000

Source: Authors

The pH values and Brix degrees are adjusted to a Beta distribution, which is a continuous probability distribution with two parameters α and β (Table 3). From this information, it is possible to generate the new random numbers.

Table 3. Parameters of the Beta distribution

Parameters	Operational parameters (independent variables)	
	pH	Brix degrees
Superior value	3,5000	74,0000
Lower value	4,5000	78,0000
Alpha	0,8030	0,8800
Beta	0,8010	0,9100

Source: Authors

Mathematical models for each of the response parameters are shown in Equations (4) and (6). Decoding allows to simulate directly with the experimental values or new generated values (for the first and second iteration in this case study). This new form of modelling is advantageous when compared to the statistical models provided by Quezada Moreno *et al.* (2016), due to the simplicity of the calculations when performing the simulations and subsequent analysis.

$$V = -10806.86 - 37.56X_1 + 0.33X_1^2 + 287.14X_2$$
$$- 1.90X_2^2 + 0.45X_1X_2 \quad (4)$$

$$S = 144.68 + 115.69X_1 - 13.13X_1^2 - 9.98X_2$$
$$+ 0.06X_2^2 - 0.04X_1X_2 \quad (5)$$

$$C = -4092.39 + 22.46X_1 - 3.79X_1^2 + 108.38X_2$$
$$+ -0.72X_2^2 - 0.07X_1X_2 \quad (6)$$

Where V (Viscosity), S (Taste), C (Presence of crystals), and X_1 (pH), X_2 (Brix degrees).

Simulation results

The case study was simulated for a production capacity of 10 batches per day (A). Moreover, it was studied for a one-month production of 120 batches (B) and another one-year production of 1 560 batches (C), which have a frequency of three times per week of production capacity correspondent to Ecuadorian Amazon Region production. This type of production is different from other regions of Ecuador, mainly in the main sugar mills, whose harvest begins in July and ends in December. Sugar production occurs throughout the year, working six days a week, and the harvest period is not carried out between January and February.

The analysis for the first iteration was performed following the procedure in Figure 1 with 10, 120, and 1560 random numbers in correspondence with these productions. When analyzing the product quality specifications according to sensory attributes (Figure 2), there is a tendency to increase the quantity of defective products as production increases,

for the three sensory quality attributes. The percentage of defective products for productions A, B, and C was 30,00%, 50,83%, and 52,63%, respectively. If this research is considered to have been carried out in the context of process design, this trend is not desirable, since income would decrease.
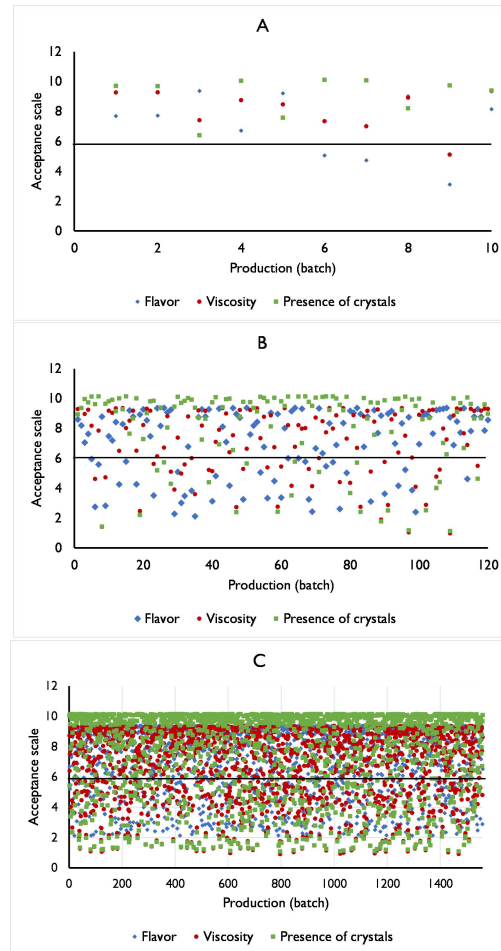
Figure 2. Simulation of the quality attributes for the first iteration. (A) Production for 10 batch; (B) Production for 120 batch; (C) Production for 1 560 batch.
Source: Authors

According to the previous considerations, in the present case study, performing new iterations to reduce uncertainty and the number of defective products based on the defined quality attributes is suggested, as well as determining the best product acceptability range.

The number of defective products of the second iteration (Figure 3) is still around 10% for production A. However, in productions B and C, a 0% in defects was achieved when compared with the results obtained in the first iteration. The range of operational parameters for each production was measured until the number of defectives reached the desired Sigma Level value of 3 (Table 1), thus demonstrating the effectiveness of the proposed methodology (Figure 1).
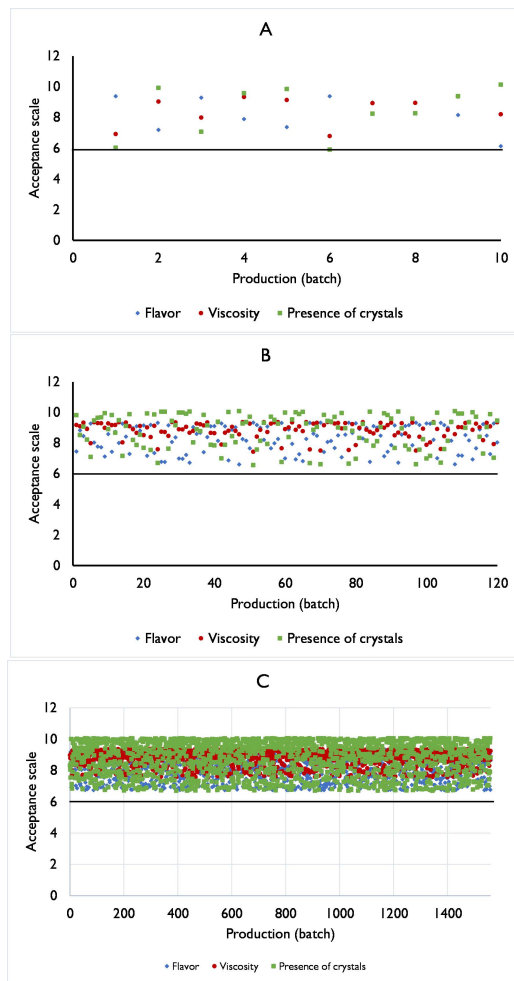
Figure 3. Simulation of the quality attributes for the second iteration. (A) Production for 10 batch; (B) Production for 120 batch; (C) Production for 1560 batch.
Source: Authors

The simulation was performed until the third iteration for production A, where defective products were not obtained (Figure 4). The GUM methodology allowed to reduce the range of operational parameters (pH and Brix degrees), and the decrease in the number of defective products was obtained as the production increased.

Determination and analysis of the Six-Sigma quality level of the process

Sigma level for A, B and C productions in the first iteration corresponded to 1, where the yield (% of products accepted) was in a range between 47,37 and 70,00, and a Sigma value of less than 3 (Table 4). As a restriction, it is necessary to reach at least 93,3% of yield, as has been proposed (Gutierrez Pulido and de la Vara Salazar, 2013), thus achieving the Sigma 3 level and concluding the simulation. The equivalent 93,32% of the historical standard is equivalent to almost 67 000 defects per million opportunities (Alderete *et al.*, 2003; Allen, 2019; Laureani and Antony, 2019). By consensus, companies have accepted Sigma 3 or Sigma 4 as standard
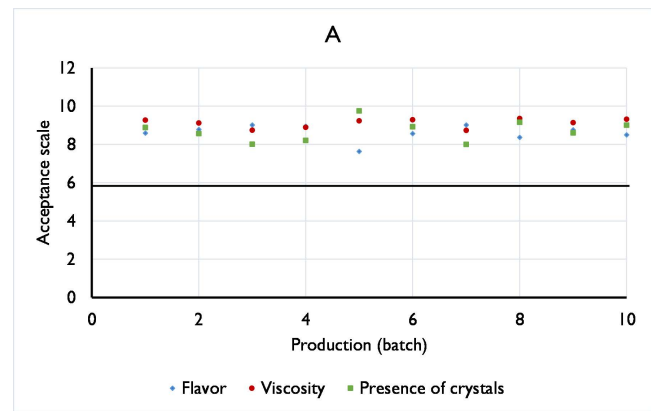
Figure 4. Simulation of the quality attributes for the third iteration for production A.
Source: Authors

(99,38% is the current standard, equivalent to almost 6 250 defects per million opportunities).

In subsequent simulations (iterations 2 and 3) of production A, it was possible to estimate a Sigma level of 2,78 for the second iteration, and higher than Six-Sigma in the third. After the third iteration, Six Sigma was reached, where the yield is close to 100%. This means that all products meet the organoleptic quality specifications. Productions B and C have better performance since the desired Sigma level is reached from the second iteration. Reaching Six Sigma, it is equivalent to having less than four defects for every million opportunities (99,99966%), which means a higher quality level (Alderete *et al.*, 2003; Allen, 2019; Laureani and Antony, 2019).

Table 4. Sigma level of the process for different productions

Parameters	Iteration 1			Iteration 2			Iteration 3
	Prod. A	Prod. B	Prod. C	Prod. A	Prod. B	Prod. C	Prod. A
Total accepted	7,00	59,00	739,00	9,00	120,00	1560,00	10,00
Total rejected	3,00	61,00	821,00	1,00	0,00	0,00	0,00
Yield (%)	70,00	49,17	47,37	90,00	100,00	100,00	100,00
Sigma level	2,02	1,48	1,43	2,78	>6,00	>6,00	>6,00

Source: Authors

Determination of uncertainty by the GUM methodology

The reduction in uncertaninty is achieved for each of the operational parameters (Table 5). The initial pH range was 3,5-4,5, and the Brix degrees were 74,0-78,0, which characterizes the experimental sample (Table 3). The GUM methodology makes it possible to reduce the range of each operational parameter in each of the iterations, but decision-making should take into account whether the desired Sigma level has been reached. For example, in the case of production A, iteration continues until the Sigma 3 level is reached. This quality level is reached in iteration 2 for a pH range of 3,89-4,11 and Brix degrees of 75,52-76,48. The range suggested for

process design of these operational parameters correspondz to production B, where the pH should be between 3,79-4,21 and the Brix degrees at 75,13-76,88. This selection is based on the fact that the range of the operating parameters for the rest of the studied production variants (A and C) are included in the selected range of production B.

Table 5. Results of uncertainty by GUM methodology

Parameters of the GUM methodology	pH				Brix degrees			
	Iteration 1			Iteration 2	Iteration 1			Iteration 2
	Prod. A	Prod. B	Prod. C	Prod. A	Prod. A	Prod. B	Prod. C	Prod. A
Mean	3,89	3,95	4,00	3,98	75,00	75,77	75,95	75,89
Expanded uncertainty	0,21	0,29	0,31	0,18	0,81	1,12	1,18	0,70
Upper and lower limit	4,29 3,71	4,21 3,79	4,19 3,81	4,11 3,89	77,19 74,81	76,88 75,13	76,82 75,18	76,48 75,52
Sigma level reached	<3	>6	>6	>6	<3	>6	>6	>6

Source: Authors

The implemented range should not only include criteria of the Sigma level but also of the technological level, which should be available for its implementation and control. It should also be taken into consideration that, for this type of analysis (sensory), potential consumers constitute an important decision factor when a new product is to be introduced in the market. Therefore, food quality is a set of properties and characteristics that confer the ability to fulfill some implicit needs expressed by the consumer, but whose evaluation in any of its categories, including the sensory, is not free of errors (uncertainty).

During food product design, some of the quality specifications should come from an adequate sensory analysis. Due to, it influences in the different stages not only of the design but also of its manufacture, maintenance, improvement, and optimization, as well as the evaluation of the potential market (Moskowitz, Beckley, and Resurreccion, 2012). For this reason, sensory evaluation is regarded today as a scientific discipline, which is used to measure, analyze, and interpret reactions to some characteristics of food and materials. In the food industry, the compounds are perceived by the senses (sight, smell, taste, touch, and hearing), which, as a whole, constitute food quality, together with microbiological, nutritional, and toxicological aspects (Lawless and Heymann, 2010; Stone, 2018; Stone and Sidel, 2004).

In this process, the upper and lower limits for each operational parameter are very close. Therefore, for subsequent stages should evaluate the implementation of an automatic control system, which can keep these parameters within calculated theoretical ranges. Regarding the implementation of these results at the local level, it should be considered that the production carried out in Pastaza is artisanal and with technological backwardness, so this would not be feasible under current conditions.

The presented and validated methodological proposal provides an alternative to reduce the variability in quality in process design. By incorporating the GUM methodology

as a tool for this purpose, it is also possible to reduce the systematic errors that may be present during the simulation. These errors are dependent on the selected model and error propagation at the time of the simulation. Although the GUM methodology has been proposed to be applied in other fields of quality, the advantages with respect to its easy implementation make it possible to suggest it in the design of processes. Its use becomes more important when quality and its variability are taken into account within a holistic context of analysis. The mentioned advantages allow recommending its use and validating it in other case studies of agro-industrial process design.

Systematic approaches such as QbD, which begins with predefined objectives and emphasizes the understanding of the design and control of products and processes, as well as the prediction of quality risk, should also be taken into account for future research (Yu, 2008; Yu and Kopcha, 2017). The rigor and advances in process design in the pharmaceutical industry allow us to extrapolate some concepts to agro-industries. We suggest identifying the characteristics that are critical to quality from the consumer's perspective, and translate them into the attributes that the agro-industrial product must possess, in addition to establishing how the critical parameters of the process can be varied to consistently produce an agro-industrial product with desired characteristics. This will allow to implement a flexible and robust manufacturing process that can adapt and produce a consistent product over time.

Some of the reference QbD elements (Yu, 2008) that are used for the design of new agro-industrial processes are: a) product design, product development, and manufacturing processes; b) identifying critical quality attributes, process parameters, and source variability; c) define the quality profile of the target product; and d) control the manufacturing processes to produce quality over time. In this research, following the methodological proposals of this approach has not been proposed as an objective. Although it has not been the aim of this research to follow methodological proposals of this approach (QbD), it is interesting to note that there are coincidences between the goal of the steps proposed by QbD and the procedure presented (Figure 1). At present, Computer-Aided Process Design (CAPD) method is used to design chemical, pharmaceutical, or agro-industrial processes (Petrides, Koulouris, and Lagonikos, 2002).

This research contributes knowledge to process design. For example, one should be careful when establishing a technological scheme based exclusively on experimental results, since there is a risk that, once in production, there will be defective products. Moreover, complementing the experimental results with new theoretical calculations (simulations), as well as with an uncertainty analysis, can reduce the number of defects. However, this evaluation is focused on a subsystem of quality analysis that can contribute to decision making during process design, which should consider technical, environmental, economic, and quality requirements (Cerda Mejía *et al.*, 2017; Pérez-Martínez *et al.*, 2012).

Economic benefit

Sugarcane processing capacity in Pastaza region is 757 kg/batch. Regardless of the sugarcane variety, moisture content and Brix degrees vary, which remains approximately around 15 (Figure 5). Taking into account these data, the estimated production of sugarcane honey is around of 144,52 kg/batch. Accordingly, its commercialization in the regional market is in a presentation of 460 g at a sale price of 2,70 USD. Therefore, in each batch production of 314 units is obtained.
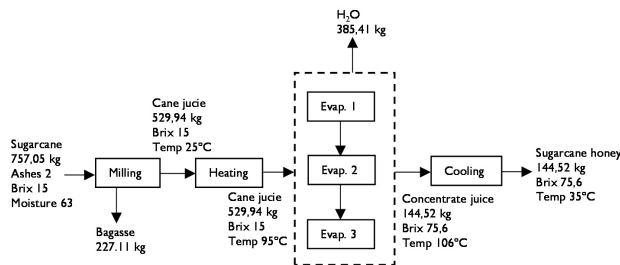
Figure 5. Flowsheet of the sugarcane honey production process.
Source: Authors

Analyzing the first iteration and the losses caused by the defective products. It was found that income reduces in the amount of 696 429 USD in a year of production (Table 6). This means that the data provided by Cerda Mejía *et al.* (2017) and Quezada Moreno *et al.* (2016) would have a huge economic impact. The negative effect of the number of defective products on the income for this iteration ranges between 30% and 52% in the range of the studied productions. These values demonstrate that the process is not economically feasible and that the investment runs the risk of not being recovered. Therefore, the selection of the range of operational parameters under study influences compliance with quality specifications and economic losses, since it affects the decrease in revenues from the sale of the product.

Table 6. Sigma level of the process for different productions

Parameters	Iteration 1			Iteration 2			Iteration 3
	Prod. A	Prod. B	Prod. C	Prod. A	Prod. B	Prod. C	Prod. A
Total accepted	7,00	59,00	739,00	9,00	120,00	1 560,00	10,00
Total rejected	3,00	61,00	821,00	1,00	0,00	0,00	0,00
Economic loss due to defectives (USD)	2 544	51 744	696 429	848,27	0,00	0,00	0,00
Impact on income (%)	-30,00	-50,83	-52,63	-10,00	0,00	0,00	0,00

Source: Authors

If the process were designed considering only productions A, Bs and C with the experimental data of Quezada Moreno *et al.* (2016). The process would not have been feasible from an economic point of view because the income would have been half. It is recommended to follow the methodological steps proposed in this research (Figure 1), since, by decreasing the uncertainty of the operational parameters (iteration 2), as

previously mentioned, productions B and C reached quality levels above the recommended Sigma level, and the economic impact was reflected on income with a positive total balance (Table 6).

During the performed design and quality analysis, a set of tasks or previous steps were performed, such as influence determination of the operational parameters on the product quality through technological surveillance or experimentation and the capacity estimation when performed following the methodology proposed and validated by (Pérez-Martínez, Benítez-Cortés, Oquendo-Ferrer, Julián-Ricardo, and Galindo-Llanes, 2013; Pérez-Martínez *et al.*, 2012). This methodology is the basis for this research. At the time, it was validated but it did not detail how quality should be analyzed as an aspect in process design. Therefore, by incorporating this preliminary quality analysis (Figure 1), the field is enriched, since not only will it be possible to generate optimal technological alternatives evaluated as economically feasible, environmentally compatible, and technologically feasible as proposed, but it also will contain quality criteria that allow its acceptability.

All this suggests that this type of quality analysis considers the relationship between product development and process design, which can be included in the conceptualization and ideation phases of a project, where it can contribute to the development of base concepts, creation of product lines, or concepts. It represents a new product, whose validation is required through new case studies. It has been recognized that the success of a design depends on the degree of the process specifications and considers it essential that quality indicators are measurable and predictable, since it determines the value of the product and consumer preference (Hadiyanto, Esveld, Boom, van Straten, and van Boxtel, 2008; M. Hadiyanto, 2007).

Conclusions

Quality should be considered both in product and process design for its future implications, which are related to product acceptability and feasibility of the process, elements that are interrelated. This should be valued with the same importance as the economic, technological, and environmental aspects.

The proposed methodology combines mathematical modeling, process simulation, quality, and uncertainty as elements that incorporate information into the decision-making of process design. The use of the GUM methodology reduced the variability of the quality attributes and is a distinctive element of the current project.

The case study shows that there is a relationship between operational parameters and process response parameters. It was shown that a range of operational parameters of pH (3,5-4,5) and Brix degrees (74-78) corresponding to data obtained from experimentation, which generates a Sigma level less of than three and a decrease in income from 30 to 52 % in product sales for the productions of 10, 120 and 1560 batches. The decrease in the uncertainty of the operational parameters (pH of 3,79-4,21 and Brix degrees of 75,13-76.88)

guaranteed i) an increase in the Sigma level to a value greater than six; ii) zero percent defects; iii) compliance with product quality specifications; and iv) reduce economic loss due to defective products.

Acknowledgements

References

Abdelhamid, T. S. (2003). *Six-Sigma in Lean Construction Systems: Opportunities and Challenges.* Paper presented at the 11th Annual Conference of the International Group for Lean Construction, Virginia, USA.

Aguilar-Rivera, N., Galindo, G. M., Fortanelli, J. M., and Contreras, C. S. (2009). ¿Por qué diversificar la agroindustria azucarera en México? *Revista de Globalización, Competitividad y Gobernabilidad, 3*(7), 62-75. 10.3232/GCG.2009.V3.N1.03

Alderete, V. P., Colombo, A. L., Di Stéfano, V., and Wade, P. (2003). *SIX SIGMA "0 de cómo las pinzas y martillos se tornan tecnología de punta.* Paper presented at the XXVI Congreso del Instituto Argentino de Profesores Universitarios de Costos.

Allen, T. T. (2019). Design for Six Sigma. In *Introduction to Engineering Statistics and Lean Six Sigma: Statistical Quality Control and Design of Experiments and Systems* (pp. 543-550). London: Springer London. 10.1007/978-1-4471-7420-2_21

Anderson, D. R., Sweeney, D. J., and William, T. A. (2014). *Statistics for busines and eonomics* (Vol. 12 Ed.). Mexico: CENGAGE Learning.

Austin, J. E. (1984). *Agroindustrial project analysis*. Retrieved from altimore, MD: Johns Hopkins University Press.

Ávila-de Hernández, R. M., and González-Torrivilla, C. C. (2011). La evaluación sensorial de bebidas a base de fruta: Una aproximación difusa. *Universidad, Ciencia y Tecnología, 15*(60), 171-182.

Belitz, H. D., Grosch, W., and Schieberle, P. (2004). Sugars, Sugar Alcohols and Honey. In *Food Chemistry*. Berlin, Heidelberg: Springer. 10.1007/978-3-662-07279-0

Bildea, C. S., Dimian, A. C., and Kiss, A. (2014). *Integrated design and simulation of chemical processes*. Amsterdam, Netherlands: Elsevier Science.

Bortz, M., Burger, J., von Harbou, E., Klein, M., Schwientek, J., Asprion, N., Bötcher, R., Küffer K.-H., and Hasse, H. (2017). Efficient Approach for Calculating Pareto Boundaries under Uncertainties in Chemical Process Design. *Industrial and Engineering Chemistry Research, 56*(44), 12672-12681. 10.1021/acs.iecr.7b02539

Castro, C., Prado, E., Paladines, R., and Cervantes, A. (2017). Factores que afectan al cultivo de caña de azúcar para producción de bioetanol en Ecuador. *European Scientific Journal, 3*(24), 58-65. 10.19044/esj.2017.v13n24p58

Cerda Mejía, V. R., Pérez-Martínez, A., González-Suárez, E., and Concepción Toledo, D. (2018). *Aplicación de métodos matemáticos que desde el diseño de procesos garanticen la calidad en industrias de procesos.* Paper presented at the XV Seminario Iberoamericano para el Intercambio y la Actualización en Gerencia de Ciencia y Tecnología IBERGECYT 2018, Habana.

Cerda Mejía, V. R., Quezada Moreno, W. F., Pérez-Martínez, A., Oquendo-Ferrer, H., Torres, V., Cerda-Mejía, L., and González Suárez, E. (2017). *Influence of the uncertainty of the operational parameters in obtaining cane syrup in sensorial attributes.* Paper presented at the MOL2NET 2016, International Conference on Multidisciplinary Sciences, 2nd edition session MODEC01: Workshop on Natural Products and Agro-Industrial Procesess in Amazon, Ecuador. 10.3390/mol2net-02-03897

Espinel-Ríos, S. and Ruiz-Espinoza, J. E. (2019). Production of 1, 3-propanediol from crude glycerol: Bioprocess design and profitability analysis. *Revista mexicana de ingeniería química, 18*(3), 831-840. 10.24275/uam/izt/dcbi/revmexingquim/2019v18n3/Espinel

Espitia, J., Velásquez, F., López, R., Escobar, S., and Rodríguez, J. (2020). An engineering approach to design a non-centrifugal cane sugar production module: A heat transfer study to improve the energy use. *Journal of Food Engineering, 274*, 109843. 10.1016/j.jfoodeng.2019.109843

González Cortés, M., Pedraza Gárciga, J., Clavelo Sierra, D. A., and González Suárez, E. (2015). Incertidumbre en la integración de procesos para el desarrollo de biorefinerías. *Centro Azúcar, 42*(3), 30-38. http://scielo.sld.cu/scielo.php?script=sci_arttext&pid=S2223-4861201500030000 04

Gutierrez Pulido, H. and de la Vara Salazar, R. (2013). *Control Estadístico de Calidad y Seis Sigma* (Tercera edición). México, D.F.: McGraw Hill.

Hadiyanto, Esveld, D. C., Boom, R. M., van Straten, G., and van Boxtel, A. J. B. (2008). Product quality driven design of bakery operations using dynamic optimization. *Journal of Food Engineering, 86*(3), 399-413. 10.1016/j.jfoodeng.2007.10.015

Hadiyanto, M. (2007). *Product quality driven food process design* (S. Gerrit van, B. Remko, and T. van Boxtel Eds.). Netherlands: Wageningen University.

Hansen, N. C. and Pearce, M. T. (2014). Predictive uncertainty in auditory sequence processing. *Frontiers in Phsycology, 5*(1052), 1-17. 10.3389/fpsyg.2014.01052

Hernandez Alarcon, E. (2005). *Evaluacion sensorial* Bogotá, Colombia: Universidad Nacional Abierta y a Distancia

Herwig, C., Garcia-Aponte, O. F., Golabgir, A., and Rathore, A. S. (2015). Knowledge management in the QbD paradigm: manufacturing of biotech therapeutics. *Trends in Biotechnology, 33*(7), 381-387. 10.1016/j.tibtech.2015.04.004

Jaffé, W. R. (2012). Health effects of non-centrifugal sugar (NCS): A review. *Sugar Tech, 14*(2), 87-94. 10.1007/s12355-012-0145-1

Keller, P. (2011). *Six Sigma DeMYSTiFieD* (Vol. 2nd Edition): McGraw-Hill.

Laureani, A. and Antony, J. (2019). Leadership and Lean Six Sigma: a systematic literature review. *Total Quality Management and Business Excellence, 30*(1-2), 53-81. 10.1080/14783363.2017.1288565

Lawless, H. T. and Heymann, H. (2010). *Sensory Evaluation of Food: Principles and Practices*. New York: Springer-Verlag. 10.1007/978-1-4419-6488-5_3

Lee, J. S., Ramalingam, S., Jo, I. G., Kwon, Y. S., Bahuguna, A., Oh, Y. S., Kwon, O.-J., and Kim, M. (2018). Comparative study of the physicochemical, nutritional, and antioxidant properties of some commercial refined and non-centrifugal sugars. *Food Research International, 109*, 614-625. 0.1016/j.foodres.2018.04.047

López, S., and Zuluaga, C. (2014). Modelo semifísico de base fenomenológica de un evaporador de jugo de caña de azúcar tipo Roberts. *Ingenio Magno, 4*(7), 32-38. http://revistas.ustatunja.edu.co/index.php/ingeniomagno/article/view/748

Maroto, A., Boqué, R., Riu, J., and Rius, F. (2001). Incertidumbre y precisión. *Técnicas de Laboratorio, 266*, 834-837. http://www.quimica.urv.es/quimio/general/incert.pdf

Molina-Mora, J. (2017). Mathematical modeling as a didactic strategy for calculus teaching. *Uniciencia, 31*(2), 19-36. 10.15359/ru.31-2.2

Moskowitz, H. R., Beckley, J. H., and Resurreccion, A. V. (2012). Sensory and consumer research in food product design and development. Hoboken, NJ: John Wiley & Sons.

Oliva, A., Fariña, J. B., and Llabrés, M. (2013). Development and validation of an UPLC method for determination of content uniformity in low-dose solid drugs products using the design space approach. *Talanta, 115*, 490-499. 10.1016/j.talanta.2013.05.060

Orlandini, S., Pinzauti, S., and Furlanetto, S. (2013). Application of quality by design to the development of analytical separation methods. *Analytical and Bioanalytical Chemistry, 405*(2), 443-450. 10.1007/s00216-012-6302-2

Pasquini, B., Orlandini, S., Caprini, C., Del Bubba, M., Innocenti, M., Brusotti, G., and Furlanetto, S. (2016). Cyclodextrin- and solvent-modified micellar electrokinetic chromatography for the determination of captopril, hydrochlorothiazide and their impurities: A Quality by Design approach. *Talanta, 160*, 332-339. 10.1016/j.talanta.2016.07.038

Pérez-Martínez, A., Benítez-Cortés, I., Oquendo-Ferrer, H., Julián-Ricardo, M. C., and Galindo-Llanes, P. (2013). Integración del diseño del sistema de control automático al diseño total de una planta para obtención de alimento animal a partir de residuos de la industria azucarera. *ICIDCA. Sobre los Derivados de la Caña de Azúcar, 47*(2), 42-51. https://www.redalyc.org/articulo.oa?id=223128548007

Pérez-Martínez, A., Cervantes-Mendieta, E., Julián-Ricardo, M. C., González-Suárez, E., Gómez-Atanay, A., Oquendo-Ferrer, H., Galindo-Llanes, P., and Ramos-Sánchez, L. (2012). Procedimiento para enfrentar tareas de diseño de procesos de la industria azucarera y sus derivados. *Revista Mexicana De Ingeniería Química, 11*(2), 333-349. http://www.rmiq.org/ojs311/index.php/rmiq/article/view/1580

Pérez Hernández, M. M. (2012). Estimación de incertidumbres. Guía GUM. *e-medida. Revista Española de Metrología, 1*(3), 113-130. https://www.uv.es/meliajl/Docencia/Web Complementarios/GuiaGUM_e_medida.pdf

Pérez, J. I., Aldana, G. J., and Arguello, G. J. (2016). Modelo de Dispersión Axial para Sistemas de Flujo Continuo Ajustado a las Condiciones de Borde. *Información Tecnológica, 27*, 169-180. 10.4067/S0718-07642016000100018

Petrides, D. P., Koulouris, A., and Lagonikos, P. T. (2002). The role of process simulation in pharmaceutical process development and product commercialization. *Pharmaceutical Engineering, 22*(7), 56-65. https://ispe.org/sites/default/files/attachments/public/Jan-Feb-2002.pdf

Phadke, M. S., and Dehnad, K. (1988). Optimization of product and process design for quality and cost. *Quality and Reliability Engineering International, 4*(2), 105-112. 10.1002/qre.4680040205

Prieto, M., Mouwen, J. M., López Puente, S., and Cerdeño Sánchez, A. (2008). Concepto de calidad en la industria Agroalimentaria. *Interciencia, 33*(4), 258-264. https://www.researchgate.net/publication/46406312_Concepto_de_calidad_en_la_industria_agroalimentaria

Pyzdek, T. (2003). *The six sigma project planner. A step-by-step guide to leading a six sigma project through DMAIC*. United States of America: McGraw-Hill.

Quezada Moreno, W., González-Suárez, E., Quezada Torres, W., and Mera, M. (2016). Cane Honey?: Process, Quality and Harmlessness. *International Journal of Engineering Research, 5*(7), 589-593. https://www.academia.edu/27147573/Cane_Honey_Process_Quality_and_Harmlessness

Quispe, C. and Purca, S. (2007). Previsión de la temperatura superficial del mar frente a la costa peruana mediante un modelo autorregresivo integrado de media móvil. *Revista Peruana de Biología, 14*(7), 109-115. 10.15381/rpb.v14i1.2164

Rabassa-Olazábal, G., Eduardo-Guerra, L., Pérez-Sánchez, A., González-Suárez, E., and Pérez-Martínez, A. (2016). Consideración de la incertidumbre en la propuesta de nuevas oportunidades de negocio en la Empresa Azucarera Ignacio Agramonte, Camagüey. *Tecnología Química, 36*(2), 147-160. https://tecnologiaquimica.uo.edu.cu/index.php/tq/article/view/1114

Rabassa Olazábal, G., González Suárez, E., Pérez Sánchez, A., Miño Valdés, J. E., and Pérez Martínez, A. (2015). D-Xilosa y Glucosa a partir de residuos de la Industria Azucarera. *Revista Científica de la UCSA, 2*(2), 6-22. 10.18004/ucsa/2409-8752/2015.002(2)006-022

Restrepo, Á., Flórez, L. C., and Tibaquirá, J. E. (2017). Diseño, simulación y construcción de un serpentín evaporador para la industria panelera a baja escala en Colombia. *Ingeniería Mecánica, 20*(2), 51-57. https://ingenieriamecanica.cujae.edu.cu/index.php/revistaim/article/view/557

Rincón Arévalo, P. (2005). *Optimización del diseño y rediseño de procesos químicos complejos bajo incertidumbre mediante cooperación de técnicas de programación matemática y metaheurísticas.* (Doctoral thesis, Universidad Politécnica de Madrid, Madrid, Spain) http://oa.upm.es/426/1/05200521.pdf

Sahinidis, N. V. (2004). Optimization under uncertainty: state-of-the-art and opportunities. *Computers and Chemical Engineering, 28*(6), 971-983. 10.1016/j.compchemeng.2003.09.017

Silva, P., Silva, C. L., Perestrelo, R., Nunes, F. M., and Câmara, J. S. (2017). A useful strategy based on chromatographic data combined with quality-by-design approach for food analysis applications. The case study of furanic derivatives in sugarcane honey. *Journal of Chromatography A, 1520*, 117-126. 10.1016/j.chroma.2017.09.019

Steimel, J., and Engell, S. (2016). Optimization-based support for process design under uncertainty: A case study. *AIChE Journal, 62*(9), 3404-3419. 10.1002/aic.15400

Stone, H. (2018). Example food: What are its sensory properties and why is that important? *npj Science of Food, 2*(7), 11. 10.1038/s41538-018-0019-3

Stone, H., and Sidel, J. L. (2004). 1 - Introduction to Sensory Evaluation. In H. Stone and J. L. Sidel (Eds.), *Sensory Evaluation Practices* (*Third Edition*) (pp. 1-19). San Diego: Academic Press. 10.1016/B978-012672690-9/50005-6

Tol, T., Kadam, N., Raotole, N., Desai, A., and Samanta, G. (2016). A simultaneous determination of related substances by high performance liquid chromatography in a drug product using quality by design approach. *Journal of Chromatography A, 1432*, 26-38. 10.1016/j.chroma.2015.12.080

Uraikul, V., Chan, C. W., and Tontiwachwuthikul, P. (2007). Artificial intelligence for monitoring and supervisory control of process systems. *Engineering Applications of Artificial Intelligence, 20*(2), 115-131. 10.1016/j.engappai.2006.07.002

Velásquez, F., Espitia, J., Mendieta, O., Escobar, S., and Rodríguez, J. (2019). Non-centrifugal cane sugar processing: A review on recent advances and the influence of process variables on qualities attributes of final products. *Journal of Food Engineering, 255*, 32-40. 10.1016/j.jfoodeng.2019.03.009

Washington, I. D., and Swartz, C. L. E. (2014). Design under uncertainty using parallel multiperiod dynamic optimization. *AIChE Journal, 60*(9), 3151-3168. 10.1002/aic.14473

Yu, L. X. (2008). Pharmaceutical Quality by Design: Product and Process Development, Understanding, and Control. *Pharmaceutical Research, 25*(4), 781-791. 10.1007/s11095-007-9511-1

Yu, L. X., and Kopcha, M. (2017). The future of pharmaceutical quality and the path to get there. *International Journal of Pharmaceutics, 528*(7), 354-359. 10.1016/j.ijpharm.2017.06.039

Zhai, C.-H., Xuan, J.-B., Fan, H.-L., Zhao, T.-F., and Jiang, J.-L. (2018). The application of SVR model in the improvement of QbD: a case study of the extraction of podophyllotoxin. *Drug Development and Industrial Pharmacy, 44*(9), 1506-1511. 10.1080/03639045.2018.1467924

PLL Wrap Function for Synchronization in Phase Jump Disturbances

Función de ajuste de un PLL para la sincronía ante perturbaciones de salto de fase

Clementina Rueda-Germán[1], Iván de Jesús Rivas-Cambero[2], Hossam A. Gabbar[3], and José Humberto Arroyo-Núñez[4]

ABSTRACT

Synchrony plays a major role in the interconnection process between local electric power generation systems and the electrical grid. Grid phase disturbances prevent the generation system from maintaining synchrony. Therefore, an efficient phase tracking method is necessary in order to detect phase jumps and abrupt changes in amplitude. In this paper, we propose a software-designed method to strengthen phase tracking based on the wrap process of a second-level Phase Locked Loop (PLL). The term 'wrap' means establishing the phase values of the reference signal in intervals of π to match it with the values obtained from the PLL output (sync pulse). To quantify phase error, a mathematical transformation of the time domain to the frequency domain is implemented. The validity of the proposed wrap function is verified using electrical disturbances.

Keywords: single phase stockticker PLL, SPLL, phase disturbance, wrap, fast Fourier transform, FFT, phase error

RESUMEN

La sincronía es primordial para la interconexión de sistemas locales de generación de energía con el sistema eléctrico. Las perturbaciones en fase evitan que el sistema de generación mantenga la sincronía. Por lo tanto, un método eficiente de seguimiento de fase es necesario para detectar saltos en la misma y cambios abruptos en amplitud. En este trabajo se propone un método para fortalecer el seguimiento de fase basado en el proceso de envoltura de fase de un PLL (Phase Locked Loop) de segundo grado diseñado por software. El término 'envoltura' (*wrap*) se refiere a establecer los valores de fase de la señal de referencia en intervalos de π para que coincida con los valores obtenidos de la señal de salida del PLL (pulso de sincronía). Una técnica de transformación matemática del dominio del tiempo al dominio de la frecuencia es implementada con el fin de cuantificar el error de fase. La validez de la función de envoltura propuesta es verificada usando perturbaciones eléctricas.

Palabras clave: PLL de fase sencilla, SPLL, disturbio de fase, envoltura, transformada rápida de Fourier (FFT), error de fase

Introduction

Many problems and technical challenges still need to be addressed for the successful interconnection of generation systems. While using renewable energy (RES) with the electrical grid, the biggest challenge is the synchronization of the power inverter (DC/AC); the form of the generated voltage wave generated must be similar to that of the electrical grid, in order to guarantee continuous and stable operation (Jaalam, Rahim, Bakar, Tan, and Haidar, 2016). The phase angle of the utility voltage vector is basic information that allows increasing the number of power conditioning equipment connected to the utility grid, such as AC/DC converters (Arruda, Silva, and Filho, 2001).

The synchrony of the generated electricity is an adaptive process in which an internal reference signal formed by a control algorithm allows the output signal of the power inverter to operate synchronically with the fundamental component of the grid voltage. Jain, Jain, S., and Nema (2015) suggest that ideal synchrony occurs when the phase angle of the electrical grid is precisely followed, efficiently detecting disturbances and high harmonic components, and

responding quickly to changes. However, the phase angle may experience smooth or abrupt changes due to system conditions such as faults (Karimi, Khajehoddin, Jain, and Bakhshai, 2012).

[1]Electronic and comunications engineer, Instituto Tecnológico de estudios superiores de Monterrey, México. Master's degree in Engineering, Universidad Politécnica de Tulancingo, México. Affiliation: Professor, Universidad Politécnica de Tulancingo, México. E-mail: clementina.rueda@upt.edu.mx

[2]Electrical Engineer, Instituto Tecnológico de Tepic, México. Ph.D. Industrial Engineering, Universidad Autónoma del Estado de Hidalgo, México. Affiliation: Professsor, Universidad Politécnica de Tulancingo, México.
E-mail: ivan.rivas@upt.edu.mx

[3]B.Sc. in the area of automatic control, Alexandria University, Egipto. Ph.D. Safety Engineering, Okayama University, Japan. Affiliation: Associate Professor, University of Ontario Institute of Technology (UOIT), Canadá.
E-mail: Hossam.Gabbar@uoit.ca

[4]Electronics Engineer, Instituto Tecnológico de Tuxtla Gutiérrez, México. Ph.D. Electronics Engineer, Universidad Politécnica de Valencia, España. Affiliation: Professor, Universidad Politécnica de Tulancingo, México.
E-mail: humberto.arroyo@upt.edu.mx

Various algorithms have been proposed for the synchronization process. The simplest synchrony model is based on an open control loop which locates the zero crossings (ZCD) (Arulkumar, Vijayakumar, and Palanisamy, 2016). The zero crossing point is detected every cycle of the waveform. The disadvantage is that it is only used when the input signal is stable because it is unstable when there are transients and noise (Guo, Wu, and Gu, 2011). When a signal is periodic, the Fourier series can be used to calculate the magnitude and phase of the fundamental frequency (Ingale, 2014). The Fast Fourier Transform (FFT) has a good performance for estimating periodic signals in steady-state. However, this method is not optimal for the detection of sudden or rapid changes (Lee, Lee, J. P., Shin, Yoo, and Kim, 2014). The equivalent method in discrete time is the Discrete Fourier Transform (Xiao, Bai, Li, Liang, and Wang, 2014).

Sometimes, the power grid is subjected to disturbances and imbalances; for example, a phase jump occurs if a large load is connected suddenly, or due to a failure in the electrical grid (Valderrabano-González, Rosas-Caro, Tapia-Olvera, Beltrán-Carbajal, and Gómez-Ruiz, 2013). During this type of failure, the inverters are exposed to serious problems such as excessive DC link voltage and loss of grid voltage synchrony, among others. In order for an inverter to work properly, it is necessary for the control algorithm to be correctly adjusted to the characteristics of the electrical grid (Patil and Patel, 2016).

In applications where the power converters are connected to the electrical grid (Limongi, Bojoi, Pica, Profumo, and Tenconi, 2009), a synchronization technique based on a control subsystem called Phase-Locked Loop (PLL) is used. The concept of PLL was introduced in the 1930s for use in synchronous radio receptors (Khatana and Bhimasingu, 2017), which is essential to find the actual voltage-phase, magnitude on-line (Hoffmann et al., 2011), and phase angle of the electrical signal (Lee et al., 2014). A PLL is a closed-loop feedback control system, which synchronizes its output signal in frequency, as well as in phase, with the fundamental component of grid voltage (Golestan, Monfared, Freijedo, and Guerrero, 2012). However, in PLL techniques, phase and frequency are estimated within a single loop. This causes spurious frequency transients during phase angle changes. Such transients are reflected on the phase variable and cause a delay in the phase estimation and synchronization processes (Karimi et al., 2012).

In order to improve phase detection, research explains different techniques, for example, a new PLL structure for single-phase systems (Amuda, Cardoso Filho, Silva, S. M., Silva, S. R., and Diniz, 2000). The results show a follow-up of the disturbed input signal with a 30° phase jump. A circular limit cycle oscillator (CLO) coupled with frequency-locked loop (FLL) is proposed by Ahmed et al. (2019b), where a comparative analysis with an EPLL is performed using four test cases: non-smooth amplitude, phase, frequency, and DC bias jump; didn´t considerer harmonics, the results show a maximum phase error of 40° with a phase jump disturbance of 40°. A different option to the application is the use of an adaptive sliding mode observer for the estimation of frequency and phase. The results point to a good precision in the presence of non-smooth variations in phase, frequency, and amplitude (Ahmed et al., 2019a). Giampaolo, Barater, Tarisciotti, and Zanchetta (2014) propose a single-phase PLL with a Hilbert filter that allows the detection of rapid frequency variations or phase jumps in the grid voltage.

Conventional PLL algorithms fail under unbalanced conditions and rapid dynamic responses affecting their level of accuracy (Ahmed et al., 2019b). They usually operate correctly only when the range of frequency change is narrow and limited. Malfunctions of this type of PLL are a direct consequence of the phase detector and its blocking range; it only works well if the phase value is between $-\pi$ and π (Akoum and Farhang-Bouroujeny, 2007). A simple solution to improve the lock-in range is to increase the natural frequency or damping, but having a higher damping produces a longer lock-in time. For this reason, it is better to extend the range using a wrap method (Kumm, Klingbeil, and Zipf, 2010).

Wrapping algorithms play an important role because the values of phases acquired by different methods are directly limited to the ranges from $-\pi$ to π. The values of this range are known as wrapped phase. To reconstruct the natural phase values outside this range, a suitable wrapping phase algorithm can be used (Su and Chen, 2004).

A series of investigations are related to improving the lock-in range by means a wrapping algorithm. The EPLL (extended lock range) (Akoum and Farhang-Bouroujeny, 2007) is based on a PLL that includes a wrap process. The phase estimation $\varepsilon[n]$ is calculated using Equation (1), where the new phase angle is compared with the previous sample $\varepsilon[n-1]$. By tracking the phase increments and adding the appropriate multiples of 2π, it is possible to obtain an estimate of the phase value, improving the blocking range of the PLL.

$$\varepsilon[n] = \varepsilon[n] + 2\pi * \left(\frac{\varepsilon[n-1] - \varepsilon[n]}{2\pi} \right) \qquad (1)$$

In Kemao, Hoai Nam, Feng, and Hock Soon (2007) and Qudeisat, Gdeisat, Burton, and Lilley (2011), the wrap phase is extracted using the four quadrant arctangent operator. In another research (Kumm et al., 2010), two input signals with different frequency Δf and with initial phase value $\Delta\varphi_0$ are used to detect the phase angle: a complex signal (2) and a trigonometric relation signal (3). The trigonometric relation is a four quadrant inverse tangent (4).

$$\underline{x} = x_i + jx_q \qquad (2)$$

$$\varphi = \arctan\left(x_q/x_i\right) \pm \pi \qquad (3)$$

$$\Delta\varphi(n) = (2\pi\Delta f T_s n + \Delta\varphi_0)\,\text{modulo operation}\,(2\pi) \qquad (4)$$

For Δf positive values, the wrapping process assigns phase values in the range of 2π to 0 in each period, and, for negative Δf, the value range is from 0 to 2π. The phase difference is computed with Equation (5) and can be classified in different cases.

$$\Delta\psi(n) = \Delta\varphi(n) - \Delta\varphi(n-1) \qquad (5)$$

The wrap technique based on four quadrant inverse tangent is included as a phase detector within a PLL. In Kandeepan and Reisenfeld (2003, 2004), the performance to acquire a single frequency sinusoid with a four-quadrant phase detector (PD) based digital phase locked loop (DPLL) is analyzed with different tests and conditions. This system performs well with noisy signals. Regarding electrical systems, Miskovic, Blasko, Jahns, Lorenz, and Jorgensen (2018) propose a phase-locked loop (PLL) to synchronize a three-phase inverter with the electrical grid. This research includes a phase detector based on the four-quadrant inverse tangent function and also a PLL Error Unwrap algorithm in order to linearize the phase detector.

In the present work, a conventional single-phase synchronism system (PLL) is analyzed with an improvement in the tracking of the phase angle by means of wrapping phase algorithm, which responds adequately to the disturbances known as phase jumps. The document gives a brief review of the conventional PLL and a technical explanation of the proposed method that is referred to as a wrap PLL. It mainly focuses on presenting test simulations under various conditions, including the real scenarios of grid work; comparative validations are carried out to show the effectiveness of the proposed approach with respect to other basic synchronization methods.

Phase-Locked Loop

The conventional PLL is composed of a voltage controlled oscillator (VCO), a loop filter (LF), and a phase detector (PD) (Xu, Qian, Bian, Hu, and Xie, 2020). Normally, the PD is of the multiplier type, whose output consists of a DC term that has the phase information of the input signal and an AC term that should be filtered by the LF (Awad, Svensson, and Bollen, 2005). The transfer functions of its components are shown in the following Equations. In (6), the transfer function of the loop filter is observed, and in (7) that of the VCO is shown.

$$F(s) = \frac{1}{s} \frac{\tau_2 s + 1}{\tau_1} \qquad (6)$$

$$N(s) = \frac{k_0}{s} \qquad (7)$$

Where $F(s)$ refers to the filter transfer function, $N(s)$ is the VCO transfer function, and K_0 is the VCO gain.

The linearized analog PLL transfer function (Chung, Chien, Samueli, and Jain, 1993), is presented in Equation (8):

$$H(s) = \frac{k_d F(s) N(s)}{1 + k_d F(s) N(s)} \qquad (8)$$

K_d is the phase detector gain. Substituting (6) and (7) in (8) results in (9):

$$H(s) = \frac{2\zeta\omega_n s + \omega_n{}^2}{1 + k_d F(s) N(s)} \qquad (9)$$

To calculate the future angular frequency of a conventional second-order PLL (Best, 2007), Equation (10) is used:

$$\varphi_2(n + 1) = \varphi_2(n) + \left[\omega_0 + K_0.u_f(n)\right] T \qquad (10)$$

Where $\varphi_2(n+1)$ = Future angular frequency, $\varphi_2(n)$ = Current angular frequency, ω_0 = PLL center frequency, K_0 = VCO gain, $u_f(n)$ = output signal of the loop filter, and T = sampling period.

The result obtained by Equation(10) is not useful to carry out the Walsh method to generate a square pulse for synchrony (Rueda-Germán, Rivas-Cambero, Arroyo-Núñez, and Coyotl-Mixcoatl, 2019). Thus, a wrap method is required. The traditional wrap Equation (11) is based on the fact that, if the value of the future angular frequency ($\varphi_2(n + 1)$) is greater than π, it is reduced by 2π.

$$\varphi_2(n + 1) = \varphi_2(n + 1) - 2\pi \qquad (11)$$

After performing a simulation of the PLL using the traditional wrap method (11), the result is shown Figure 1a), where the PLL input signal is a sine wave with abrupt phase changes, and the output is a square signal (sync pulse). In Figure 1b), a high phase error is observed; the maximum value is close to π, and there is a loss of synchrony when the disturbance occurs.
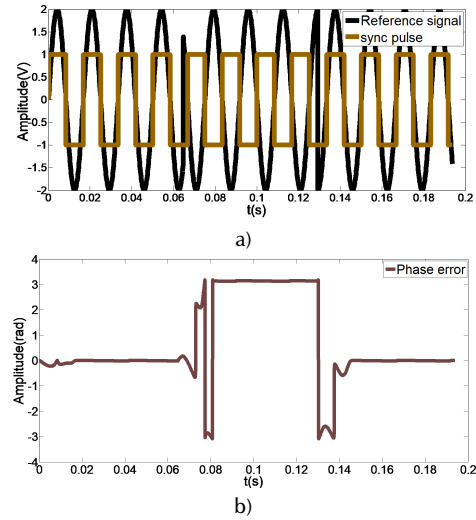
Figure 1. a) Reference signal, out-of-phase sync pulse b) phase error.
Source: Authors

Methodology

This work focuses on studying the operation of a wrap PLL proposal under strong phase jumps and other disturbances. Taking as reference the works of Akoum and Farhang-Bouroujeny (2007), Kumm *et al.* (2010), Hong-Yu and Yung-Chang (2017), Kandeepan and Reisenfeld (2003), and Miskovic *et al.* (2018), a single-phase synchronization system based on a second-order PLL is presented that includes a wrapping phase algorithm. The parts that constitute it are shown in Figure 2.

The reference signal (u_1) is a sine wave; the system input passes through a common phase detector, generating a phase error. Then, the phase error signal goes through a low-pass filter to eliminate the high frequency (Tiwari, R., Skone, Tiwari, S., and Strangeways, 2011). The output of the filter is the

input of the proposed wrap method (inverse tangent of four quadrants), and, finally, the VCO generates the equivalent frequency to track with the PLL input.
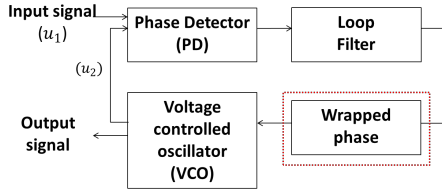
Figure 2. Second-level PLL with a wrapping phase algorithm.
Source: Authors

A multiplier is used as a phase detector, where the second input signal (u_2) in Equation (12) is a symmetrical square wave signal (Walsh function) generated by the VCO (Best, 2007).

$$u_2(t) = U_{20}\, \text{rect}(\omega_2 t + \theta_2) \tag{12}$$

Where rect is a square wave, U_{20} is the amplitude, ω_2 is the frequency value, and θ_2 is the phase. Using a series of mathematical considerations, the detector output signal u_d is:

$$u_d(t) \approx K_d \sin(\theta_e) \tag{13}$$

Where the phase error is $\theta_e = \theta_1 - \theta_2$, the detector gain is $K_d = \frac{2U_{10}U_{20}}{\pi}$, and U_{10} is the amplitude of u_1.

With $u_d(t)$ and a fixed sinusoidal signal, the inverse tangent of four quadrants is computed (Ukil, Shah, and Deck, 2011). This function returns values in the interval $[-\pi \text{ to } \pi]$ according to (14):

$$\text{Four-Quadrant Inverse Tangent } (y, x) = \begin{cases} \arctan\left(\frac{y}{x}\right) if(x > 0) \\ \pi + \arctan\left(\frac{y}{x}\right) if(y \geq 0, x < 0) \\ -\pi + \arctan\left(\frac{y}{x}\right) if(y < 0, x < 0) \\ \frac{\pi}{2} if(y > 0, x = 0) \\ -\frac{\pi}{2} if(y < 0, x = 0) \\ \text{undefined..if } (y = 0, x = 0) \end{cases} \tag{14}$$

To verify the effectiveness of this proposed wrap system, waveforms with different faults are simulated with Matlab. Two basic synchronization models are used to make the comparison: the zero crossing detector and the conventional PLL. The Fast Fourier Transform (FFT) function that calculates the DFT is applied to find the phases and display the phase error.

Results

The PLL input is a constant amplitude sine wave (15), where the value of the phase angle is modified to generate a phase jump disturbance. The processing algorithm considers the following parameters: 2V sinusoidal reference signal amplitude, 8 000 Hz sampling frequency, and 376,9911 rad/s center frequency.

$$v = v_p \sin(2\pi f t \pm \theta) \tag{15}$$

v_p = Amplitude (V), f = Frequency (Hz), θ = Phase angle (Radians).

The first case is a sinusoidal type reference signal with a phase jump of 180° that is approximately 0,1 seconds, as shown in Figure 3 a). The same figure also shows the behaviors of the output signals of the proposed PLL (continuous orange line) and of the conventional PLL (dotted brown line). Before the disturbance, both square signals (sync pulses) are in tune. When the phase jump occurs, only the sync pulse produced by this proposed model remains in phase and frequency with the reference signal (black signal). To show the phase error, the FFT function is used. The phase values are observed in Figure 3 b), taking a period to obtain the data window for the FFT processing in all tests. For this reason, a phase error is shown at the beginning of the graphs. It is worth mentioning that the Gibbs effect was not considered in the results. As shown in Figure 3 c), by subtracting the values obtained through the FFT, we have the phase error of the proposed PLL, which is close to zero (continuous orange line), while the conventional PLL phase error (dotted brown line) increases after the disturbance.

a)

b)

c)
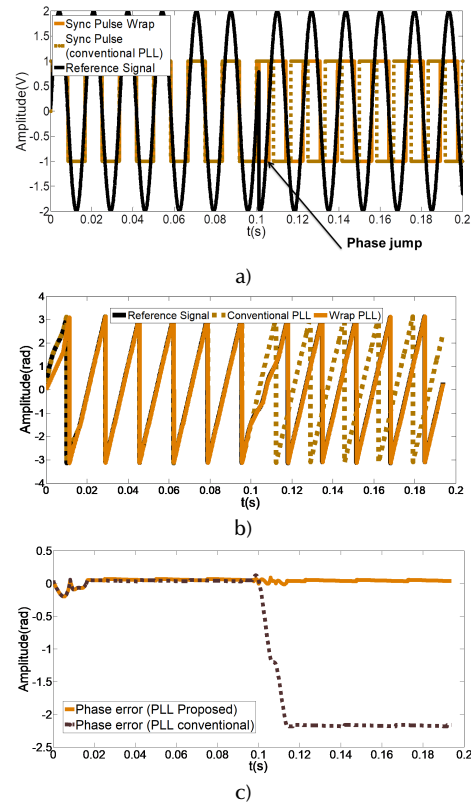
Figure 3. a) Synchrony pulse of the proposed model compared to a conventional PLL. b) Reference signal phase and sync signals phase using FFT. c) Phase error obtained from the phase comparison between the input signal and the synchronization pulses (Wrap PLL and convectional PLL).
Source: Authors

The second case is a signal that contains multiple extreme phase jumps, which is shown in Figure 4 a) in order to evaluate the effectiveness of the wrap PLL phase tracking. The phase error is close to zero as seen in Figure 4 b); the synchrony remained with the reference signal.
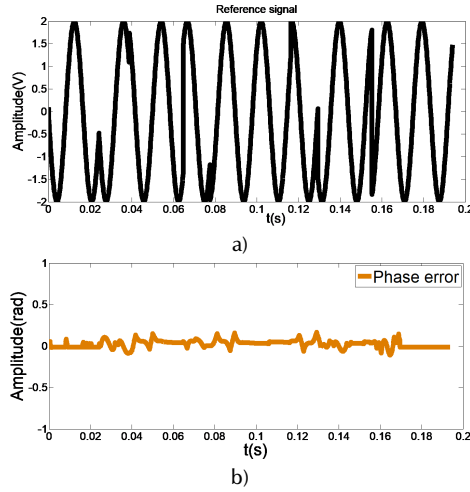
Figure 4. a) Reference signal with different phase jumps b) Phase error obtained from sync pulse (Wrap stocktickerPLL) and reference signal.
Source: Authors

With the third test case, the effectiveness of this proposed PLL is verified. The input signal (continuous black line) refers to the behavior of the power line. This is shown in Figure 5 a), where the output signal or synchronization pulse (square signal) is also observed. Synchrony is lost only for an instant of time (close to 0,08 s) and then resynchronizes even when disturbances are evident. The maximum phase error is 0,061 (rad) and it takes 0,4025 s for the PLL to lock in, as shown in Figure 5 b).

Figure 5. a) Electrical disturbances and pulse in synchrony. b) Phase error.
Source: Authors

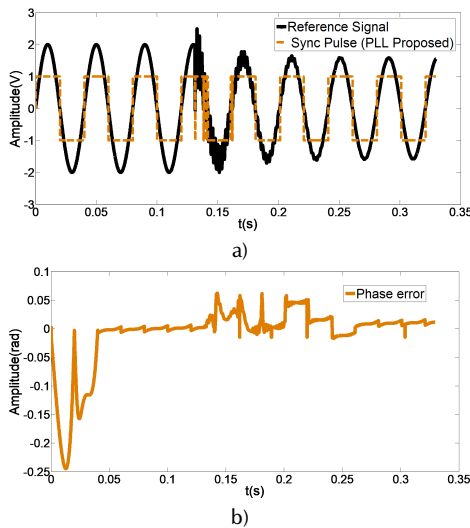Harmonics are the main disturbance in the electrical system (Senthilnathan, Annapoorani, and Ravi, 2018). Furthermore,

voltage variations, such as sag and swell conditions, occur due to fault and utilization of sensitive loads (Damaraju and Lalitha, 2015). The proposed method is tested in a fourth case with a signal containing a series of disturbances. Details of the test scenarios are given in Table 1.

Table 1. Test conditions

Time (s)	Disturbance type	Frequency (Hz)	Phase(rad)
0	No disturbance	60 Hz	0
0,99	Phase jump	60 Hz	-2,473
0,1065	Harmonics	60 Hz	-2,473
0,1801	Voltage loss	0 Hz	0
0,2409	Phase jump	60 Hz	-1,051
0,2799	Phase Jump	50 Hz	-0,2529
0,2805	Phase Jump	60 Hz	0,4523
0,3468	Phase Jump	60 Hz	2,516

Source: Authors

The experimental results of the synchronization pulses generated by the conventional PLL method and by the zero crossing detector are observed in Figure 6 a). The three methods are tuned with the sinusoidal signal without disturbances during the first seconds. When the harmonics begin, only two signals remain in tune: the synchronization pulse of the ZCD and that of the PLL with the wrap method. In the voltage drop, the ZCD sync pulse loses tune. The phase error results obtained from each of the synchrony methods are shown in Figure 6 b). The error is close to zero in the proposed Wrap PLL method.
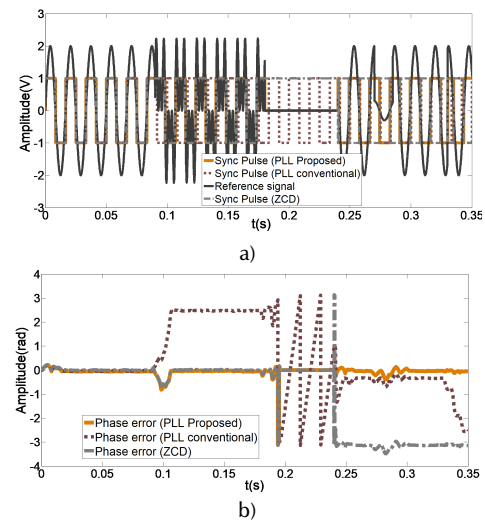
Figure 6. a) Synchronous pulses comparison with different methods, b) Three methods phase error.
Source: Authors

The summary of the results for the three analyzed synchrony methods is shown in Table 2. The proposed PLL significantly outperformed conventional PLL and ZCD most of the time. The PLL method proposed in this article remains synchronized despite the different disturbances, which is not the case with conventional PLL and ZCD.

Table 2. Summary of the results

Time (s)	Max phase error (rad)		
	Wrap-PLL	**CLASSICAL PLL**	**ZCD**
0	0	0	0
0,99	0,7762	0,4492	0,7465
0,1065	0,02962	2,432	0,022
0,1801	0,0569	2,617	0,009
0,1945	3,125	3,125	2,93
0,2409	0,0868	0,9657	3,102
0,2799	0,1171	0,3855	3,212
0,2805	0,2018	0,5066	3,296
0,3468	0,06184	2,563	3,14
State	**Remain in synchrony**	**Loss synchrony**	**Loss synchrony**
Max. settling time (s) during disturbances	0,0476	-	-

Source: Authors

Conclusions

An alternative synchronization method was presented as a proposal for grid connected systems, based on a model to improve the wrap process in a second-degree PLL. The results obtained were compared with a synchrony system based on a conventional PLL and ZCD, showing that the proposed PLL has a better tuning against phase disturbances. The synchrony capability is highlighted and verified by FFT. The performance of the proposed PLL is superior in comparison with the other techniques. This work contributes as a reference for the process of synchronization of the electrical power systems with the electrical grid, even when there are phase jumps. The results enable the possibilities for future testing by implementing this model on a real-time processor.

Acknowledgements

References

Ahmed, H., Amamra, S., and Salgado, I. (2019a). Fast Estimation of Phase and Frequency for Single-Phase Grid Signal. *IEEE Transactions on Industrial Electronics*, 66(8), 6408-6411. 10.1109/TIE.2018.2860567

Ahmed, H., Amamra, S., and Bierhoff, M. (2019b). Frequency-Locked Loop-Based Estimation of Single-Phase Grid Voltage Parameters. *IEEE Transactions on Industrial Electronics, 66*(11), 8856-8859. 10.1109/TIE.2018.2873527

Akoum, S. and Farhang-Bouroujeny, B. (2007). *A phase locked loop with arbitrarily wide lock range for software defined radios*. Paper presented at the 2007 Software Defined Radio Technical Conference, November 5-9, 2007, Denver, Colorado.

Amuda, L. N., Cardoso Filho, B. J., Silva, S. M., Silva, S. R., and Diniz, A. S. A. C. (2000). Wide bandwidth single and three-phase PLL structures for grid-tied PV systems. In IEEE (Eds.) *Conference Record of the Twenty-Eighth IEEE Photovoltaic Specialists Conference* (pp. 1660-1663). New York, NY: IEEE. 10.1109/PVSC.2000.916220

Arruda, L. N., Silva, S. M., and Filho, B. J. C. (2001). PLL structures for utility connected systems. In IEEE (Eds.) *Conference Record of the 2001 IEEE Industry Applications Conference. 36th IAS Annual Meeting* (vol. 4, pp. 2655-2660). New York, NY: IEEE. 10.1109/IAS.2001.955993

Arulkumar, K., Vijayakumar, D., and Palanisamy, K. (2016). Recent advances and control techniques in grid connected PV system–A review. *International Journal of Renewable Energy Research (IJRER), 6*(3), 1037-1049. https://www.ijrer.org/ijrer/index.php/ijrer/article/view/4075

Awad H., Svensson, J., and Bollen, M. J. (2005). Tuning software phase-locked loop for series-connected converters. *IEEE Transactions on Power Delivery, 20*(1), 300-308, Jan. 2005, 10.1109/TPWRD.2004.837823

Best, R. E. (2007). *Phase locked loops: design, simulation, and applications*. New York, NY: McGraw-Hill Professional.

Chung, B.-Y., Chien, C., Samueli, H., and Jain, R. (1993). Performance analysis of an all-digital BPSK direct-sequence spread-spectrum IF receiver architecture. *IEEE Journal on Selected Areas in Communications, 11*(7), 1096-1107. 10.1109/49.233222

Damaraju, R. and Lalitha, S. V. N. L. (2015). A fuzzy controller for compensation of voltage sag/swell problems using reduced rating dynamic voltage restorer. *Indian Journal of Science and Technology, 8*(23), 1-6. 10.17485/ijst/2015/v8i23/71858

Giampaolo, B., Barater, D., Tarisciotti, L., and Zanchetta, P. (2014). High-dynamic single-phase Hilbert-based PLL for improved phase-jump ride-through in grid-connected inverters. In IEEE (Eds) *2014 IEEE Energy Conversion Congress and Exposition* (*ECCE*)(pp. 4932-4939). New York, NY: IEEE. 10.1109/ECCE.2014.6954077

Golestan, S., Monfared, M., Freijedo, F. D., and Guerrero, J. M. (2012). Design and Tuning of a Modified Power-Based PLL for Single-Phase Grid-Connected Power Conditioning Systems. IEEE Transactions on Power Electronics, 27(8), 3639-3650, 10.1109/TPEL.2012.2183894

Guo, X. Q., Wu, W. Y., and Gu, H. R. (2011). Phase locked loop and synchronization methods for grid-interfaced converters: a review. *Przeglad Elektrotechniczny, 87*(4), 182-187. http://pe.org.pl/articles/2011/4/48.pdf

Hoffmann, N., Lohde, R., Fischer, M., Fuchs, F. W., Asiminoaei L., and Thøgersen, P. B. (2011). A review on fundamental grid-voltage detection methods under highly distorted conditions in distributed power-generation networks. In IEEE (Eds) *2011 IEEE Energy Conversion Congress and Exposition* (pp. 3045-3052). New York, NY: IEEE. 10.1109/ECCE.2011.6064179

Hong-Yu, L. and Yung-Chang Y. (2017). Efficient four-quadrant carrier frequency offset tracking for OFDM. *Journal of the Chinese Institute of Engineers, 40*(6), 547-550. 10.1080/02533839.2017.1356693

Ingale, R. (2014). Harmonic Analysis Using FFT and STFT. *International Journal of Signal Processing, Image Processing and Pattern Recognition, 7*(4) 345-362. 10.14257/ijsip.2014.7.4.33

Jaalam, N., Rahim, N. A., Bakar, A. H. A., Tan, C., and Haidar, A. M. (2016). A comprehensive review of synchronization methods for grid-connected converters of renewable energy source. *Renewable and Sustainable Energy Reviews, 59*, 1471-1481. 10.1016/j.rser.2016.01.066

Jain, B., Jain, S., and Nema, R. K. (2015). Control strategies of grid interfaced wind energy conversion system: An overview. *Renewable and Sustainable Energy Reviews, 47*, 983-996. 10.1016/j.rser.2015.03.063

Kandeepan, S. and Reisenfeld, S. (2003). Frequency tracking and acquisition with a four-quadrant arctan phase detector based digital phase locked loop. In IEEE (Eds) *Fourth International Conference on Information, Communications and Signal Processing, 2003 and the Fourth Pacific Rim Conference on Multimedia. Proceedings of the 2003 Joint* (vol.1, pp. 401-405). New York, NY: IEEE. 10.1109/ICICS.2003.1292483

Kandeepan S. and Reisenfeld S. (2004). Acquisition performance of a digital phase locked loop with a four-quadrant arctan phase detector. In IEEE (Eds) *Proceedings of 2004 International Symposium on Intelligent Signal Processing and Communication Systems* (pp. 648-653). New York, NY: IEEE. 10.1109/ISPACS.2004.1439139

Karimi Ghartemani, M., Khajehoddin, S. A., Jain, P. K., and Bakhshai, A. (2012). Problems of Startup and Phase Jumps in PLL Systems. *IEEE Transactions on Power Electronics, 27*(4), 1830-1838. 10.1109/TPEL.2011.2169089

Khatana, V. and Bhimasingu, R. (2017). Review on Three-Phase PLLs for Grid Integration of Renewable Energy Sources. In IEEE (Eds) *2017 14th IEEE India Council International Conference* (*INDICON*) (pp. 1-6). New York, NY: IEEE. 10.1109/INDICON.2017.8488071

Kemao, Q., Hoai Nam, L. T., Feng, L., and Soon, S. H. (2007). Comparative analysis on some filters for wrapped phase maps. *Applied Optics, 46*(30), 7412-7418. 10.1364/AO.46.007412

Kumm, M., Klingbeil, H., and Zipf, P. (2010). An FPGA-based linear all-digital phase-locked loop. *IEEE Transactions on Circuits and Systems I: Regular Papers, 57*(9), 2487-2497. 10.1109/TCSI.2010.2046237

Lee, K. J., Lee, J. P., Shin, D., Yoo, D. W., and Kim, H. J. (2014). A novel grid synchronization PLL method based on adaptive low-pass notch filter for grid-connected PCS. *IEEE Transactions on Industrial Electronics, 61*(1), 292-301. 10.1109/TIE.2013.2245622

Limongi, L. R., Bojoi, R., Pica, C., Profumo, F., and Tenconi, A. (2007). Analysis and Comparison of Phase Locked Loop Techniques for Grid Utility Applications. In IEEE (Eds) *2007 Power Conversion Conference - Nagoya* (pp. 674-681) 10.1109/PCCON.2007.373038

Miskovic, V., Blasko, V., Jahns, T. M., Lorenz, R. D., and Jorgensen, P. M. (2018). Linear Phase-Locked Loop. In IEEE (Eds) *2018 IEEE Energy Conversion Congress and Exposition* (*ECCE*) (pp. 5677-5683). New York, NY: IEEE. 10.1109/ECCE.2018.8558259

Patil, K. R. and Patel, H. H. (2016). Modified Dual Second-order Generalized Integrator FLL for Frequency Estimation Under Various Grid Abnormalities. *Transactions on Environment and Electrical Engineering, 1*(4), 10-18. 10.1109/EEEIC.2016.7555824

Qudeisat, M., Gdeisat, M., Burton, D., and Lilley, F. (2011). A simple method for phase wraps elimination or reduction in spatial fringe patterns. *Optics Communications, 284*(21), 5105-5109. 10.1016/j.optcom.2011.07.024

Rueda-Germán, C., Rivas-Cambero, I. J., Arroyo-Núñez, J. H., and Coyotl-Mixcoatl, F. (2019). Implementation of a phase tuner for exchange of electrical energy. In IEEE (Eds) *2019 IEEE International Autumn Meeting on Power, Electronics and Computing* (*ROPEC*) (pp. 1-5). New York, NY: IEEE. 10.1109/ROPEC48299.2019.9057059

Senthilnathan, K., Annapoorani, I., and Ravi, S. (2018). Simulation and Hardware Implementation of Shunt Active Power Filter Based on Synchronous Reference Frame Theory. *TELKOMNIKA, 16*(1), 1-9. 10.12928/telkomnika.v16i1.6524

Su, X. and Chen, W. (2004). Reliability-guided phase unwrapping algorithm: a review. *Optics and Lasers in Engineering, 42*(3), 245-261. 10.1016/j.optlaseng.2003.11.002

Tiwari, R., Skone, S., Tiwari S., and Strangeways, H. J. (2011). WBMod assisted PLL GPS software receiver for mitigating scintillation affect in high latitude region. In IEEE (Eds) *2011 XXXth URSI General Assembly and Scientific Symposium* (pp. 1-4). New York, NY: IEEE. 10.1109/URSIGASS.2011.6050861

Ukil, A., Shah, V. H., and Deck, B. (2011). Fast computation of arctangent functions for embedded applications: A comparative analysis. In IEEE (Eds) *2011 IEEE International Symposium on Industrial Electronics* (pp. 1206-1211) 10.1109/ISIE.2011.5984330

Valderrabano-Gonzalez, A., Rosas-Caro, J. C., Tapia-Olvera, R., Beltrán-Carbajal, F., and Gómez-Ruiz, J. F. (2013). Single phase angle tracking method for power switches gating synchronization. *Electric Power Systems Research, 105*, 88-94. 10.1016/j.epsr.2013.07.015

Xiao, J., Bai, L., Li, F., Liang, H., and Wang, C. (2014). Sizing of energy storage and diesel generators in an isolated microgrid using discrete Fourier transform (DFT). *IEEE Transactions on Sustainable Energy, 5*(3), 907-916. 10.1109/TSTE.2014.2312328

Xu, J., Qian, H., Bian, S., Hu, Y., and Xie, S. (2020). Comparative study of single-phase phase-locked loops for grid-connected inverters under non-ideal grid conditions. *CSEE Journal of Power and Energy Systems, 1*, 1-10. 10.17775/CSEEJPES.2019.02390

Energy Management Electronic Device for Islanded Microgrids Based on Renewable Energy Sources and Battery-Based Energy Storage

Dispositivo electrónico de gestión de energía para microrredes aisladas basadas en recursos energéticos renovables y almacenamiento de energía basado en baterías

Elkin D. Granados[1], Nelson L. Díaz[2], and Adriana C. Luna[3]

ABSTRACT

Energy management systems are one of the most important components in the operation of an electric microgrid. They are responsible for ensuring the supervision of the electrical system, as well as the coordination and reliability of all loads and distributed energy resources in order for the microgrid to be operated as a unified entity. Because of that, an energy management system should be fast enough at processing data and defining control action to guarantee the correct performance of the microgrid. This paper explores the design and implementation of an energy management system deployed over a dedicated electronic device. The proposed energy management device coordinates the distributed energy resources and loads in a residential-scale islanded microgrid, in accordance with a rule-based energy management strategy that ensures reliable and safe operation of the battery-based energy storage system. A hardware-int-he-loop test was performed with a real-time simulation platform to show the operation of the electronic device.

Keywords: energy management system, hardware in the loop, microgrid, single-board computer

RESUMEN

Los sistemas de gestión de energıa son uno de los componentes más importantes en la operación de las microrredes eléctricas. Son responsables de asegurar la supervisión del sistema eléctrico, además de la confiabilidad y coordinación de todas las cargas y los recursos energéticos distribuidos, de tal forma que la microrred pueda ser operada como una entidad unificada. Debido a esto, un sistema de gestión de energıa debe ser lo suficientemente rápido para procesar un gran número de datos y definir las acciones de control para garantizar el correcto funcionamiento de la microrred. Este documento explora el diseño e implementación de un sistema de gestión de energıa desplegado sobre un dispositivo electrónico dedicado. El dispositivo de gestión de energıa propuesto coordina las cargas y los recursos energéticos distribuidos en una microrred aislada a escala residencial de acuerdo a un sistema de gestión de energıa basado en reglas que asegura una operación confiable y segura del sistema de almacenamiento de energıa basado en baterıas. Se realizó una prueba de hardware en el lazo de control usando una plataforma de simulación en tiempo real para demostrar la operación del dispositivo electrónico.

Palabras clave: sistema de gestión de energıa, hardware en el lazo, microrred, computador de placa única

[1]Electronics Engineer, Universidad Distrital Francisco José de Caldas, Colombia. Affiliation: master student on engineering at Universidad Distrital Francisco José de Caldas, Colombia. E-mail: edgranadosh@correo.udistrital.edu.co

[2]Electronics Engineer, Universidad Distrital Francisco José de Caldas, Colombia. M.Sc. Industrial Automation, Universidad Nacional de Colombia, Colombia. Ph.D. in Energy Technology Aalborg University, Denmark. Affiliation: Associate Professsor, Universidad Distrital Francisco José de Caldas, Colombia. E-mail: nldiaza@udistrital.edu.co

[3]Electronics Engineer, Universidad Nacional de Colombia, Colombia. M.Sc. in Indrustial Automation, Universidad Nacional de Colombia, Colombia. Ph.D. in Energy Technology Aalborg University, Denmark. Affiliation: Faculty of Mechanical, Electronics, and Biomedical Engineering, Universidad Antonio Nariño, Colombia. E-mail: aluna10@uan.edu.co

Introduction

Increasing energy requirements, along with a general concern about global warming caused by the use of conventional energy sources based on fossil fuels, have triggered the use of renewable energy sources (RES) (Keyhani, 2016). Particularly, RESs based on photovoltaic (PV) and wind turbine (WT) generation units have been playing an important role, due to their availability and easy integration by means of power electronics conversion stages (Teodorescu, Liserre, and Rodriguez, 2010). Nevertheless, PV and WT generation are characterized by their high variability and dependence on weather conditions, which make it difficult to control and regulate the amount of power obtained (Jurasz, Mikulik, and Krzywda, 2017). Because of that, energy storage systems appear as a viable option to compensate the variability of the RESs (Beaudin, Zareipour, Schellenberg, and Rosehart, 2015).

Mainly, energy storage systems (ESS) based on batteries have become the most reliable option to complement the operation of variable RESs since, in general, batteries have a good commitment between power density, for compensating quick changes in the generation profiles, and provide energy density to ensure back up of energy, for supporting the power balance in the electrical system.

Through the integration of distributed RESs, ESSs, and loads as shown in Figure 1, it is possible to configure an islanded microgrid in which all distributed energy resources should operate coordinately, governed by an energy management system (EMS) in order to ensure the reliability of the islanded power system and support the load requirements (de Matos, e Silva, and Ribeiro, 2015). In the microgrid, the EMS is responsible of defining and providing proper control commands to all distributed energy resources, in accordance with predefined strategies or control objectives that range from simple rule-based or reactive methods, to more complex ones based on optimization, or even hybrid methods based on the combination of the former two (Luna, 2016; Rafique and Jianhua, 2018; Hofman, Steinbuch, van Druten, and Serrarens, 2006). Therefore, the EMS becomes an important component of the microgrid, which should be able to perform complex operation with high processing speed, have enough capability for data storing and processing, and rely on communication modules for the integration with other components of the microgrid (Al sumaiti, Ahmed, and Salama, 2014). In spite of this, the EMS comprises different components by itself, such as sensors, smart metering infrastructure, communication channels, the device itself, and the embedded software. In particular, the development of the last two have been of interest for different manufacturers in order to obtain a more compact and efficient embedded on-chip-based system (Al sumaiti, Ahmed, and Salama, 2014; Liu, Qiu, Fan, Zhu, and Han, 2016).
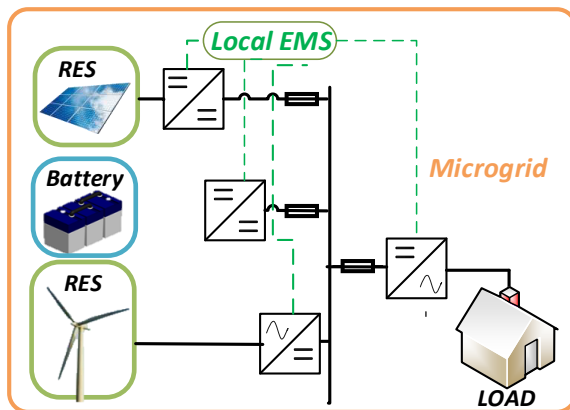
Figure 1. Islanded microgrid configuration based on RESs.
Source: Authors

In order to validate the performance of a designed EMS device, it is possible to use dedicated test platforms in which microgrid behavior, power electronic devices, and primary controllers can be simulated in real-time, while the physical hardware, where the EMS and control actions are embedded, is integrated into a closed-loop in order to emulate a real

interaction with the microgrid (Casolino, Russo, Varilone, and Pescosolido, 2018; Wang, Nguyen, Xu, and Shi, 2020). These kinds of experimental platforms are defined as hardware-in-the-loop (HIL) and are commonly used an accepted for the validation of control and management strategies in a real hardware environment (IEEE, 2018). HIL allows a rapid prototyping and performance test of the electronic device by emulating the behavior under real conditions without complex lab setups (Montoya et al., 2020; Estrada, Vázquez, Vaquero, de Castro, and Arau, 2020; Sun et al., 2020).

For an islanded, RES-based residential microgrid based, variability in power generation and consumption is not the only fact to consider within the operation of the power system. As a matter of fact, the operation of the battery-based ESS is critical for an islanded microgrid due to its capacity for storing or releasing energy. Hence, the ESS unit commonly assumes the responsibility of regulating the balance between generation and consumption, and, consequently, the regulation of the local power system (Pecas Lopes, Moreira, and Madureira, 2006). Therefore, it is important to consider the limitations and requirements on the operation of the battery-based ESS, since they cannot store an infinite amount of energy and they have important limitations within their operation that should be considered. Particularly, Li-ion batteries and Lead-Acid batteries are the most used in islanded power systems such as microgrids, since they offer a good commitment between deep-cycle and lifespan (Beaudin, Zareipour, Schellenberg, and Rosehart, 2015). On top of that, it is important to consider that those kind of batteries are voltage-limiting devices whose operation limits should not overcome certain typical maximum and minimum boundaries defined by the manufactures under risk of degradation or damage (Battery University, n.d.; Buchmann, 2016). Here is where the coordination and energy management system becomes crucial for the operation of the microgrid; based on this information, a rule-based EMS can be considered for ensuring the proper dispatch and transitions between different states an operation modes of the microgrid (IEEE, 2017).

Several approaches have been proposed for a proper coordination and energy management of distributed energy resources in microgrids in the search for a proper operation of the ESSs within safe ranges (Kim, et al., 2010; Mahmood, Michaelson, and Jiang, 2015; Mao, Huang, and Chang, 2013). Particularly, in Díaz, Luna, Vázquez, and Guerrero (2017), a centralized coordination strategy based on the definition of simple supervisory stages was previously proposed. This strategy was deployed in a laboratory text platform where it showed to be effective at ensuring the regulation of the islanded electrical power system and keeping the ESS within safe operation values.

In accordance with the aforementioned, this article presents the design and implementation of an electronic device that acts as an EMS for a residential-scale isolated microgrid based on variable RESs and a battery-based energy storage system, as shown in Figure 1. Given that the EMS will act as a central control unit, it must take into account the variability of renewable resources together with the loads and execute a

management algorithm to ensure the reliability of the isolated energy system. In order to test the electronic device, a simple rule-based management strategy, already presented by Díaz *et al.* (2017), is embedded into the EMS device. In the following sections, the rule-based management strategy will be outlined for an isolated microgrid whose model has been implemented on a real-time simulation platform (OP4510). Next, based on the requirements derived from the simulation, the design and implementation of the electronic device that will act as EMS are explained. For the validation of the device, the HIL method will be used, connecting the EMS to the ports of the real-time simulation platform OPAL® OP4510. Finally, the results obtained from the validation will be presented.

Rule-based Management Strategy

Figure 1 shows the basic structure of the islanded microgrid considered for this application. The microgrid has a DC configuration in order to avoid dealing with problems of reactive power and frequency regulation within the model. The microgrid consists of a hybrid PV-WT generation unit, an ESSs based on batteries, and AC loads integrated through a DC/AC conversion stage. Commonly, ESSs are responsible for ensuring the power balance and the regulation of the common bus in the local power grid. Meanwhile, RESs are more likely to operate as power sources at their maximum power point in order to harvest the maximum amount of available energy. Since ESSs have limited storage capacity, overcharge and over-discharge should be avoided to prevent degradation of the storage units. Since, for islanded applications, Lead-acid and Li-ion batteries are the most used technologies, it is important to consider that they are voltage-limiting devices. Because of that, their operation limits are defined by voltage levels, whose maximum value (V_{max}) roughly corresponds to a 90% of the state of charge (SoC), while the minimum (V_{min}) roughly corresponds to a 20% of the SoC (Marra and Yang, 2015).

Description of the desired operation

Figure 2 shows the desired profile for the operation of a battery. In this Figure, three stages or operation modes can be identified. The first stage corresponds to a normal charge or discharge of the battery within safe operating limits. In this stage (S1), called MODE I from now on, the battery will absorb or inject power in accordance with the difference between generation and consumption. Because of that, the battery will be charged or discharged. The second stage corresponds to the moment in which the battery has reached its maximum charge limit, defined by V_{max}. This stage will be called MODE II. Here, the charge of the battery should be stopped in order to overpass the maximum voltage limit. Finally, the third stage is when the battery reaches its minimum voltage threshold an then the discharge should be stopped. This this stage is called MODE III.

In light of the above, the operation of the islanded microgrid should be complemented by a management strategy that keeps the operation of the battery within safe regions. As mentioned before, the ESS is responsible for the regulation of
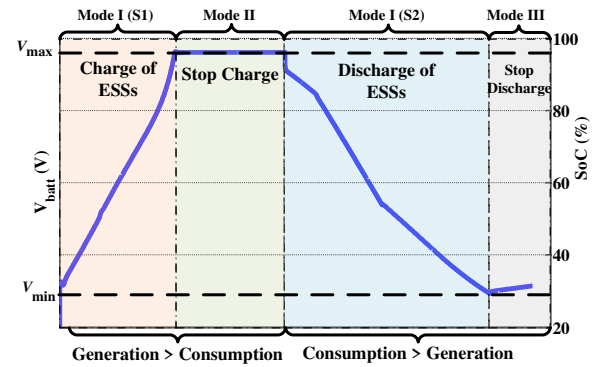
Figure 2. Desired operation Profile for the battery in the islanded microgrid.
Source: Authors

the islanded power grid. Therefore, it will operate in voltage control mode, defining the voltage level of the islanded power grid. Then, the battery will be charged when the generation is larger than consumption or discharged in the opposite case. When the battery reaches its maximum level of operation, the ESS will not be able to continue absorbing energy and charging the battery. For that reason, an active power curtailment of RES generation is considered when the battery reaches its maximum voltage in such a way that the generation from PV (P_{PV}), and WT (P_{WT}) is balanced with the consumption (P_{Load}).

$$P_{Load} = P_{PV} + P_{WT} \tag{1}$$

The power curtailment of each RES unit can be defined proportionally to its maximum available power ($P_{PV_{MP}}$) and ($P_{WT_{MP}}$), which can be obtained from maximum power point tracking methods such as the one presented by Trujillo Rodríguez, Díaz Aldana, and Hernández Mora (2015) and Patsios Chaniotis, Rotas, and Kladas (2009) for PV and WT, respectively. Thus, Equation (1) can be rewritten as:

$$P_{Load} = \alpha_{PV} * P_{PV_{MP}} + \alpha_{WT} * P_{WT_{MP}} \tag{2}$$

where (α_{PV}) and (α_{WT}) are defined as the curtailment indexes for PV and WT, respectively, which should be calculated in the EMS responsible for the management strategy. In order to have a contribution of each RES in proportion to its maximum available power ($P_{RES_{MP}}$), the following condition is established:

$$\frac{P_{PV_{MP}}}{\alpha_{PV}} = \frac{P_{WT_{MP}}}{\alpha_{WT}} \tag{3}$$

Otherwise, when generation is less than consumption, the battery will be discharged until it reaches its minimum voltage level. In this case, the option is to disconnect the load unless there is another dispatchable source available that can supply the load. Once the load has shed, the battery will be charged in accordance to the generation from RES.

Operation modes

In accordance with the operation modes described above, it is possible to define a finite state machine (FSM) programmed into the energy management system, which coordinates the operation of the distributed energy resources within the islanded microgrid. The states in the FSM correspond to the operation modes, described as:

- *Mode I*: The ESSs is charged (S1) or discharged (S2) based on the imbalance between supply and demand.

- *Mode II*: The ESS is fully charged and the power generation should be curtailed to avoid overcharge. The curtailment index is calculated.

- *Mode III*. The ESS reaches its minimum charge levels of charge and the load should be disconnected to avoid over-discharge.

The transitions between states or operation modes are defined by discrete events:

- *From Mode I to Mode II*: The battery voltage (V_{batt}) reaches its maximum value (V_{max}).

- *From Mode II to Mode I*: The maximum available generation from RES becomes less than the load consumption ($P_{Load} < P_{PV_{MP}} + P_{WT_{MP}}$)

- *From Mode I to Mode III*: The battery voltage (V_{batt}) reaches its minimum value (V_{max}).

- *From Mode III to Mode I*: The SoC of the battery reaches a value of 50%.

Microgrid Simulation

The microgrid model has been built in Simulink, where two 24-hour PV and WT generation profiles will be used with data sampled in 5-minute periods and two 24-hour load profiles with data sampled every hour. Since the battery operation is one of the most important issues to consider in the operation of the microgrid, a detailed model of a Li-ion battery, able to emulate the internal losses and the slow and fast dynamics, has been used as proposed in Kim and Qiao (2011). The RESs are modeled and controlled as power sources; they are able to provide a generation profile. Meanwhile, the load has been modeled as an inverter controlled as a power load. The SoC is estimated by the commonly used ampere-hour (Ah) counting method as:

$$SoC(t) = SoC(0) - \int_0^t \eta_{batt} * \frac{I_{batt}(\tau)}{C_{bat}} d\tau \qquad (4)$$

where $SoC(0)$ is the initial SoC, C_{bat} is the capacity in ($A \cdot h$), η_{batt} is the charging/discharging efficiency, and $I_{batt}(\tau)$ is the instantaneous current in the battery.

To avoid running the simulation during the full 24-hour period, its time has been scaled. Therefore, a real hour corresponds to 12 seconds in the simulation. Thus, the shortest period of change in values corresponds to 5 minutes of the generation profiles, which in the simulation corresponds to 1 second. In order to warn EMS that there was a change in the microgrid, a digital square signal with a period of 0,5 seconds will be generated for synchronization. With this, at least two values will be processed by the EMS before a change occurs in the simulation.

The Simulink-based microgrid model has been embedded in the OPAL® OP4510 real-time simulation platform. Therefore, by taking advantage of the analog and digital input and output ports of the OP4510, it is possible to have a real interaction with external devices. The embedded microgrid model provides measured variables such as the instantaneous power output of the PV and WT generators ($P_{PV_{MP}}$ and $P_{WT_{MP}}$), the state of charge of the battery (SoC), the battery voltage (V_{batt}), and the power consumed by the load (P_{Load}) through analog outputs. Also, external control instruction can be received by the microgrid, such as the curtailment indexes of the two generators(α_{PV} and α_{WT}) through analog inputs, and the on/off control signal for the load through a digital input, as well as generating a synchronization signal to enable the communication with external devices through a digital output. Table 1 summarizes the input and output ports used for the interaction with the microgrid.

Table 1. Input/Output Ports Real-time Simulation Platform

| Type of ports	Number	Variables
Analog Outputs	5	$(P_{PV_{MP}})$, $(P_{WT_{MP}})$, SoC, (V_{batt}), and (P_{Load})
Analog Inputs	2	(α_{PV}) and (α_{WT})
Digital Input	1	on/off signal for the load
Digital Output	1	Synchronization

Source: Authors

The model defined for the rule-based management strategy requires the energy management device to perform mathematical operations such as solving a system of equations composed by Equation (2) and (3), which allow obtaining the curtailment indexes of the generators when the microgrid operates in MODE II. In addition, the energy management device should be able to capture and generate both analog and digital signals for proper interaction with the simulation platform.

EMS Device Design and Operation

Considering the requirements mentioned above, it is established that the EMS device will consist of a processing unit with an integrated operating system that allows executing scripts in a high-level language in order to implement the coordination strategy state machine in an agile way and perform the necessary calculations. As a processing unit, an Orange Pi Zero single board computer (SBC) is used, which has an Allwinner H2 + ARM® Cortex®A7 QuadCore processor with 512Mb of RAM memory running the Armbian

operating system. This SBC was selected taking into account that it is an open source development board with a low cost ($12 dollars per unit), with a high processing capacity due to its technical characteristics, and with high availability in the market. Although the processing capacity of the SBC is high, it does not have analog I/O pins. Therefore, it is necessary to integrate an additional component with this kind of pins. As a coupling interface is used, an STM32L476RG microcontroller that has an Arm® Cortex®M4 processor with a maximum working frequency of 80Mhz, 1Mb of flash memory and 128Kb of RAM memory, which is mounted on an STM32L476 NUCLEO development board from STMicroelectronics®. This microcontroller has 3 units, 12 bits ADCs with a working frequency of up to 5Msps and up to 24 input channels, a 12 bits DAC with 2 output channels, as well as multiple communication protocols and GPIO pins. Because the voltage window for both the ADC and the DAC in the microcontroller is 0 to 3,3 VDC, the analog inputs and outputs values of the OPAL® OP4510 simulation platform have been scaled to this range to avoid damaging the EMS. The SPI protocol is selected for communication between the SBC and the microcontroller with a frequency of 1Mhz. The SBC performs the communication as master. A complete representation of the device integrated with the simulation platform is shown in Figure 3.
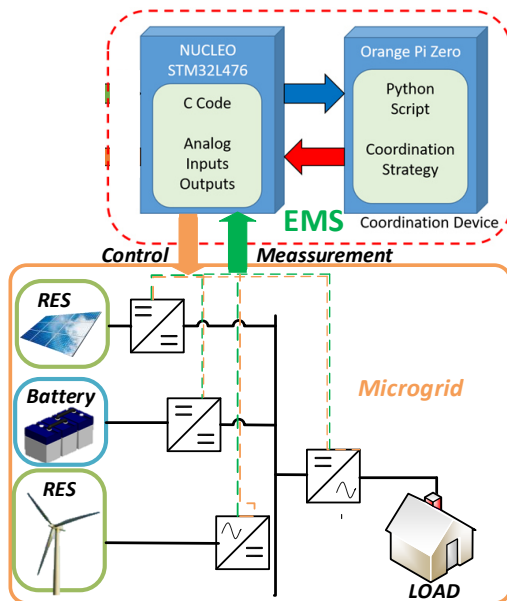
Figure 3. Structure of the EMS electronic device integrate to the microgrid.
Source: Authors

The state machine that executes the rule-based management strategy is implemented on the SBC with a Python3 script. The Numpy library is added to the script, which allows to operate vectors and matrices, and is suitable for solving the equation systems to obtain the curtailment indices of the generators. Within the state machine script, the communication functions with the microcontroller are added to get the analog values and send the curtailment indexes.

A pseudo-code of the Python3 script is shown in Pseudo-code 1. In the microcontroller, a firmware is implemented with the C language using the HAL libraries provided by STMicroelectronics®, which allows to perform the SPI communication with the SBC, read the pins of the ADC channels, and set the analog curtailment indexes using the two channels of the DAC. A pseudo-code of the microcontroller firmware is shown in Pseudo-code 2.

Pseudo-code 1 Python Pseudo-code management Strategy

```
 1:  # Load Machine
 2:  if load state is active then
 3:      if V_bat is lower than threshold then
 4:          load state is inactive;
 5:      else if load state is inactive then
 6:          if SoC is higher than threshold then
 7:              load state is active;
 8:          end if
 9:      end if
10:  end if
11:
12:  # Power Curtailment Machine
13:  if Power Curtailment is disable then
14:      if V_bat is higher than threshold then
15:          Power curtailment is enable;
16:          Solve System();
17:      else
18:          no power curtailment;
19:      end if
20:  else if Power Curtailment is enable then
21:      if Power generation is lower than Load Power then
22:          Power Curtailment is disabled;
23:      else
24:          Solve System();
25:      end if
26:  end if
```

Pseudo-code 2 Microcontroller Interface

```
 1:  if pulse input then
 2:      Convert data from analog inputs;
 3:      Forming SPI Frame;
 4:      Send pulses to GPIO;
 5:      wait until SPI start frame is received();
 6:      if start frame has been received then
 7:          send data;
 8:          wait until SPI answer frame is received();
 9:          if answer frame has beed received then
10:              set analog values;
11:              set GPIO values;
12:          end if
13:      end if
14:  end if
```

The operation of the EMS integrated with the simulation platform can be described as follows: with one of the digital pins of the microcontroller, the synchronization pulse of the simulation is received. This indicates that it has to read the analog variables through the 5 channels of the ADC, which takes approximately 50 us. At the end of the reading, the microcontroller activates a pin connected to the SBC that

indicates that there is data ready to be processed. The SBC, acting as an SPI master, receives this data in a fixed size frame. The received data is converted to the real values (because they are scaled to values between 0 and 3,3 V) and the current mode of the state machine is verified. If it is in MODE I, the curtailment indexes ((α_{PV}) and (α_{WT})) are 1 and the load is on; if it is in MODE II, the new vales of the curtailment indexes are calculated; and if it is in MODE III, the state of the load is changed to off. This procedure is performed in period of less than 100 ms, the curtailment indexes and the state of the load are sent to the microcontroller in another fixed size frame where they are processed. The curtailment indexes are setting in the outputs of the 2 channels of the DAC and the state of the load in a digital pin, where a value 1 corresponds to load on and 0 to load off. These steps are executed in less than 20 us. Including the sending and receiving times of SPI frames that take approximately 300 us, the complete processing time of each sample is less than 150 ms, with which the samples that have to be taken every 0,5 seconds can be processed correctly.

Experimental Validation

A hardware-in-the-loop (HiL) test platform has been used for validating the operation of the EMS electronic device. The test platform is composed of the EMS electronic device, a real-time simulation OPAL® OP4510, and a console for data acquisition and visualization as shown in Figure 4.

(a)

(b)
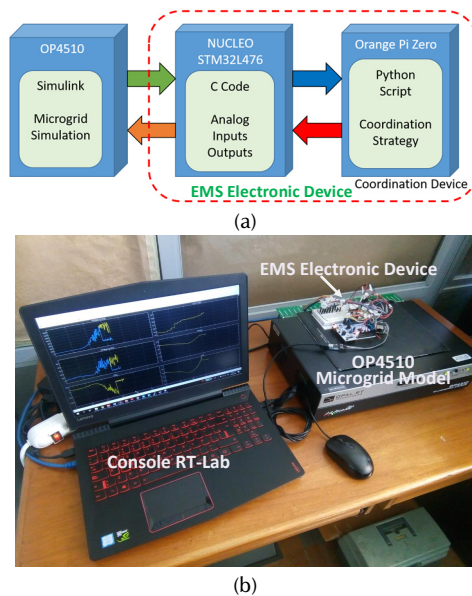
Figure 4. Experimental test platform. (a) Scheme, (b) image.
Source: Authors

The microgrid model has been built in Simulink and embeds into a real-time simulation platform. Table 2 presents the main parameters of the islanded microgrid.

The operation of the system has been tested by using different generation a load profiles. In the case of the generation, the profiles change every 5 minutes, and, in the case of the load, the profile changes every hour.

Table 2. Parameters of the Islanded Microgrid

| Parameter	Symbol	Value
Power Stage		
Nominal Load	$P_{LOAD_{max}}$	2 kW
Maximum Power from RES	$P_{RES_{max}}$	2 kW
ESSs Parameters		
Nominal Voltage	$VBat$	48 V
Maximum battery voltage	$Vmax$	50 V
Minimum Battery Voltage	$Vmin$	45 V
Maximum SoC	SoC_{max}	90%
Minimum SoC	$SoCmin$	20%
Battery Capacity	C_{batt}	10 Ah
charging/discharging efficiency	η_{batt}	0,9

Source: Authors

Figures 5 and 6 show the results obtained from the experimental platform with two different generation and load profiles. In Figures 5 and 6, it is possible to see that, when the battery reaches its maximum voltage value ($V_{batt} = V_{max}$), the operation of the microgrid changes to MODE II. As a consequence, the power generation from RESs (P_{PV}) and (P_{WT}) is curtailed below their maximum available power ($P_{PV_{MP}}$) and ($P_{WT_{MP}}$) to keep the power balance in the system, and preventing the battery from overcharging. It can be seen that even in the accelerated simulation of the microgrid, explained in a previous section, the EMS devices manage to deal with all the required processes in the ruled-based management system.
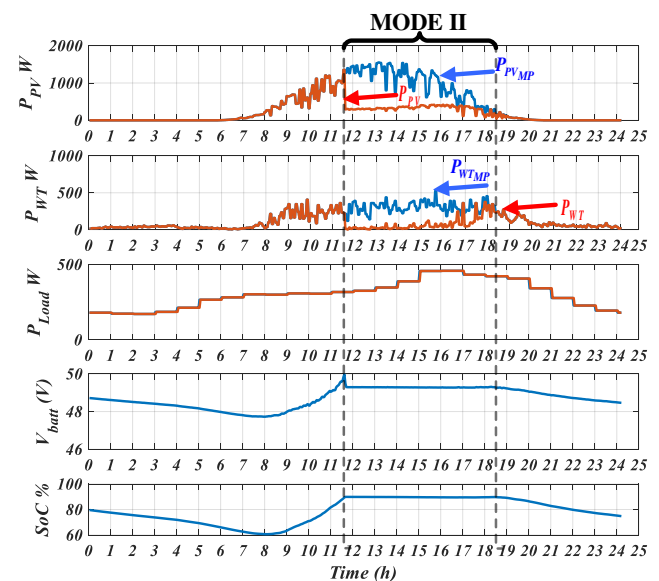
Figure 5. Operation of the microgrid for time period of 24h.
Source: Authors
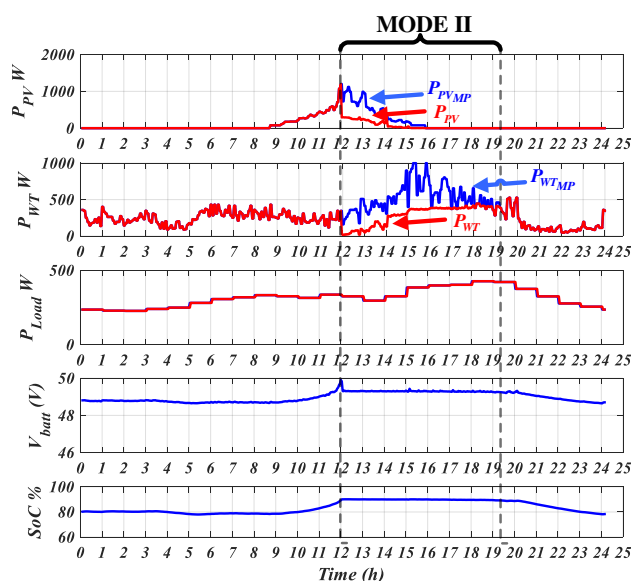
Figure 6. Operation of the microgrid for time period of 24h.
Source: Authors

Conclusions

The capability of the HIL method to represent real variables of a Simulink simulation as electrical outputs allows the execution of tests to hardware control devices in real-time. This fact minimizes the initial need to have a real system plant, which comprises a system of medium complexity devices in the case of a microgrid.

It is possible to implement a rule-based management strategy based on state machines focused on improving the lifespan of the energy storage resource, which is one of the most critical components in the microgrid. This, by taking advantage of the processing capacity of a single board computer working in conjunction with a microcontroller. On top of that, it is important to consider the possible limitations in the selection of the electronic device, such as the ability of the device to generate responses in real-time. In particular, it is important to consider the processing times, data representation, and resolution of ADC and DAC converters for more accurate answers.

Acknowledgment

References

Al sumaiti, A. S., Ahmed, M. H., and Salama, M. M. A. (2014). Smart home activities: A literature review. *Electric Power Components and Systems, 42*(3-4), 294-305. 10.1080/15325008.2013.832439

Battery University (n.d.). *Secondary (Rechargeable) Batteries - Battery University.* https://batteryuniversity.com/index.php/

Beaudin, M., Zareipour, H., Schellenberg, A., and Rosehart, W. (2015). Chapter 1 - energy storage for mitigating the variability of renewable electricity sources. In P. D. Lu (ed.). *Energy Storage for Smart Grids* (pp. 1-33). Boston, MA: Academic Press. 10.1016/B978-0-12-410491-4.00001-4

Buchmann, I. (2016). *Batteries in a Portable World: A Handbook on Rechargeable Batteries for Non-engineers*. Richmond, Canada: Cadex Electronics.

Díaz, N. L., Luna, A. C., Vasquez, J. C., and Guerrero, J. M. (2017). Centralized control architecture for coordination of distributed renewable generation and energy storage in islanded AC microgrids. *IEEE Transactions on Power Electronics 32*(7), 5202-5213. 10.1109/TPEL.2016.2606653

Casolino, G., Russo, M., Varilone, P., and Pescosolido, D. (2018). Hardware-in-the-loop validation of energy management systems for microgrids: A short overview and a case study. *Energies 11*(11): 2978. 10.3390/en11112978

de Matos, J., e Silva, F., and Ribeiro, L. (2015). Power control in AC isolated microgrids with renewable energy sources and energy storage systems. *IEEE Transactions on Industrial Electronics, 62*(6), 3490-3498. 10.1109/TIE.2014.2367463

Estrada, L., Vázquez, N., Vaquero, J., de Castro, and Arau, J. (2020). Real-time hardware in the loop simulation methodology for power converters using labview fpga. *Energies 13*(2), 373. 10.3390/en13020373

Hofman, T., Steinbuch, M., van Druten, R., and Serrarens, A. (2006). Rule-based energy management strategies for hybrid vehicle drivetrains: A fundamental approach in reducing computation time. *IFAC Proceedings Volumes 39*(16), 740-745. 10.3182/20060912-3-DE-2911.00128

IEEE (2017). *IEEE standard for the specification of microgrid controllers, IEEE Std 2030.7- 2017* (pp. 1-42). New York, NY: IEEE.

IEEE (2018). *IEEE standard for the testing of microgrid controllers, IEEE Std 2030.8-2018* (pp. 1-42). New York, NY: IEEE.

Jurasz, J., Mikulik, J., and Krzywda, M. (2017). Concept of large scale pv-wt-psh energy sources coupled with the national power system. *E3S Web Conference, 17*, 00035. 10.1051/e3sconf/20171700035

Keyhani, A. (2016). *Design of Smart Power Grid Renewable Energy Systems*. IEEE Press Series on Power Engineering, Hoboken, NJ: Wiley.

Kim, J. Y., Jeon, J. H., Kim, S. K., Cho, C., Park, J. H., Kim, H. M., and Nam, K. Y. (2010). Cooperative control strategy of energy storage system and microsources for stabilizing the microgrid during islanded operation. *IEEE Transactions on Power Electronics 25*(12), 3037-3048. 10.1109/TPEL.2010.2073488

Kim, T., and Qiao, W. (2011). A hybrid battery model capable of capturing dynamic circuit characteristics and nonlinear capacity effects. *IEEE Transactions on Energy Conversion 26*(4), 1172-1180. 10.1109/TEC.2011.2167014

Liu, Y., Qiu, B., Fan, X., Zhu, H., and Han, B. (2016). Review of smart home energy management systems. *Energy Procedia, 104*, 504-508. 10.1016/j.egypro.2016.12.085

Luna, A. (2017). *Energy Management Systems for Microgrids Equipped with Renewable Energy Sources and Battery Units* (Doctoral dissertation, Universitat Politècnica de Catalunya, Barcelona, Spain). https://www.semanticscholar.org/paper/Energy-Management-Systems-for-Microgrids-Equipped-Hernandez/c7ca89f73ec8ffea7c4ea97a7c8016684ec16d1b

Mahmood, H., Michaelson, D., and Jiang, J. (2015). Strategies for independent deployment and autonomous control of pv and battery units in islanded microgrids. *IEEE Journal of Emerging and Selected Topics in Power Electronics, 3*(3), 742-755. 10.1109/JESTPE.2015.2413756

Mao, M., Huang, H., and Chang, L. (2013). Real-time energy coordinated and balance control strategies for microgrid with photovoltaic generators. In IEEE (Eds) *2013 4th IEEE International Symposium on Power Electronics for Distributed Generation Systems* (*PEDG*) (pp. 1-7). New York, NY: IEEE. 10.1109/PEDG.2013.6785609

Marra, F., and Yang, G. (2015). Chapter 10 - decentralized energy storage in residential feeders with photovoltaics. In P. D. Lu (ed.), *Energy Storage for Smart Grids* (pp. 277-294). Boston, MA: Academic Press. 10.1016/B978-0-12-410491-4.00010-5

Montoya, J., Brandl, R., Vishwanath, K., Johnson, J., Darbali-Zamora, R., Summers, A., Hashimoto, J., Kikusato, H., Ustun, T. S., Ninad, N., Apablaza-Aranciba, E., Bérard, J.-P., Rivard, M., Ali, S. Q., Obushevs, A., Heussen, K., Stanev, R., Guillo-Sansano, E., Syed, M. H., Burt, G., Cho, C., Hyeong-Jun, Y., Awasthi, C. P., Wadhwa, K., and Brüdlinger, R. (2020). Advanced laboratory testing methods using real-time simulation and hardware-in-the-loop techniques: A survey of smart grid international research facility network activities. *Energies 13*(12), 3267. 10.3390/en13123267

Patsios, C., Chaniotis, A., Rotas, M., and Kladas, A. (2009). A comparison of maximum-power-point tracking control techniques for low-power variable-speed wind generators, *8th International Symposium on Advanced Electromechanical Motion Systems Electric Drives Joint Symposium*. Lillie, France, 2009, pp. 1-6. 10.1109/ELECTROMOTION.2009.5259095

Pecas Lopes, J., Moreira, C., and Madureira, A. (2006). Defining control strategies for microgrids islanded operation. *IEEE Transactions on Power Systems 21*(2), 916-924. 10.1109/TPWRS.2006.873018

Rafique, S. F. and Jianhua, Z. (2018). Energy management system, generation and demand predictors: a review. *IET Generation, Transmission Distribution 12*(3), 519-530. 10.1049/iet-gtd.2017.0354

Sun, C., Joos, G., Ali, S. Q., Paquin, J. N., Rangel, C. M., Jajeh, F. A., Novickij, I., and Bouffard, F. (2020). Design and real-time implementation of a centralized microgrid control system with rule-based dispatch and seamless transition function. *IEEE Transactions on Industry Applications, 56*(3), 3168-3177. 10.1109/TIA.2020.2979790

Teodorescu, R., Liserre, M., and Rodriguez, P. (2010). *Grid Converters for Photovoltaic and Wind Power Systems.* New York, NY: IEEE, Wiley.

Trujillo Rodriguez, C. L., Diaz Aldana, N. L., and Hernandez Mora, J. A. (2015). Control of an inverter for photovoltaic arrays, using an estimator of short circuit current for maximum power point tracking, *IEEE Latin America Transactions 13*(10): 3294-3303. 10.1109/TLA.2015.7387234

Wang, Y., Nguyen, T. L., Xu, Y., and Shi, D. (2020). Distributed control of heterogeneous energy storage systems in islanded microgrids: Finite-time approach and cyber-physical implementation. *International Journal of Electrical Power and Energy Systems, 119*, 105898. 10.1016/j.ijepes.2020.105898

Instructions for Authors

Editorial Committee reserves the copyright to printing any material and its total or partial reproduction, as well as the right to accept submitted material or reject it. It also reserves the right to make any editorial modification which it thinks fit. In such event, the author of the submitted material in question will receive the evaluators' recommendations for changes to be made in writing. If an author accepts them, the revised (or rewritten) article must be submitted with the suggested changes having been made by the date fixed by the journal to guarantee its publication in the programmed issue.

The process to be followed for publishing an article in the journal

The article must be uploaded into the journal's OJS website, see the guidelines for article submission in the Authors guide section in our website http://www.revistas.unal.edu.co/index.php/ingeinv/article/view/59291/56815. Any manuscript must be sent using journal's template (6 pages length max.) and must be accompanied by the license agreement, addressed to the journal's editor, Prof. Andrés Pavas, stating that all authors involved in the work in question agree to it being submitted for consideration in the *Ingeniería e Investigación journal*.

Article and License templates are available on: http://www.revistas.unal.edu.co/index.php/ingeinv/index

Once an article has been received by the journal, the corresponding author will be notified by e-mail and the peer-review process will be begun. Following this evaluation, authors will then be informed whether their article has been accepted or not. If accepted, authors must deal with the respective corrections recommended by the evaluators and the Editorial Committee's final decision. If it is to be published.

Content

All articles being considered by the committee for possible publication in the *Ingeniería e Investigación journal* must consist of the following parts:

- Title, abstract and keywords must be written in Spanish and English. The title must clearly explain the contents of the article in question, written in normal title form and be preferably brief. The abstract should contain around 200 words in Spanish and English, as well as including the methods and materials used, results obtained and conclusions drawn.

- An Introduction must be given. It must describe article's general purpuose, including its main objective, referring to any previous work and the scope of the current article.

- Conclusions must be drawn. This section must provide the implication of the results found and their relationship to the proposed objective.

- Bibliographical references must be given (an explanation and example of how to set them out is given later on).

- Acknowledgements (Optional). These should be brief and mention any essential support received for carrying out the work being reported.

- Appendix (Optional).

Scientific and technological research articles must also include:

- Experimental development. This must be written giving sufficient details for the subject to be fully understood by readers, including descriptions of any procedures involved.

- Results. These must give a clear explanation and interpretation of the findings. If it is necessary, a brief, focused discussion about how given results can be interpreted.

It is required that the bibliographical references for all articles are included at the end of the article, given in alphabetical order of first authors' surnames and mentioned in the text and, since May 2014, it is asked that the authors use the American Psychological Association (APA) style for citation and references:

- Articles published in journals:

Author, A. A., Author, B. B., & Author, C. C. (year). Article title. Journal Title, volume number(issue number), page numbers.

Del Sasso, L. A., Bey, L. G. & Renzel, D. (1958). Low-scale flight ballistic measurements for guided missiles. *Journal of the Aeronautical Sciences, 15*(10), 605-608

Author, A. A., & Author, B. B. (year). Article title. Journal Title, volume number(issue number), page numbers. Retrieved from http://www.xxxxxxxxxxxxxxxx

Gaona, P. A. (2014). Information visualization: a proposal to improve search and access digital resources in repositories. Ingeniería e Investigación, 34(1), 83-89. Retrieved from http://www.revistas.unal.edu.co/index.php/ingeinv/article/ view/39449

- Books:

Author, A. A. & Author, B. B. (year). Title of work. Location: Publisher.

Turner, M. J., Martin, H. C. & Leible, R. C. (1964). Further development and applications of the stiffness method, Matrix Methods of Structural Analysis. New York: the Macmillan Co.

- Conference papers and symposium contributions:

Uribe, J. (1973, September). The effects of fire on the structure of Avianca building, Paper presented at National Seminar concerning Tall Buildings, Bogotá, Colombian School of Engineering.

- Theses or undergraduate projects:

Patton, F. D. (1906). Multiple modes of shear failure in rock-related materials (Ph.D. thesis, University of Illinois).

Further information can be obtained by:

Contacting the Editorial Team (Email: revii_bog@unal.edu.co) or Prof. Andrés Pavas (Editor-in-Chief. Email: fapavasm@unal.edu.co)

The *Ingeniería e Investigación* journal's office is located at: Ciudad Universitaria, Facultad de Ingeniería, Edificio CADE. Telefax: (57-1) 3165000 Ext. 13674. Bogotá - Colombia.